Ethane Dehydrogenation Using a Catalytic Membrane Reactor

by

Zhengnan Yu

A thesis submitted in partial fulfillment of the requirements for the degree of

Master of Science

in
Chemical Engineering

Department of Chemical and Materials Engineering
University of Alberta

Abstract

The steam cracking of hydrocarbons is the dominant technology for ethylene production and is a highly energy intensive process. The increasing demand for ethylene has stimulated substantial research into the development of new process routes to reduce energy consumption and other costs. Catalytic dehydrogenation of ethane using a membrane reactor is an attractive solution because the cracking equilibrium can be shifted in favor of ethylene by selectively removing hydrogen. Lower temperatures can thus be used to generate comparable ethylene yields. Using natural mordenite as membrane and Pt/Al_2O_3 as catalyst, a reactor with membrane area to reactor volume ratio of 0.16 m^{-1} improved ethylene yield by 15.6% comparing to the conventional packed-bed reactor at 500°C. A novel Pt-Zn/ETS-2 catalyst for ethane dehydrogenation was also developed. With this catalyst, unlike the Pt/Al_2O_3, side reactions could be completely suppressed and the ethylene selectivity could reach 100% while conversion was at equilibrium.

Acknowledgements

I would like to thank my supervisor Professor Steven M. Kuznicki for his directions, guidance, and support. Without his help and supports, this thesis would not have been possible.

I appreciate all of the help I have received from Dr. Kuznicki's group. Specifically, I wish to thank Dr. James Sawada for his guidance and support of my research as well as his help in the revision of my thesis. I also wish to thank Dr. Adolfo Avila for valuable discussions, assistance with data analysis, and help in conducting the membrane reactor testing. I want to extend my thanks Weizhu An for her insights, suggestions, and varieties of help in the lab. I also wish to thank Lan Wu and Tong Qiu for their support of my research efforts in the lab. I would like to extend my appreciation to Albana Zeko and Dr. Tetyana Kuznicki for their efforts to improve my technical writing skills.

Jing Shen, PhD candidate in Dr. Natalia Semagina's group, conducted the TPR tests for me and helped guide the XPS data analysis. Dr. Lianhui Ding graciously offered to help revise my thesis and provide valuable suggestions about both catalyst characterization and technical writing. I appreciate their valuable assistance.

I also thank Lily Laser, Graduate Administrative Assistant, for her kind assistance through the final stages of my thesis.

Table of Contents

List of Tables

List of Figures

Abbreviations

Symbol	Description
AGO	Atmospheric gas oil
BET	Brunauer-Emmett-Teller
BJH	Barret-Joyner-Halenda
EB	Ethylbenzene
EDC	Ethylene dichloride
EDX	Energy dispersive x-ray
EO	Ethylene oxide
ETS-2	Engelhard titanosilicate-2
GC	Gas chromatography
HDPE	High density polyethylene
HK	Horvath-Kawazoe
ID	Inner diameter, mm
LDPE	Low density polyethylene
LLDPE	Linear low density polyethylene
LPG	Liquefied petroleum gas
OD	Outer diameter, mm
PBMR	Packed-bed membrane reactor
PE	Polyethylene
PVC	Polyvinyl chloride
SEM	Scanning electron microscopy

TCD	Thermal conductivity detector
TEM	Transmission electron microscopy
TGA	Thermogravimetric analysis
TG-MS	Thermogravimetric analysis-mass spectrometry
TPR	Temperature-programmed reduction
WHSV	Weight hourly space velocity, h^{-1}
XPS	X-ray photoelectron spectroscopy
XRD	X-ray diffraction

Symbols

Symbol	Description	Unit
c	Speed of light	m/s
C	BET constant	
d	Pore diameter	m
d_A	Diameter of adsorbate molecule	m
d_p	Particle diameter	m
d_s	Diameter of adsorbent molecule	m
E_1	Heat of adsorption for the 1st layer	J
E_L	Heat of adsorption for the 2nd and higher layers, heat of liquefaction	J
F_A	Permeation flux of gas species A	$mol/(m^2 \cdot s)$
F_K	Permeance of membrane	$mol/(m^2 \cdot s \cdot Pa)$
k	Boltzmann constant, 1.38×10^{-23}	J/K

K	Avogadro's number, 6.02×10^{23}	mol^{-1}
l	Distance between two layers of adsorbent	m
L	Thickness of porous medium	m
m	Mass of an electron	kg
M_A	Molecular weight of gas species A	g/mol
N_A	Number of molecules per unit area of adsorbate	
N_s	Number of atoms per unit area of adsorbent	
P	Pressure, or equilibrium pressure	Pa
P_0	Saturation pressure of adsorbates at the temperature of adsorption	Pa
r	Radius of pore	m
R	Gas law constant	$J/(mol \cdot K)$
T	Absolute temperature	K
W	Weight of gas adsorbed at a relative pressure	g
W_m	Weight of adsorbate constituting a monolayer of surface coverage	g
α_A	Polarizability of adsorbate	
α_s	Polarizability of adsorbent	
ε	Porosity	
λ	Mean free path	m
τ	Tortuosity	
χ_A	Magnetic susceptibility of adsorbate	
χ_s	Magnetic susceptibility of adsorbent	

Chapter 1. Introduction

1.1 Overview of Global Ethylene Production

Ethylene is a versatile petrochemical intermediate, and it plays a vital role to modern society. As Figure 1-1 shows, a wide series of daily items such as plastic bags, milk and food cartons, washing-up liquids, paints, antifreeze, toys, pipes, window frames, car components, and many other industrial materials are produced from ethylene. Based on Chemical Market Associates Inc. (CMAI) data (Figure 1-2), the majority of global ethylene is for the production of polyethylene (PE), which is primarily used in a wide variety of non-durable goods applications, such as packaging materials. Ethylene oxide (EO), ethylene dichloride (EDC), and ethylbenzene (EB)/styrene are also important ethylene derivatives. The figure also shows a continuous increase of ethylene demand in the near future as PE feedstock.

According to Oil & Gas Journal's survey, global ethylene capacity has been increasing since 1995 or earlier [1], as shown in Figure 1-3. Asia-Pacific and Middle East were the two fastest increasing regions. The ethylene capacity in North America and West Europe has been almost unchanged in recent years. Survey data [2] revealed that as of January 1, 2013 the global ethylene production was more than 143 million tons versus 141 million tons in 2012. Formosa Petrochemical Corp. had the largest ethylene complex in Mailiao, Taiwan with the capacity of 2.94 million tons. Nova Chemicals Corp. had the second largest complex in Joffre, Alberta with

the capacity of 2.81 million tons. Complex capacity varied yearly, but the rank did not change since 2010 [1-3].

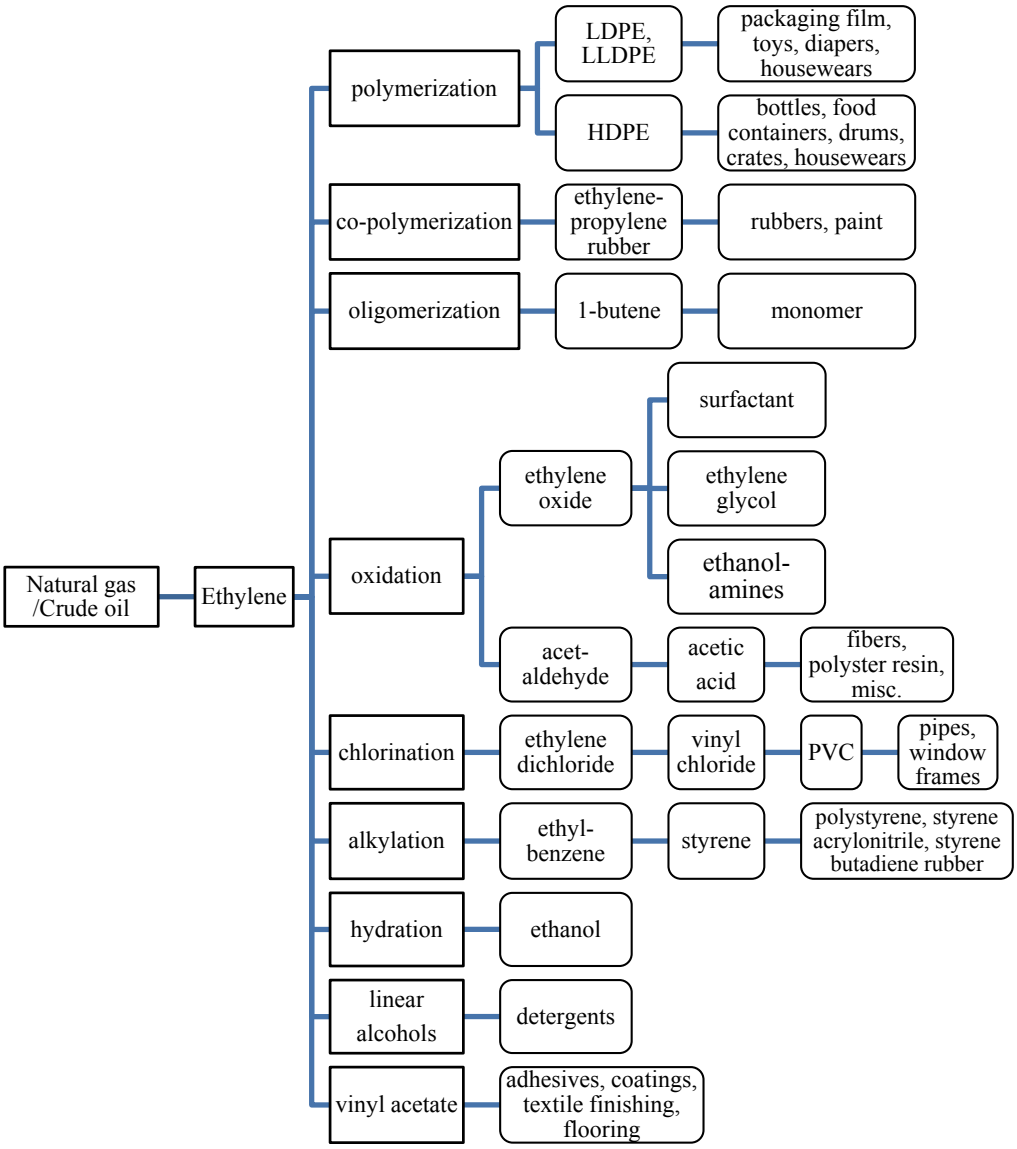

Figure 1-1 The Main Applications of Ethylene

Saudi Basic Industries Corp. (SABIC) replaced Dow Chemical Co. in 2010 to become the largest ethylene producer with the total capacity of 23.67 million tons

per year. Dow Chemical Co. became the second largest one worldwide with the total capacity of 23.57 million tons per year. The capacity rank of the two companies did not change since 2010. As of January 2013, the United States was the largest producer, with the capacity of 28.12 million tons. China and Saudi Arabia were the second and third ones, with the capacity of 13.78 and 13.16 million tons respectively. Canada was the seventh with the capacity of 5.53 million tons.

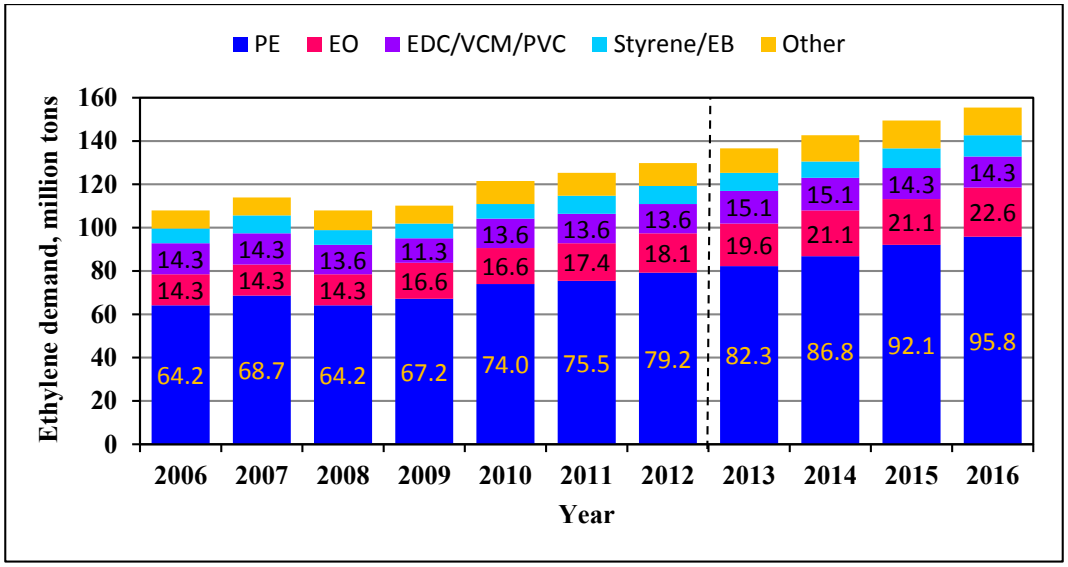

Source: *CMAI, 2012 World Light Olefins Analysis*

Figure 1-2 Global Ethylene Demand by End Use

As shown in Figure 1-3, global ethylene capacity reached 147.7 million tons in 2011, and was predicted at over 170 million tons in 2016 at 3.4% annual growth [4]. Relying on its huge market advantage and rapid growth of demand, Asia-Pacific becomes a region attractive to investors for ethylene production. Even though the newly added production capacity was small, the advantage of low production costs

could make, Middle East the world's most investment-intensive region in the ethylene industry, and the main ethylene exporting area [5].

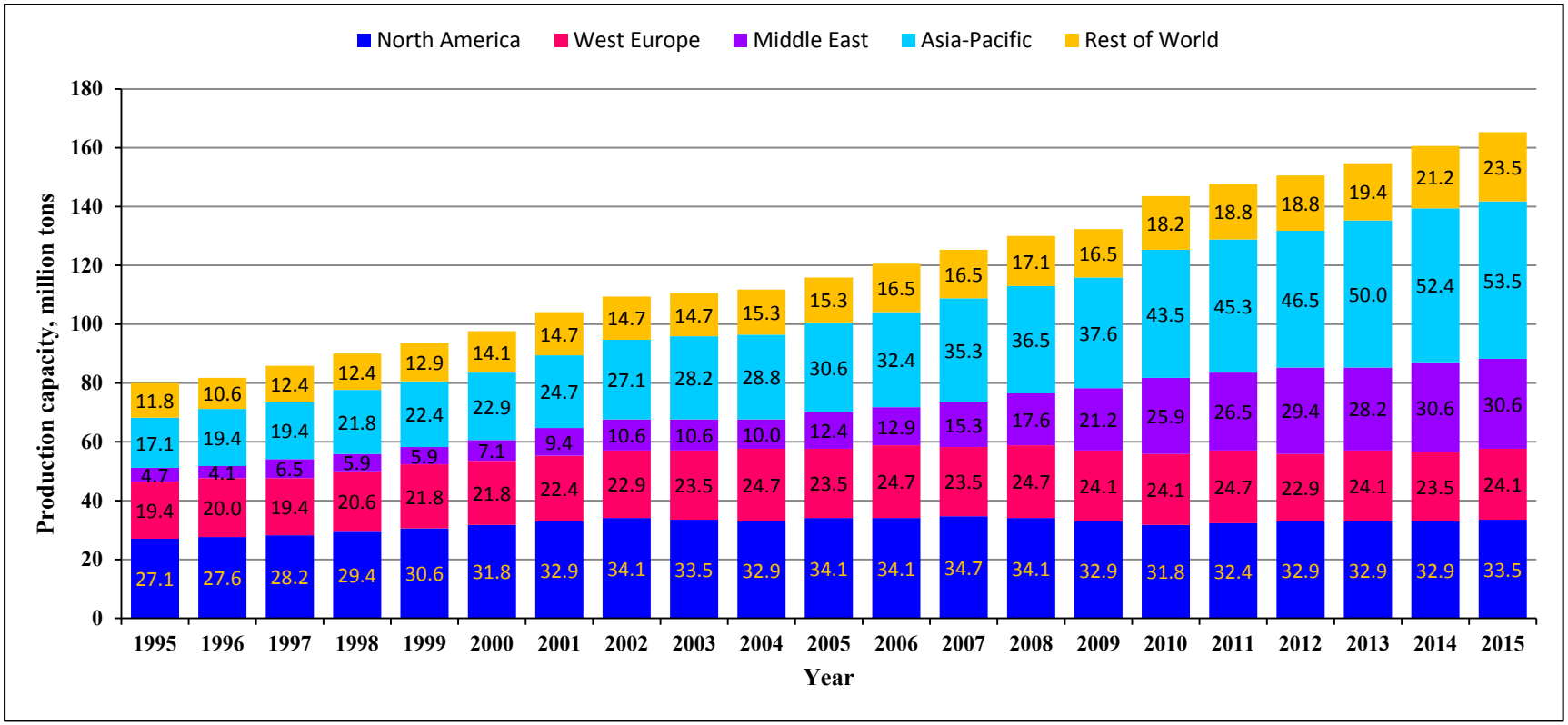

Figure 1-3 Regional Ethylene Capacity Growth

1.2 Feedstock of Ethylene Production

Natural gas (ethane) and petroleum distillates (naphtha) are the main feedstocks for ethylene production. The trend of their ratios over the years are illustrated in Figure 1-4. The figure indicates naphtha is the major feedstock for ethylene production globally. However, ethane's use as feedstock has gradually increased. The cost of feedstock accounts for 60% - 80% of ethylene production costs. The main factors driving feedstock changes for petrochemical plants are the supply and the price of oil and natural gas.

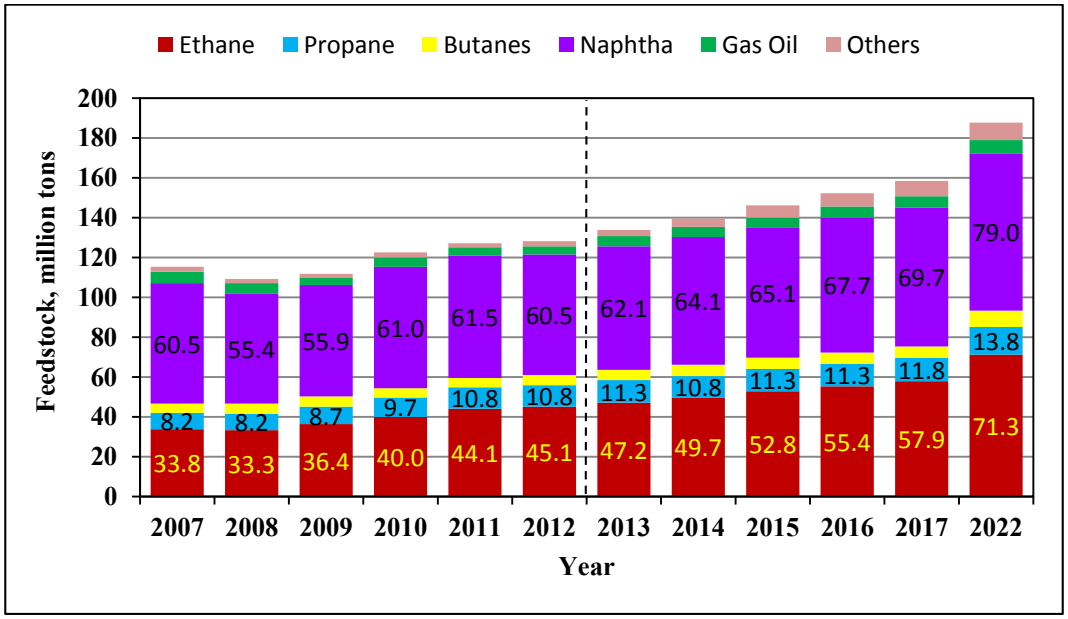

Figure 1-4 Global Ethylene Production by Feedstock [6]

In natural gas-rich regions, like North America, ethane was the main feedstock for ethylene production in recent years [4, 7, 8]. As showed in Figure 1-5, ethane was the main feedstock for ethylene production in the United States from 2005 to 2011.

Regional cash cost and global cash cost of ethylene production are illustrated in Figure 1-6 and Figure 1-7 respectively. As revealed from the two figures, ethane as ethylene feedstock was more profitable than LPG and naphtha. The higher margins of ethane-to-ethylene have resulted in significant feedstock shifts in the U.S. over the past few years. Numerous chemical producers [9, 10] are expanding ethylene capacity to take advantage of the low-cost and increased availability of ethane from natural gas. A vast number of chemicals and products are made from ethylene. It is the most produced organic chemical worldwide. In 2012, global ethylene sales reached about 150 billion US dollars [7].

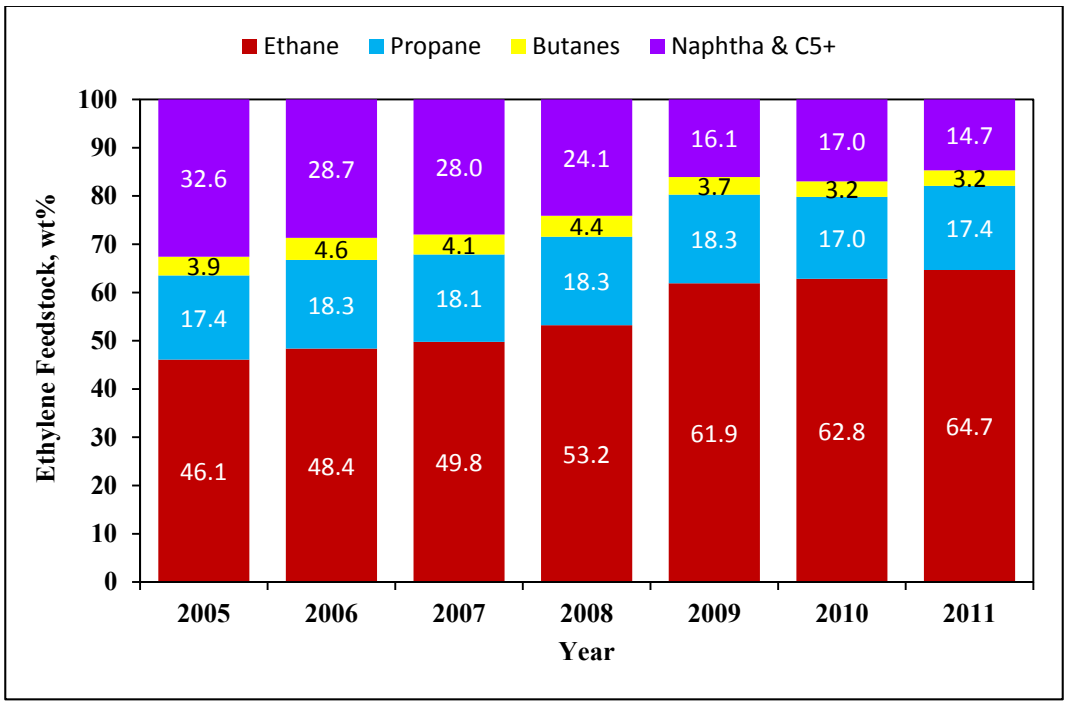

Figure 1-5 U.S. Ethylene Feedstock Sources (Percent of Ethylene Production) [11]

Ethane is the most competitive feedstock for ethylene production due to its cost and the highest ethylene yield among all other feedstocks. Generally, ethylene yields decrease with the increase in the density of feedstocks. Heavier feedstocks produce more low-value by-products. To produce the same amount of ethylene, the use of AGO feed was about three times that of ethane. Furthermore, the utilities consumption is higher for heavy feeds.

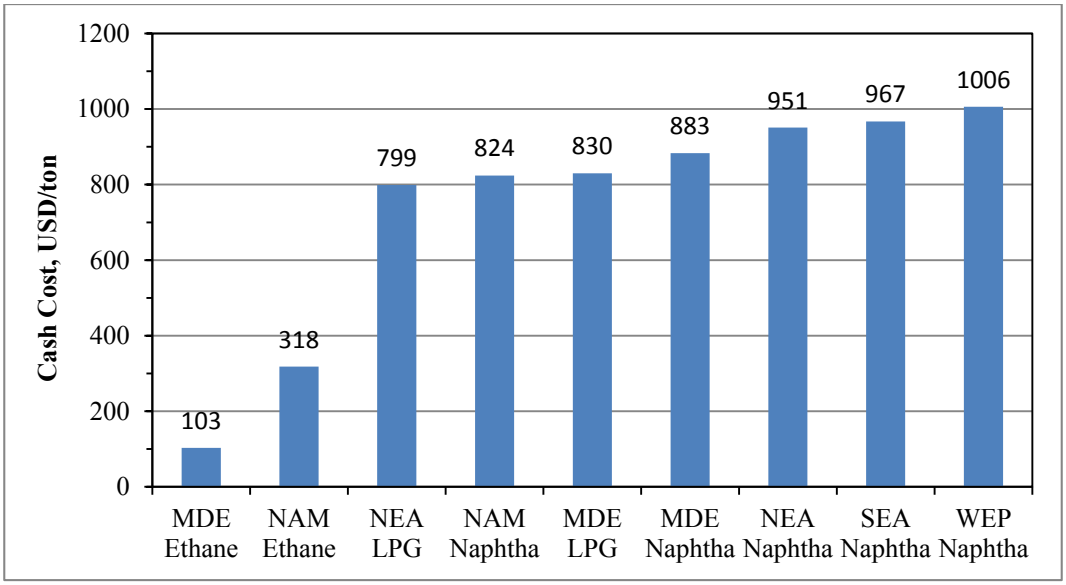

Source: IHS as of July 2012.

MDE: Middle East, NAM: North America, NEA: Northeast Asia, SEA: Southeast Asia, WEP: Western Europe.

Figure 1-6 Global Ethylene Cash Cost by Region

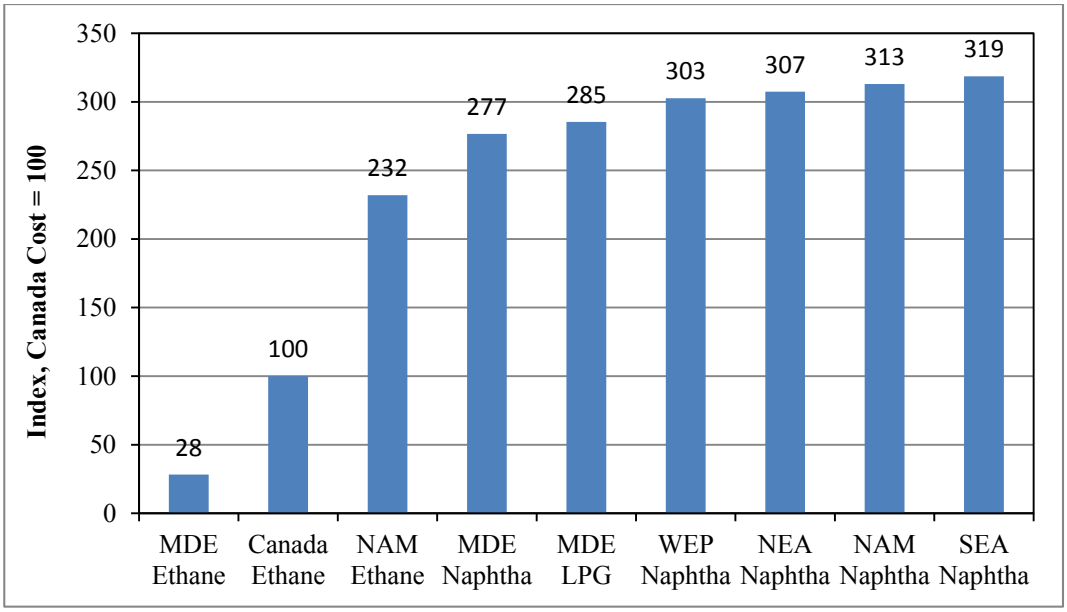

MDE: Middle East, NAM: North America, NEA: Northeast Asia, SEA: Southeast Asia, WEP: Western Europe.

Figure 1-7 Global Ethylene Cash Cost Index: 2010 [12]

1.3 Technologies for Ethylene Production

Driven by the pursuit of lower investment cost the tube furnace pyrolysis technology has continually improved over the course of several decades. Currently, tube furnace steam cracking is the dominant technology in ethylene production. About 99% of global ethylene production uses tube furnace pyrolysis method. A simplified process flow diagram is shown in Figure 1-8.

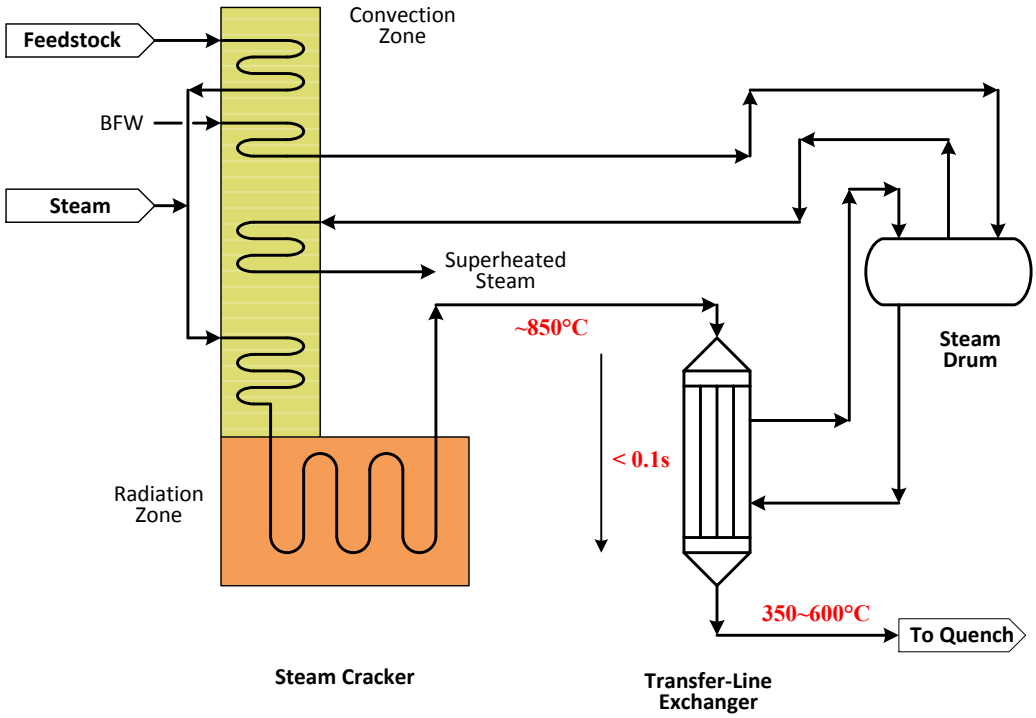

Figure 1-8 Steam Cracking Process

First, preheated hydrocarbon feedstock (500 to 680 °C) is mixed up with dilution steam in the convection zone and then quickly discharged to the radiation zone (750 to 875 °C) where the feed is cracked to produce ethylene, other small olefins, di-olefins, and by-products. The method is also known as steam cracking process. The residence time is 0.1 – 0.5 seconds. Due to the high reactivity of the products, the high temperature effluent has to be quenched within 0.02 – 0.1 seconds in the transfer-line exchanger to avoid further unwanted side reactions. The cooled products are separated by distillation towers.

Using ethane as feedstock, typical hydrocarbon conversion levels reach 70% with olefin yields of around 50% [13]. Single-pass conversion and yields are lower in naphtha crackers.

Industrial ethylene production requires dehydrogenation and/or cracking reactions of hydrocarbon molecules at elevated temperatures because the cracking reactions are highly endothermic, and also equilibrium limited. Unfortunately, ethylene and feed hydrocarbons are very reactive at high temperature, which means they can easily convert to undesirable by-products. Both dehydrogenation and cracking are expansion reactions, which according to the Le Chatelier's principle means that lower product partial pressure is favored for the higher conversion. In the steam cracking process, steam is used as a diluent to lower reaction partial pressure. Lower hydrogen partial pressure also reduces unwanted hydrogenation reactions, which increases yields of desired products—olefins. Steam can also suppress coking in radiant coils. The design constraints for increasing ethylene yields are shown in Figure 1-9.

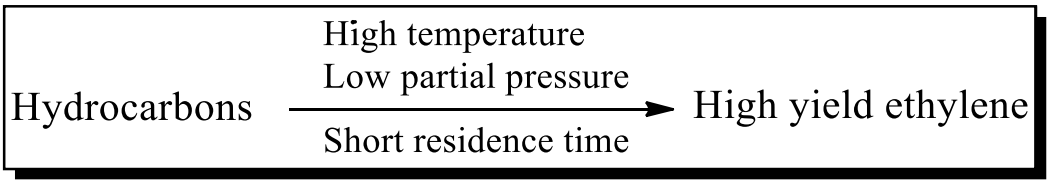

Figure 1-9 Optimal conditions of ethylene production

As shown in Figure 1-9, parameters that influence the performance and product distribution are residence time, the partial pressures of the feedstock and steam, and the process temperature (profile) in the reactor.

The main six technology licensors for ethylene production and their main technology characteristics are summarized in Table 1-1. All technology providers

have their own proprietary equipment, which is designed to maximize olefin (ethylene) yields with different feedstock by varying operation conditions.

Table 1-1 Main technology licensors for ethylene production

Companies	ABB Lummus	Stone & Webster	Technip KTI	Kellogg Brown & Root	Mitsubishi Petrochemical Company	Selas-Linde
Pyrolysis furnace	SRT-I, II, III, IV, V, VI, VII	USC-U, W, M	SMK, USC M-coil, GK6, USC U-coil	USRT, SCORE	M-TCF	PyroCrack, LSCC
Quench boiler	Quicker Quencher TLE	USX, M-SLE	U coil/ SLE	Kellogg casing TLX	M-TLX	Linde quench exchanger
Furnace outlet temperature, ℃	830~840	820~860	Diesel: 800 Naphtha: 840	871~927	820~850	
Residence time, s	0.2~0.6	0.2~0.3	0.3	0.03~0.1	0.3~0.6	
Thermal efficiency, %	SRT-II: 87-91 SRT-III: 92-93	86~91	90	93~94	89~91	
Feedstock	Ethane to diesel	Ethane to diesel	Ethane to diesel	Heavy diesel	Ethane to diesel	Ethane to light diesel

1.4 Challenges for Tube Furnace Pyrolysis Process

1.4.1 Coking

Coking is one of the challenges to radiant coils and quench exchangers. There are two types of coking, tube metal catalyzed coking and pyrolysis coking [14]. Carburized metals are problematic as they can boost the catalyzed coking process. Catalytically formed coke is about 80% of the total coke when using gas feedstocks, like ethane, propane, and butane. For liquid feedstock, catalytically formed coke is about 30% to 40% of the total coke. Pyrolysis coking is the lesser coke product and

is caused by dehydrogenation of small unsaturated hydrocarbons like acetylene, and polycyclic aromatics by condensation, polymerization, and dehydrogenation reactions.

The thickness of coke is a function of tube metal temperature and conversion. Coke layer could reach 10 mm or thicker depending on the type of feedstock and operation severity. Coking in furnace tubes can reduce product yields, decrease production capacity, increase energy consumption, shorten tube service life, and increase maintenance and operation costs.

A variety of anti-coking technologies have been developed to reduce coking. The goal is to engineer a metal surface by applying a layer or multiple layers of coating. The coating materials could be silicon-based, like GE Betz's Py-Coat™, Chevron Phillips' CCA 500, or phosphorus-based, like Nalco's COKE-LESS®. These coating agents can be applied on-line to make a stable layer coated on the inner surface of the tubes in the furnace. The coated layer can reduce coking effectively, protect the tube metal base from oxidation, and improve tube life and extend the de-coking cycle. Westaim's CoatAlloy™ and Nova Chemicals /Kubota's ANK 400 coating agents can be applied on the inner surfaces of new furnace tubes and transfer line exchangers. Coking inhibitors can also reduce coking. The agents are the chemicals containing S, P, Sn, Sb, and Cr among others. Typical compounds are DMDS, triphenylphosphine, triphenyl phosphorus oxide, and chromium phosphate. Both coating agents and inhibitors are effective in reducing coking and extending operation cycles. However, these technologies only mitigate coking issues, but cannot eliminate the coking problems.

1.4.2 Energy Consumption of Pyrolysis Furnace

Steam cracking for light olefins such as ethylene and propylene production is the most energy consuming process in the chemical industry. During ethylene production, the cracking furnace is a major energy consumer. Its energy consumption is about 50-60% of the total energy of an ethylene complex. A naphtha steam cracker consumes about 65% of the total process energy and approximately 75% of the total energy loss [15]. It is a challenge to increase ethylene production while saving energy simultaneously. Thermodynamically, higher temperatures enhance endothermic reaction to reach higher equilibrium conversion. Kinetically, higher temperatures also accelerate the relative rate of the primary reaction (producing target product) to secondary reaction (producing by-products). However, higher temperatures also cause deep cracking of hydrocarbons and accelerate coking because these secondary reactions are more thermodynamic favorable. This results in ethylene yield reduction and other problems. A solution is to shorten residence time. In order to maintain conversion in shorter residence time, higher tube and furnace temperatures are required, which increases the energy consumption of the cracking furnace.

In summary, ethane is the most economically competitive feedstock for ethylene production. However, ethane dehydrogenation is an endothermic and equilibrium limited process so that high reaction temperature is required for industrial production operations. Although hydrocarbon steam cracking is the main industrial process for ethylene manufacture, it has its disadvantages. First, steam cracking is a highly energy intensive process. When using ethane as feedstock, the

total energy consumption is 16 GJ/ton versus 23 GJ/ton when using naphtha [13]. Second, fired furnace produces CO_2 and NO_x emissions. approximately 1 – 1.6 tons of CO_2 are produced per ton of ethylene. In addition, coking and high temperature create maintenance challenges for furnace tubes.

High temperature operation also produces low value by-products. According to the mechanism of ethane dehydrogenation, if one of the products hydrogen can be selectively removed from the reaction system, it can break the thermodynamic barrier and will increase the conversion even at lower temperature and achieve more economical production of ethylene. An effective catalyst can also help the dehydrogenation reaction reach equilibrium quickly at low temperature.

1.5 Catalytic Dehydrogenation of Ethane to Ethylene by Membrane Reactor

1.5.1 Gas Separation Mechanisms of Porous Inorganic Membranes

Pore size is fundamental to the separation properties of porous membranes. According to the IUPAC classification of pore diameter [16], there are three general types of porous membranes: macroporous membranes with average pore diameter larger than 50 nm, mesoporous membranes with average pore diameter in the range between 2 nm and 50 nm, and microporous membranes with average pore diameter less than 2 nm. The micropores can be further classified into subgroups by the diameter: supermicropores (1.4 to 3.2 nm), micropores (0.5 to 1.4 nm), and ultramicropores (<0.5 nm) [17].

Pore size and distribution, openness (volume fraction) and the nature of the pores to a great extent decide a porous inorganic membrane's permeability and permselectivity. Higher porosity membranes have a more open porous structure, thus generally leading to higher permeation rates for the same pore size. The nature of the pores determines the mechanisms of gas stream transport through a porous membrane, and consequently the membrane's separation properties. Generally, inorganic membranes do not exhibit a high *permeability* and a high *permselectivity* simultaneously.

In gas separation, there are six possible transportation mechanisms [18-20]. An overview of the transportation mechanisms is shown in Table 1-2.

From the table, it can be seen that viscous flow, molecular diffusion, and Knudsen diffusion occur in macro- and meso-pores, but viscous flow and molecular diffusion do not separate species. However they can affect the total flow resistance of the membrane system. Knudsen diffusion, surface diffusion, multilayer diffusion, capillary condensation, and molecular sieving are responsible for gas separations.

Table 1-2 Transportation regimes in porous membrane

Transport type	Pore diameter	Selectivity
Viscous flow	$d > 20\ nm$	-
Molecular diffusion	$d > 10\ nm$	-
Knudsen diffusion	$2 < d < 100\ nm$	$1/\sqrt{M}$
Surface diffusion		+
Capillary condensation/ multilayer diffusion		++
Molecular sieving (Size exclusion)	$d < 1.5\ nm$	++

The separation mechanism of Knudsen diffusion is based on the collisions between molecules and the pore surface. When the mean free path length of the molecules is larger than the characteristic pore diameter, the permeating species collide with the pore surfaces more frequently than with other molecules. As shown in equation (1-1), smaller molecules have longer mean free path length because the diameter is shorter. Mean free path length is proportional to temperature and inversely proportional to pressure.

$$\lambda = \frac{kT}{\sqrt{2}\pi d_p^2 P} \tag{1-1}$$

As shown in equation (1-2), the separation factor of Knudsen diffusion α^* depends on the square root of the molecular weight ratio of the gases separated, where *F* and *M* represent the permeation fluxes and molecular weights of the gas species *A* and *B*.

$$\alpha^* = \frac{F_A}{F_B} = \sqrt{\frac{M_B}{M_A}} \tag{1-2}$$

$$K_n = \frac{2\lambda}{d_p} \tag{1-3}$$

Knudsen number K_n in equation (1-3) generally defines the three regimes of gas diffusion (also refer to Table 1-2): (1) for viscous flow, $K_n \ll 1$; (2) for

Knudsen diffusion, $K_n \gg 1$; and (3) for transition flow, $0.01 \leq K_n \leq 10$. Viscous and transition flow are non-selective. Generally speaking, when λ is ten times larger than d_p, Knudsen diffusion becomes dominant [18]. In the Knudsen flow regime, the mean free path of gases is comparable to the pore diameter.

As equation (1-2) implies, the separation is only effective for those gases with large difference in molecular weights. Since the selectivity between molecules in this regime is usually low, Knudsen flow is not effective in gas separation. As equation (1-4) shows [21], Knudsen permeance is not a function of pressure. It is proportional to $1/\sqrt{T}$.

$$F_K = \frac{2\varepsilon\gamma}{3\tau L}\sqrt{\frac{8}{\pi RTM}} \tag{1-4}$$

Surface diffusion, multilayer diffusion and capillary condensation are more effective separation mechanisms than Knudsen diffusion. Surface diffusion occurs when gas mixtures interact with the inner wall materials. Chemical properties of the membrane surface play an important role in gas surface diffusion.

In porous membranes meso-pores and micro-pores contribute to selectivity. In mesoporous membranes, the dominant transport mechanism relies on the pore size and the permeating molecules which limits the selectivity of the membrane. The dominant transport mechanism in microporous membranes is molecular sieving, an activated transport mechanism, which is capable of permselectivities much greater than Knudsen.

Three main parameters are used to evaluate the performances of a gas separation membrane system: (1) the permselectivity or selectivity toward the gases to be separated. This property affects the recovery of the valuable gas in the feed and, for the most part, directs the process economics. (2) the permeate flux or permeability which is related to productivity and determines the membrane area required. (3) the membrane stability or service life which has a strong impact on the replacement and maintenance costs of the system.

1.5.2 Zeolite Membrane Reactor Configurations

By the definition of IUPAC [22], a membrane reactor combines two functional parts in one unit: a chemical reaction and a membrane-based separation. The membrane used in the reactor can be polymeric or inorganic, homogeneous or heterogeneous, symmetric or asymmetric in structure. A zeolite membrane reactor can be configured in one or more modules in these categories.

For applications of membrane-based reactive separation at high temperature, zeolite based membranes overcome the limitations associated with organic and metal membranes. Zeolites have a highly uniform pore structure, good thermal stability, and strong mechanical properties. Zeolitic materials have been used for inorganic membranes since 1930s. Zeolites that have been extensively studied for membrane applications include zeolite X, Y, ZSM-5, Silicalite-1, Na A, and sodalite [23]. However, gas separation and reactive separation applications of zeolite membranes depend strongly on the selectivity, permeability and stability characteristics of these membranes. In addition, the development of a high-performance and energy-efficient membrane-based process will depend on the

availability of highly-selective and robust zeolite membranes, fabricated with simple and cost-effective protocols [24].

Unlike traditional separation processes governed by thermodynamic equilibrium relationships, membrane separation is based primarily upon the relative rates of mass transfer in membranes. For gas separation, the transport occurs by adsorption-diffusion mechanism. Membrane selectivity is based upon the relative permeation rates of the components through the membrane. Gas diffusion obeys Fick's Law. The driving force of gas diffusion in a porous membrane is the concentration gradient through the membrane.

The catalytic function can be introduced in one of two ways: inert zeolite catalytic membrane reactor and zeolite catalytic membrane reactor. In an inert catalytic membrane, the zeolite membrane is not catalytically active and does not participate in the reaction, and simply acts as a selective separation unit for the desired products. A separate packed bed of catalyst particles promotes the chemical reaction on the feed side and the membrane selectively removes one of the products of reaction. For a *catalytic* zeolite membrane reactor, the membrane is catalytically functionalized with a precious metal, and the membrane effectively performs the catalytic reaction and separation simultaneously because the catalysis takes place on the surface of the membrane.

Based on the configurations of the zeolite membranes and the catalysts, there are three types of zeolite catalytic membrane reactor modules [25], as shown in Figure 1-10. An extractor-type zeolite catalytic membrane reactor increases the conversion by selectively removing a product or an intermediate from the reaction

system whose conversion in a traditional reactor is limited by the thermodynamic equilibrium (cases (a) and (b) in Figure 1-10). In the examples shown in case (a), the conversion to olefins from alkanes or other hydrocarbons by dehydrogenation was enhanced by the removal of product hydrogen from the feed side. This reactor is ideal for the ethane dehydrogenation to ethylene [26].

As shown in case (c) in Figure 1-10, the reactant distributor type membrane reactor works like an extractor type membrane reactor inversely. A typical example of this reactor's application is partial oxidation reaction of butane to maleic anhydride [27]. By controlling lower partial pressure of one reactant, it is expected to improve the selectivity of the target product. Oxidative dehydrogenation of lower alkanes like ethane [28-33] and propane [34, 35] to make olefins were carried out in this type of reactors by conducting oxygen or oxygen anions trough the membrane to the reaction system. There are many benefits to using a distributor membrane for oxidation reactions, such as achieving higher selectivity, more even reaction heat distribution, and working beyond flammability regions. The membrane in the contactor type of reactor shown in (d) is catalytically functionalized. It functions as catalyst and separator at the same time. In this configuration the reactants are located at different sides of the membrane and must diffuse through the zeolite layer to react.

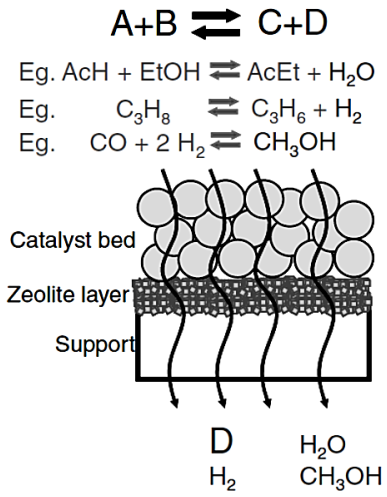

(a) Equilibrium displacement (Extractor type)

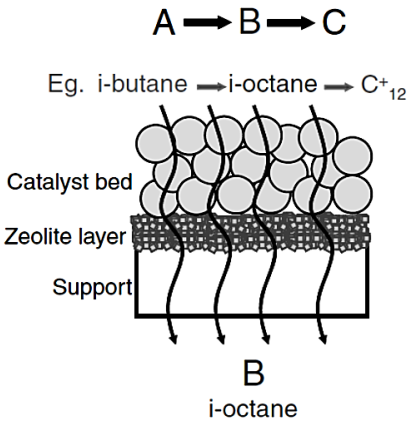

(b) Selective removal of intermediate (Extractor type)

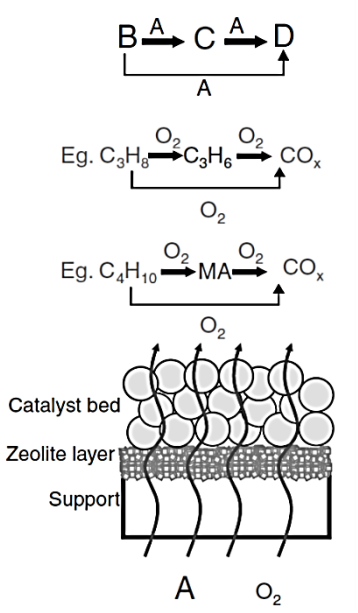

(c) Reactant distribution (Distributor type)

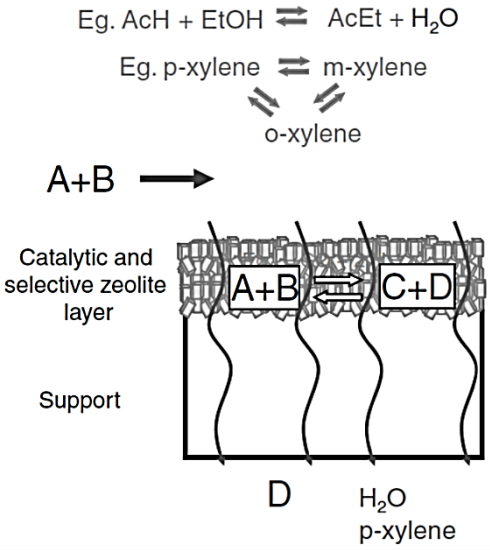

(d) Catalytic membrane with product removal (Contactor type)

Figure 1-10 Types of Zeolite Catalytic Membrane Reactors

1.6 Research Objectives

The objective of this work was to demonstrate the concept of using natural zeolites in a membrane reactor to increase the conversion of ethane and yield of ethylene at temperatures below conventional thermal cracking conditions. This work also sought to demonstrate the benefits of using ETS-2 as a catalyst substrate for ethane dehydrogenation.

.

Chapter 2. Characterizations and Product Analysis

2.1 Characterization methods

2.1.1 X-ray diffraction (XRD)

The phase identification and structural analysis of zeolites and catalyst materials were characterized by X-ray diffraction (XRD) using Rigaku Gigerflex 2173 diffractometer with Co tube x-ray source (Co K_α, $\lambda = 1.79021\text{Å}$), and a vertical goniometer with a graphite monochromator as K_β filter.

Testing conditions were: 38 kV, 38 mA, scan speed 2 degree/min, step width 0.02 degree, and scan range 5 to 90 degree. XRD samples data were compared to the database from the International Center for Diffraction Data-Powder Diffraction File (ICDD-PDF) to identify crystalline phases present in the samples.

For natural zeolites, both powder and thin surface samples were tested. For catalysts and supports, all samples were fine powder. All XRD data were collected at room temperature.

2.1.2 Pore Size Distribution, Specific Surface Area, and Pt Particle Dispersion

The BJH (Barret-Joyner-Halenda) and Horvath-Kawazoe (HK) pore size distribution (PSD) of the natural zeolite modernite were calculated from the N_2 adsorption isotherm at 77K using a Quantachrome Instruments AUTOSORB-1.

The specific surface area of samples was calculated using the Brunauer-Emmett-Teller (BET) method. For the natural zeolite mordenite, the sample dried at 120 °C was degassed at 150 °C for two hours. Other samples were degased at 200 °C for two hours before adsorption.

Hydrogen chemisorption measurements for the Pt catalysts were performed on a Micrometrics ASAP 2020C instrument. Samples of ~ 0.5 g were first reduced in hydrogen at 400 °C for 30 minutes, cooled down under vacuum to 35 °C, and then evacuated for an additional 10 minutes at this temperature before the hydrogen isotherm was collected at the same temperature. A total of 14 points were collected for the hydrogen isotherm between 0.25 and 0.60 kPa. Dispersions were estimated assuming the adsorption of one hydrogen atom per surface Pt atom.

2.1.3 X-ray photoelectron spectroscopy (XPS)

The XPS measurements were carried out on a Kratos Axis 165 X-ray photoelectron spectrometer with a Mono Al Kα source (hν = 1486.6 eV) (operated at 15 mA and 14 kV). The survey spectra were collected with analyzer pass energy of 160 eV and a step of 0.4 eV; the high resolution spectra were scanned with a pass energy of 20 eV and a step of 0.1 eV. During the acquisition of a spectrum, charge neutralization was applied to compensate the insulating problem of the sample. XPS signals were fitted by mixed Lorentzian–Gaussian curves using Casa XPS software. All binding energies are reported after calibration for C1s peak to match 284.8 eV.

2.1.4 TPR

Hydrogen temperature-programmed reduction (H_2-TPR) was carried out on an AutoChem 2950 HP instrument (Micromeritics, USA) equipped with thermal conductivity detector (TCD) under atmospheric pressure. About 0.5 grams of the catalyst calcined in air, at 200 °C, for one hour was used for the analysis. The catalysts were reduced in a flow of 10% H_2/Ar (50 ml/min) from room temperature to 500 °C with a heating rate of 5 °C/min.

2.1.5 SEM and EDX

The SEM used was a Hitachi S-2700 Scanning Electron Microscope (SEM) equipped with a PGT (Princeton Gamma-Tech) IMIX digital imaging system and a PGT PRISM IG (Intrinsic Germanium) detector for Energy Dispersive X-Ray Analysis (EDX). Backscattered Electron Detector - GW Electronics System 47 four quadrant solid state Backscattered Electron Detector. Samples for EDX were coated with carbon.

The high-resolution scanning electron micrographs were obtained using a JEOL 6301F field emission scanning electron microscope. Samples for high-resolution images were coated with gold.

2.1.6 TEM

The morphology of Pt particles on catalysts were characterized by transmission electron microscopy (TEM) on a JEOL 2100 transmission electron

microscope operating at 200 kV. Fine powder samples were loaded on copper mesh and coated with carbon.

2.1.7 TGA and TG-MS

The thermogravimetric analysis of natural zeolites was conducted on TA Instruments TGA Q500. N_2 was used as the inert sweeping gas at a flow rate of 40 ml/min while between 15 to 25 mg of fine powder sample was used for analysis. Heating rate was 10 °C/min from room temperature to 1000 °C.

The analysis of coke deposits on spent catalysts was conducted using TG-MS. The TG-MS plots were collected using a TA Instruments Q500 TGA coupled to a Pfeiffer Omnistar QMA 200 residual gas analyzer. TG scans were run using a balance purge rate of 5 ml/min Ar and a sample (air) purge rate of 180 ml/min. Samples were loaded on platinum pans and heated at a rate of 10 °C/min from ambient to 600 °C.

The mass spectrometer was configured with a stainless steel capillary heated to 200 °C and connected to the TGA by means of a stainless steel adapter and a ¼" branch T-fitting. The capillary was positioned at the center of the tee close to the furnace exhaust to sample the evolved gases. The exhaust end of the T-fitting was connected to a 6 m length of ¼" OD tubing that prevented back-diffusion of atmospheric components and led to a fume hood exhaust. Experiments were run in MID mode with fragments at m/z = 18 and 44 tracked over time. These fragments, associated with water and carbon dioxide respectively, were found to be the most diagnostic signals associated with the combustion of the coke. To start data

collection, the two instruments were manually synchronized. An uncertainty of a few tenths of a degree for the starting temperature can be expected between the TG and MS plots.

2.1.8 Dilatometry test

The dilatometric behavior of natural zeolite mordenite was carried out on a L75 PT Vertical Dialtometer (Linseis Thermal Analysis). About 0.3 g of each powder sample was pressed into cylindrical rods using a special die and an isostatic press (Top Industrie) under a pressure of 300 MPa. The rods were about 10 mm in length and 5 mm in diameter. The pressed rods were heated from room temperature to 1000 °C under air with a rate of 10 °C/min. After maintaining a temperature of 1000 °C for one hour, the sample was cooled down at a rate of 10 °C/min. The thermodilatometric data were processed under the form of curves, which report the percent variation of cylinder length ($\Delta L/L_0$, %) as a function of temperature.

2.2 Gas Product Analysis

An on-line GC (Bruker 450-GC) with automatic sampling valves was used to analyze gas products. The packed column was Hysep D (80-100 mesh) stainless steel (ϕ1/8", 3 meters), equipped with a thermal conductivity detector (TCD). Argon (99.99%, Praxair) was used as GC carrier gas.

Part I: The Use of Natural Zeolite Mordenite in a Membrane Reactor for Ethane Dehydrogenation

Chapter 3. Characterization of Natural Mordenite Zeolite

3.1 Introduction

Zeolites are hydrated crystalline alumina-silicates that contain alkali and alkaline earth metals. The name zeolite was created by the Swedish mineralogist Axel Fredrick Cronstedt in 1756 and it means "boiling stone" in Greek [36]. More than 40 naturally occurring zeolites have been identified in the past two centuries. Chabazite, clinoptilolite, erionite, ferrierite, mordenite, and phillipsite are the six most industrially important natural zeolites [37]. Mordenite was first discovered in 1864 in Morden, King's County, Nova Scotia, Canada by How [38] and, as per tradition, was named after the locality. Mordenite mineral deposits occur in more than 348 locations in 39 countries including Antarctic [39], as shown in Figure 3-1.

New Zealand is one of the countries with the most abundant mordenite deposits. About 250,000 years ago, massive volcanic ash formed thick sediment beds in lakes. Hot water transformed those clay beds into soft rocks with ordered internal structures. Over time the lakes drained due to severe block faulting and the deeply buried structured clay rocks became zeolites. Mordenite and clinoptilolite are the predominant natural zeolites in New Zealand. Due to their diagenesis, they are highly matured and mechanically strong and cannot be broken down into constituent clays.

All samples of natural zeolite mordenite used in the thesis work are from New Zealand.

Mordenite was chosen as potential membrane reactor material because it is physically and chemically stable at the required working temperatures and it has suitable pore structures to achieve good selectivity for hydrogen removal. In addition, it is very economical due to its abundance in nature. Its pore structure, unique to naturally occurring zeolites, is only large enough to admit molecules 3 Å and smaller making it ideal for hydrogen separation from larger hydrocarbons.

Figure 3-1 Localities of natural zeolite mordenite

3.2 Channel Sizes of Zeolite Mordenite

Zeolite mordenite has a big elliptical 12-ring channel and an 8-ring (2.6 × 5.7Å) channel along [001] with two interconnected 8-ring channels (3.4 × 4.8Å) along [010]. Figure 3-2 shows an ideal framework of mordenite. The 8-ring holes of successive sheets do not align to make channels along [010]. Since the 8-ring

channel along [001] is smaller than most gases' kinetic diameter [40] (He: 2.6 Å, H_2: 2.8 Å, CO_2: 3.3 Å, O_2: 3.4Å, N_2: 3.6Å), the 8-ring opening acts as a connecting window. Practically, mordenite is one-dimensionally permeable along [001]. A more visual demonstration is shown in Figure 3-3 [41]. The figure clearly shows that the 8-ring channels are highly compressed and not accessible to most molecules or ions, and there is no direct connections between 12-ring channels. Although the framework structure appears like it would admit larger molecules, the position and types of the cations inside the framework prevent molecules larger than about 3 Å from entering the structure.

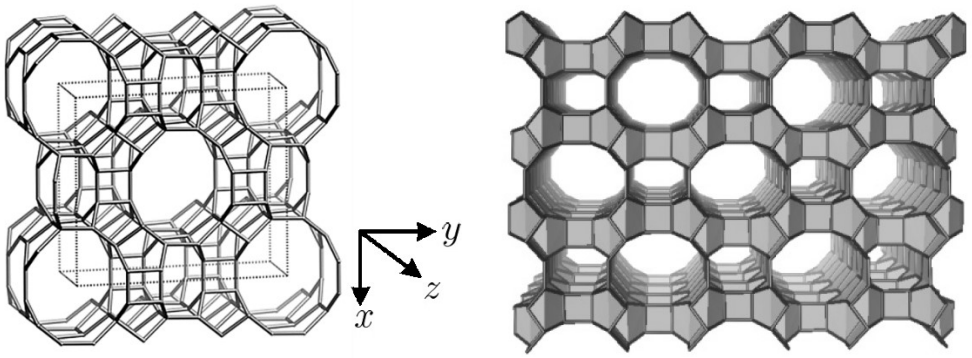

Framework viewed along [001]

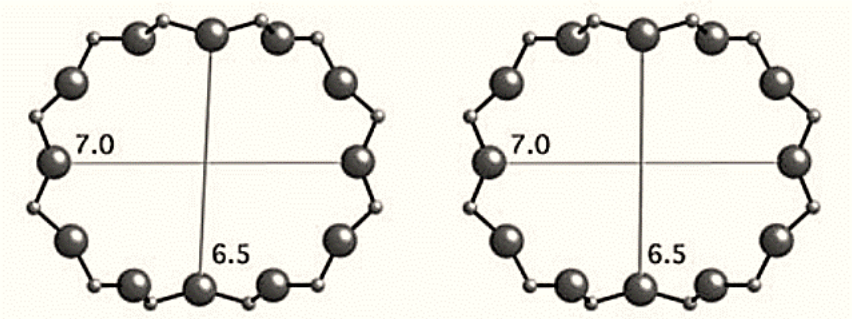

12-ring viewed along [001]

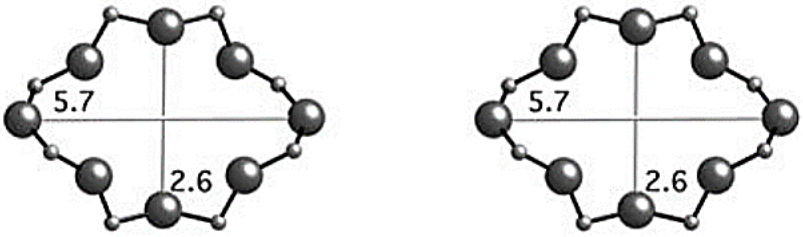

8-ring viewed along [001] between 12-ring channels

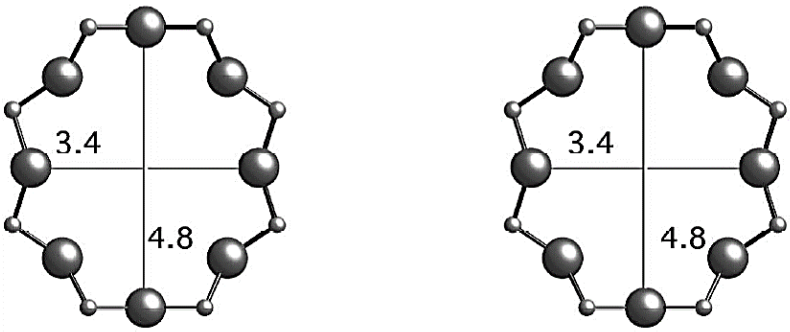

8-ring viewed along [010]

Figure 3-2 Framework and ring sizes or mordenite

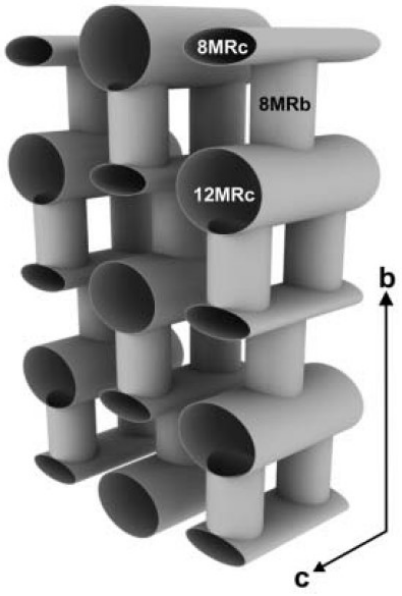

Figure 3-3 One-dimensionally accessible channel system in mordenite

3.3 XRD

Both the powder and the thin membrane surface samples of natural zeolite mordenite were treated at different temperatures.

Figure 3-4 shows that the sample of natural zeolite mordenite contained a quartz impurity. From Figure 3-5, it can be seen that the natural mordenite samples were thermally stable at elevated temperatures. The XRD patterns show that the crystalline framework remained unchanged up to 750 °C.

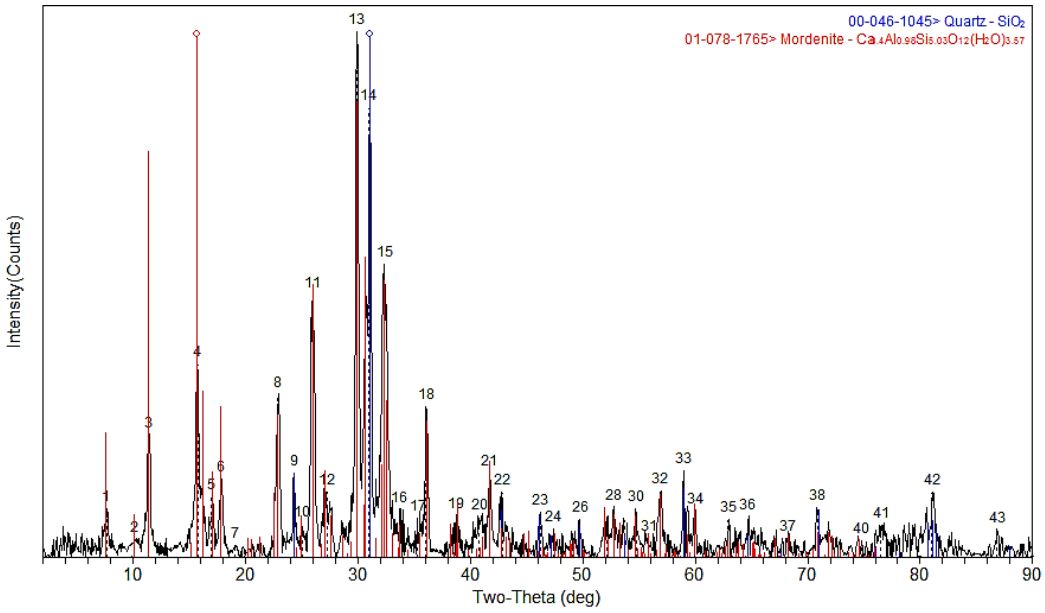

Figure 3-4 XRD patterns of natural zeolite mordenite before calcination

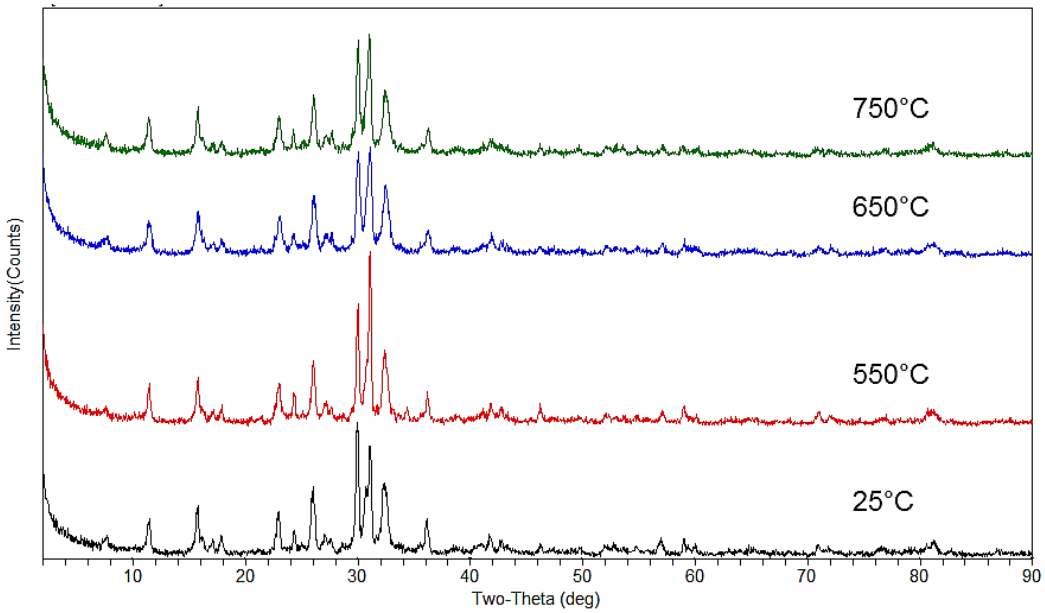

Figure 3-5 XRD patterns of natural zeolite mordenite treated at different temperatures for 4 hours

3.4 Scanning Electron Microscopy (SEM)

In Figure 3-6, cross-section images clearly show that there were plenty of needle-like crystals in natural mordenite samples. Well-matured natural zeolite mordenite has a needle-like crystal structure while the layers stacked on each other indicate the presence of multiple crystals. This multiple-layer structure reveals the growing process of naturally occurring zeolite mordenite.

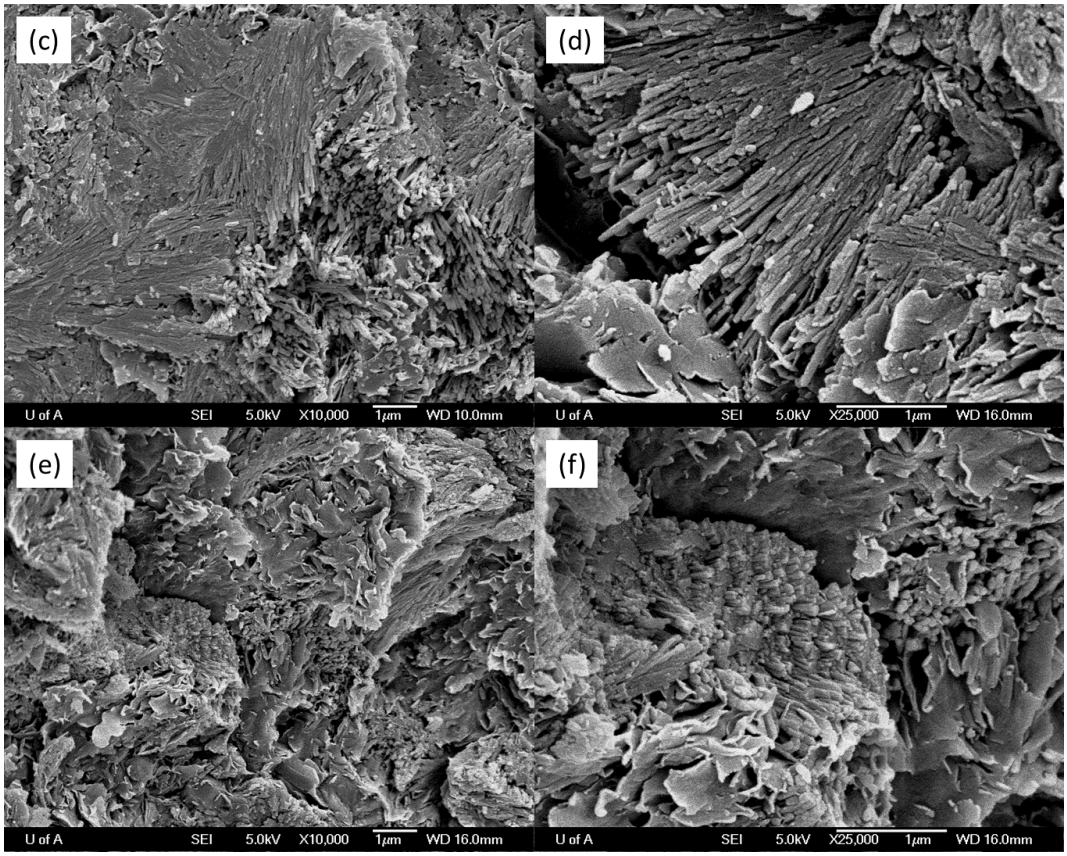

Figure 3-6 SEM images of cross-section of natural zeolite mordenite

3.5 Thermal Analysis

3.5.1 Thermogravimetric Analysis (TGA)

Figure 3-7 shows the TGA curve of the natural zeolite mordenite. The total weight loss was about 12.1 wt%. The weight losses at ≤ 150 °C, 150-200 °C, 200-300 °C, 300-400 °C, 400-670 °C were 6.2 wt% (about 51% of the total weight loss), 1.1 wt% (9% of the total weight loss), 1.3 wt% (10.7% of the total weight loss), 1.1 wt% (9% of the total weight loss), and 2.2 wt% (18.2% of the total weight loss) respectively. After 660 °C, there was nearly no weight loss (~ 0.2 wt%).

The weight loss at < 200 °C is caused by dehydration of the zeolite. For the zeolites with high kinetic diameter, like mordenite, the main dehydration temperature is lower than 200 °C. The so-called zeolitic water is free water absorbed in capillary channels and external surface as well. The water dipole is attracted to the oxygen electron density in the SiO_4 and AlO_4 tetrahedra. Free water in large channels is easy to remove because it lacks strong associations, and so the dehydration temperature is in the low range (~ 100 °C). Water associated with the cations and bound to them through ion-dipole interactions is more difficult to remove and is desorbed at higher temperatures (100-200 °C). Once all of the water associated with the cations is desorbed the remaining weight loss is due to "chemical" and "structural" water. Hydroxyl groups present in defects and at the terminus of SiO_4 and AlO_4 tetradedra can be removed at sufficiently high temperatures by condensing those hydroxyl groups to water molecules. The total amount of water content and dehydration profile of natural mordenite were in good agreement with literature reports [42]. The loss of water can cause zeolite membrane to shrink. This will be illustrated in the dilatometric analysis.

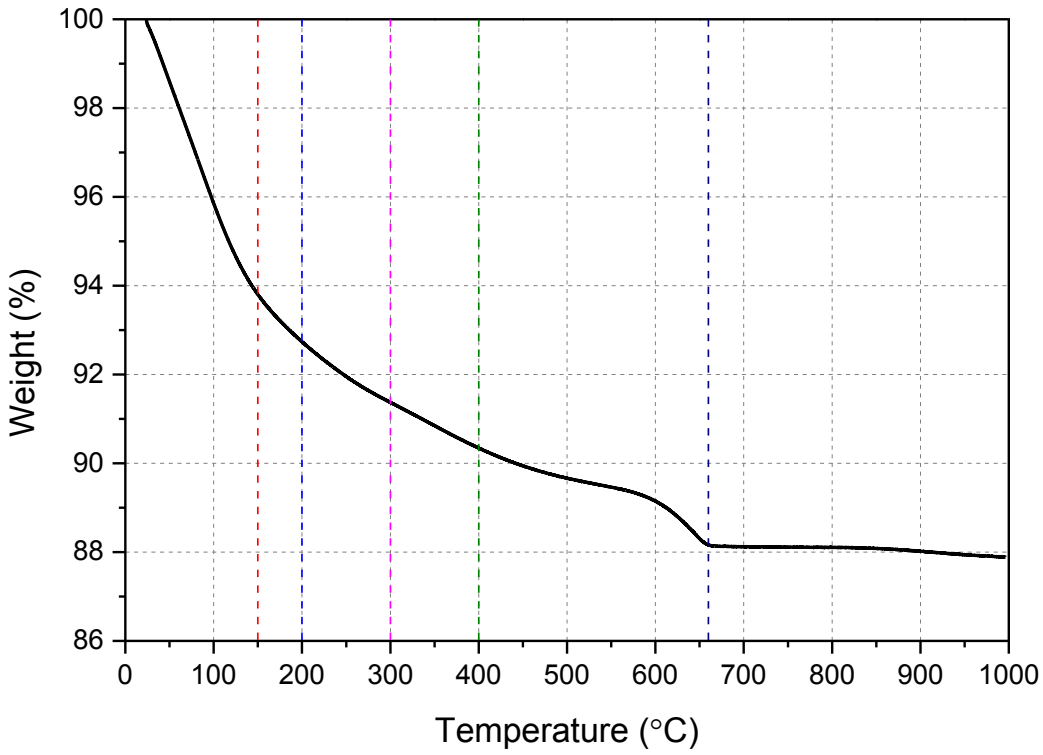

Figure 3-7 TGA profile of natural mordenite

3.5.2 Dilatometry Test

In order to understand the thermal mechanical behavior of natural zeolite mordenite, a dilatometry test was conducted.

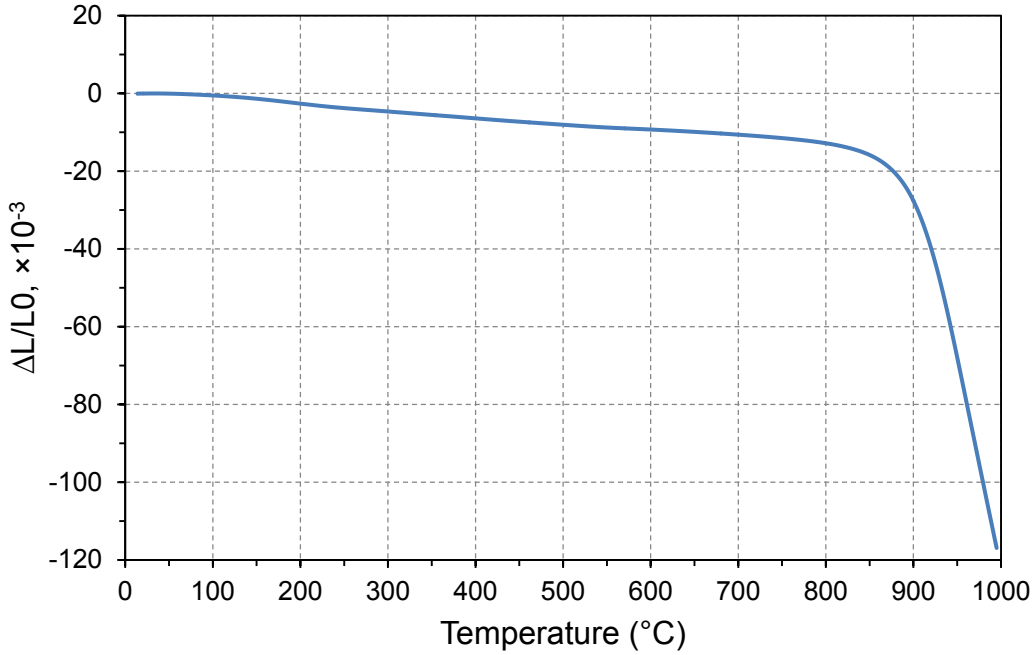

Figure 3-8 Dilatometry test of natural zeolites mordenite

Dilatometric curves of sintering for mordenite between room temperature and 1000 °C under atmospheric conditions is shown in Figure 3-8. In the region between room temperature and around 800 °C, the negative slope curve shows shrinkage of sintering behavior of the sample. The TGA curve in Figure 3-7 shows that from room temperature up to 700 °C the mordenite sample was continuously losing water, and the weight loss at 700 °C was about 98% of total weight loss. From the XRD profile in Figure 3-5, it can be seen the mordenite retained its crystal frameworks without obvious structural collapse and phase transformation. So it appears that the continuous dehydration with increased temperature was the main reason for the shrinkage. In the region between 800 °C and 1000 °C, shrinkage increased

significantly and thermal collapse of the structure occurred. Cruciani [43] reported mordenite exhibited good thermal stability above 800 °C.

For the negative thermal expansion behaviors, Sleight proposed four possible mechanisms [44]: (a) decrease of M-O bond length leading to a net cell volume contraction; (b) anisotropic thermal behavior of M-O bonds; (c) extrinsic effect of interstitial cations relocating as temperature changes; (d) transverse thermal vibrations of oxygen in M-O-M linkages.

For zeolites, the M-O bonds in the frameworks are hinged by two-coordinated oxygen and are relatively rigid. Their thermal motions have limited freedom in order to maintain structural framework. Hammonds et al developed a rigid unit mode (RUM) model to interpret and quantify the flexibility possessed by zeolites [45, 46], but it was a debated issue [43].

Martucci et al [47] carried out an *in situ* study of dehydration process of natural mordenite by X-ray synchrotron powder diffraction from 25 to 830 °C. Structure refinements indicated that the slight cell-volume contraction (~1.9 %) is related to the release of water molecules from the channels. The cell parameters *b* and *c* decreased regularly as the temperature rose. The removal of water molecules also relocated the initial Ca sites into many positions bonded to the framework oxygen. The increased interaction with the framework oxygen of Ca sites was intimately related to the distortion of the 12-ring which is in turn related to the lengthening of the *a* cell parameter. Figure 3-9 demonstrates the initial cations relocating and water molecules removing out the 12-ring channel.

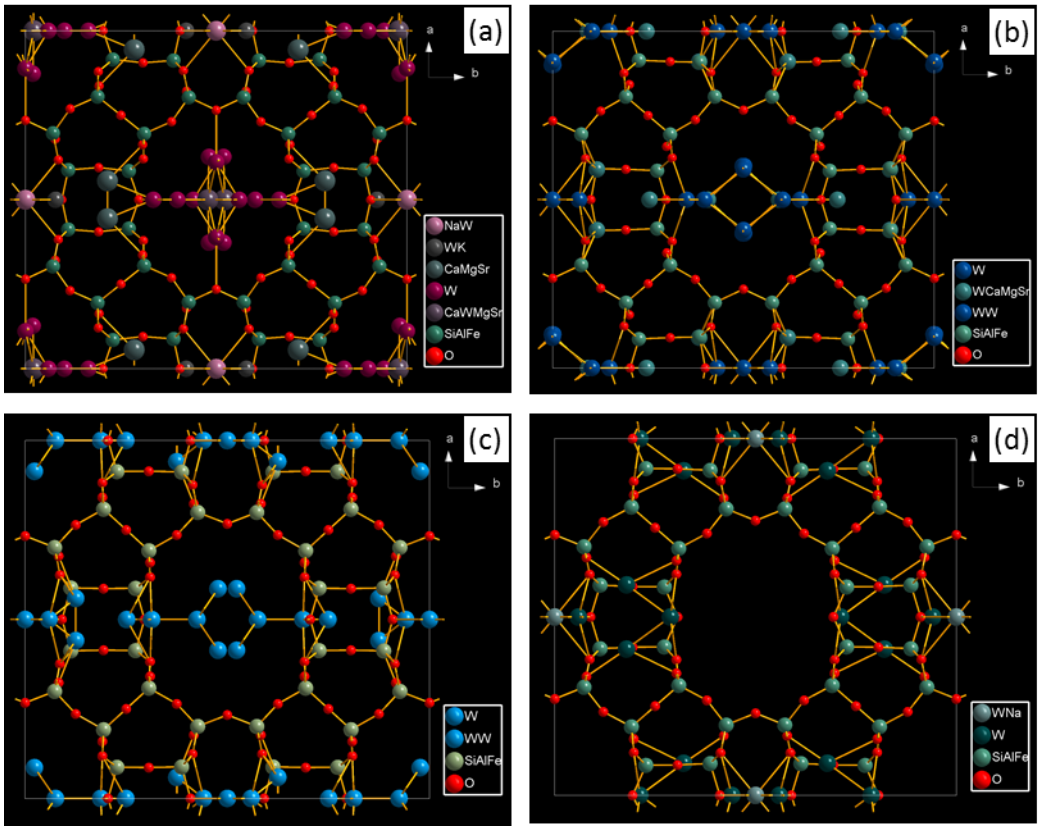

Figure 3-9 Refined natural mordenite structure viewed along [001] at different temperatures: (a) 25 °C, (b) 200 °C, (c) 450 °C, (d) 830 °C

3.6 BET of Mordenite

Specific surface area calculated with the Brunauer-Emmett-Teller (BET) method. The BET equation is shown in Equation (3-1).

$$\frac{1}{W\left(\frac{P_0}{P}-1\right)} = \frac{1}{W_m C} + \frac{C-1}{W_m C}\left(\frac{P}{P_0}\right) \tag{3-1}$$

$$C = exp\left(\frac{E_1 - E_L}{RT}\right) \quad (3\text{-}2)$$

Figure 3-10 shows the BET surface area changes of the mordenite treated at different temperatures. In general, the measured surface area was similar to literature reports [48]. From the figure, it can be seen that the sample calcined at 200 °C for four hours has the largest surface area. As water was removed out from the inner channels, the surface area increased. Martucci and coworkers [47] found that at 200 °C the diameter of the 8-ring along [001] was the largest, decreasing with further temperature raise. A big ring aperture exposes more internal surfaces to N_2 and may be the cause of surface area increase.

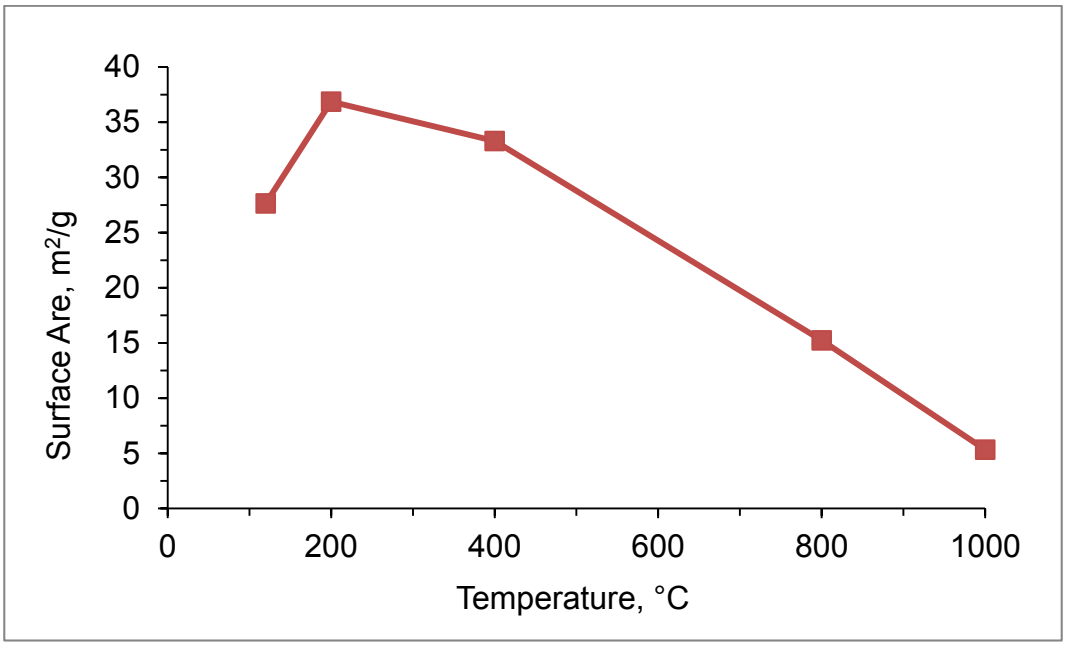

Figure 3-10 BET surface area of natural mordenite treated at different temperatures

Pore size distribution determined with Horvath-Kawazoe (HK) method [49] is shown in Figure 3-11. Many pore size distribution methods are derived from the Kelvin equation that describes the phenomena of capillary condensation. The HK method was derived independently from the Kelvin equation, which more accurately describes micropore (< 20 Å) size distribution. The HK equation is shown in Equation (3-3).

$$RT\ ln\left(\frac{P}{P_0}\right) = K\frac{N_S A_S + N_A A_A}{\sigma^4(l-d)}\left[\frac{\sigma^4}{3\left(l-\frac{d}{2}\right)^3} - \frac{\sigma^{10}}{9\left(l-\frac{d}{2}\right)^9} - \frac{\sigma^4}{3\left(\frac{d}{2}\right)^3} + \frac{\sigma^{10}}{9\left(\frac{d}{2}\right)^9}\right] \quad (3\text{-}3)$$

$$A_S = \frac{6mc^2\alpha_S\alpha_A}{\left(\frac{\alpha_S}{\chi_S}+\frac{\alpha_A}{\chi_A}\right)} \quad (3\text{-}4)$$

$$A_A = \frac{3mc^2\alpha_A\chi_A}{2} \quad (3\text{-}5)$$

$$\sigma = \frac{0.858d}{2} \quad (3\text{-}6)$$

$$d = d_s + d_A \quad (3\text{-}7)$$

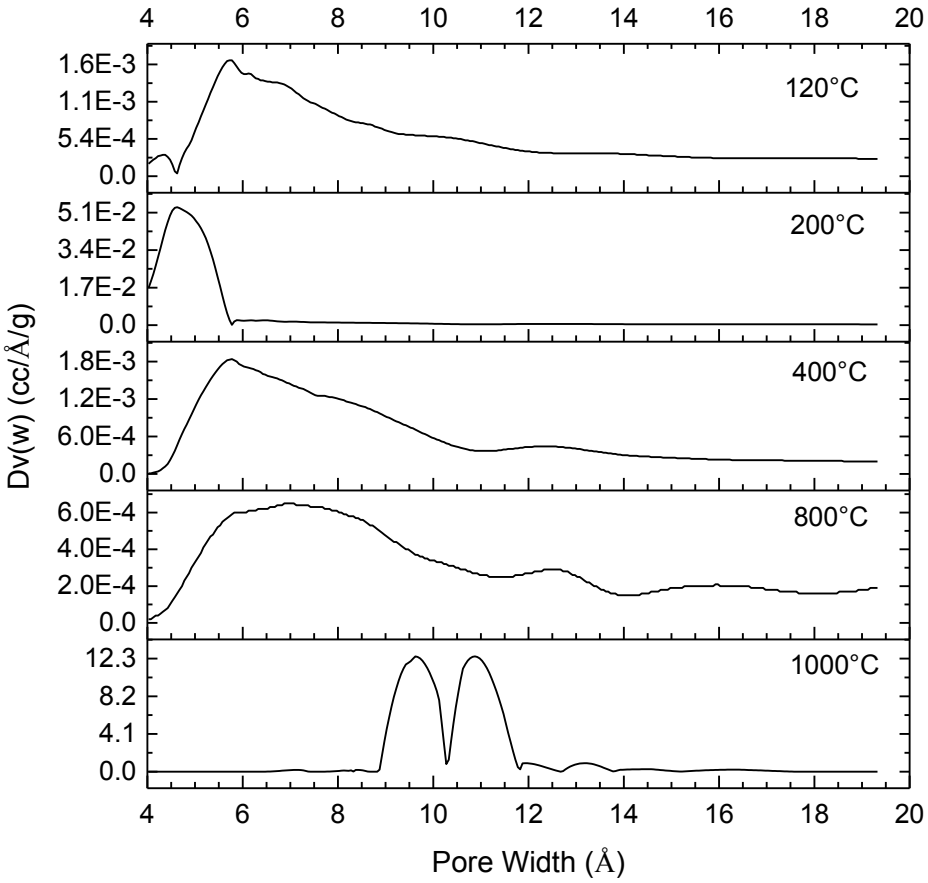

Figure 3-11 Pore size distribution of natural mordenite calculated by HK method

Figure 3-11 clearly shows the micropore size distribution of the natural mordenite treated at different temperatures. As treating temperature increased, the mean pore size increased, and the size distribution became wider. Both pore size and distribution were well predicted by the removal of water adsorbed in channels and redistribution of initial cations through water removal, which made N_2 more accessible to the micropores. At 800 °C, a higher number of large pores with a wide range of sizes are present. These big pores may be caused by the collapse of some of the micro frameworks. When temperature increased to 1000 °C, micropore size

distribution narrowed down to two main sizes: 9.5Å and 11Å. This phenomenon may further confirm the collapse of micro structures.

The Barrett-Joyner-Halenda (BJH) method provides quantitative specific surface area and pore size distribution information primarily for mesoporous and macroporous materials but also some semi-quantitative information on microporous materials. The equations for pore size distribution calculations are shown in equations (3-8) and (3-9).

$$V_{pn} = \left(\frac{r_{pn}}{r_{Kn}+\frac{\Delta t_n}{2}}\right)^2 \left(\Delta V_n - \Delta t_n \sum_{j=1}^{n-1} A c_j\right) \tag{3-8}$$

$$c = \frac{\overline{r_c}}{\overline{r_p}} = \frac{\overline{r_p}-t_{\overline{r}}}{\overline{r_p}} \tag{3-9}$$

Figure 3-12 shows the mesopore size (> 20 Å) distribution of mordenite treated at different temperatures. The figure clearly indicates that low temperature treated samples lack mesopores. However, when treated at 800 °C and 1000 °C, 20 Å and 35 Å mesopores appeared respectively. The mesopores present at higher temperatures provide further evidence of the structure collapse.

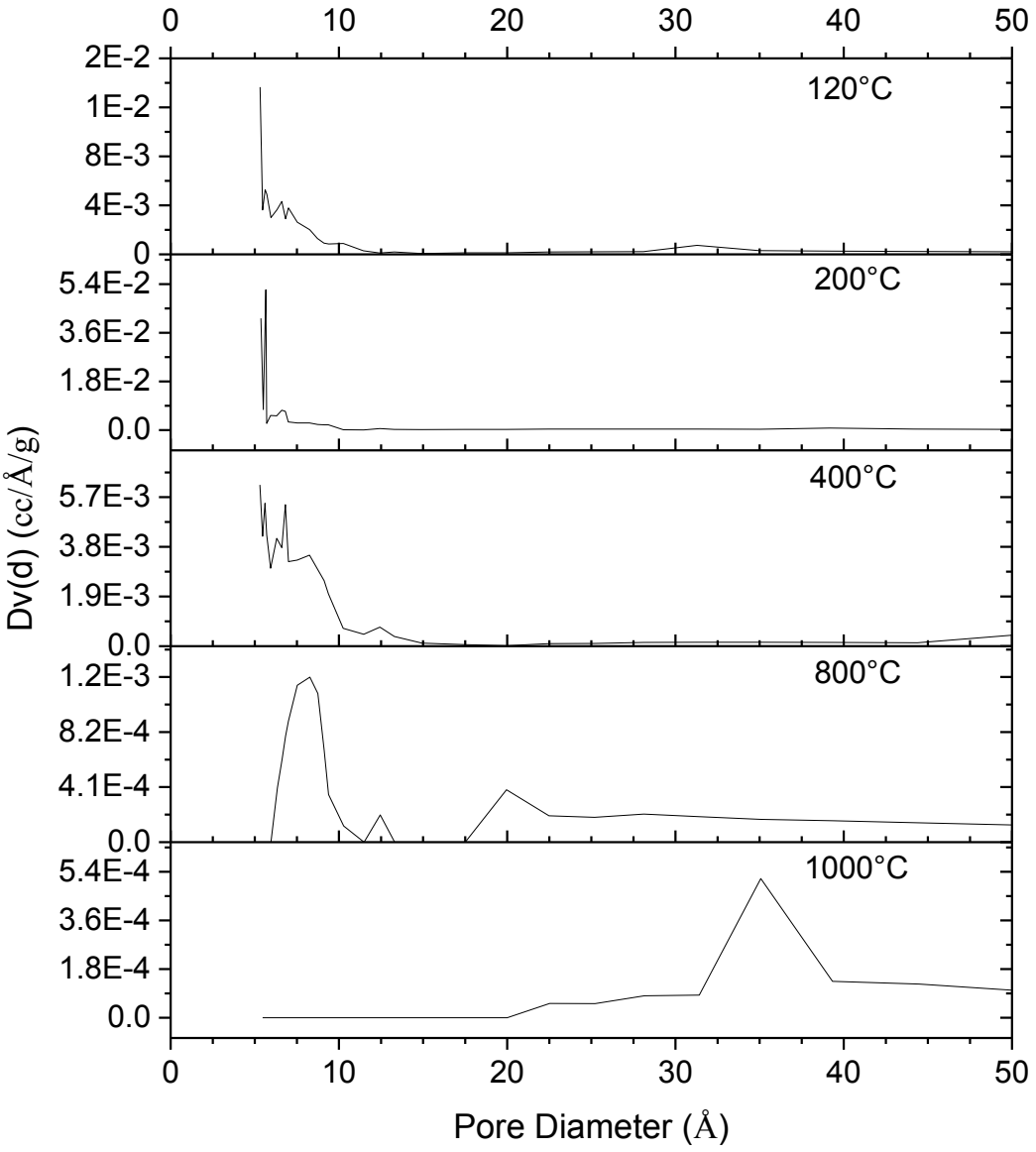

Figure 3-12 Pore size distribution of natural mordenite calculated by BJH method

3.7 Chemical compositions of natural mordenite zeolite

The chemical composition of natural zeolite mordenite from New Zealand is summarized in Table 3-1. Data show that Si/Al molar ratio is 5.10 $\left(\frac{\mathrm{Si}}{\mathrm{Al+Fe^{3+}}} = 4.36\right)$,

falling in the typical range of Si/Al of mordenite [50]. The sample had low concentration of alkali metals like sodium and potassium, but very high calcium concentration, which was double that of the typical samples [51].

Table 3-1 Chemical composition of natural zeolite mordenite

Compound	wt %
LOI*	15.36
Na_2O	1.60
MgO	0.57
Al_2O_3	9.38
SiO_2	56.42
P_2O_5	0.12
SO_3	0.080
K_2O	0.70
CaO	12.24
TiO_2	0.27
Cr_2O_3	0.0035
MnO	0.072
Fe_2O_3	2.49
NiO	0.0034
CuO	0.0038
ZnO	0.0078
Rb_2O	0.0015
SrO	0.040
Y_2O_3	0.0052
ZrO_2	0.011
Total	99.38

* LOI = loss on ignition at 950 °C for 1 hour

Natural zeolite mordenite is classified in the high thermal stability category [52]. XRD and dilatometry results show that it is stable up to 800 °C. Pore size distribution measurements show that mordenite has uniform pore size. All these features make the mordenite a strong candidate as a high temperature membrane material for membrane reactors.

Chapter 4. Packed Bed Membrane Reactor for Ethane Dehydrogenation*

4.1 Introduction

Ethylene, the simplest olefin, is a fundamental intermediate in petrochemical industry for the productions of plastics, solvents, cosmetics, pneumatics, paints, packaging and more. The global ethylene capacity reached 150 million tons in 2012, and is predicted to have a growth rate of 3.4% per year [4]. The global sales of ethylene reach $148 billion annually [8].

Currently, tube furnace steam cracking process is the dominant technology for ethylene production, which accounts for about 99% of global ethylene production process. Among the hydrocarbon feedstock for ethylene production, ethane has the lowest cost and the highest ethylene yield. Heavier feedstock produces more low value by-products. Steam cracking process for ethylene production occurs at high temperature because hydrocarbon dehydrogenation is an endothermic reaction (Equation (**4-1**).

* Published: A. M. Avila, Z. Yu, S. Fazli, J. A. Sawada, and S. M. Kuznicki: "Hydrogen-Selective Natural Mordenite in a Membrane Reactor for Ethane Dehydrogenation", *Microporous and Mesoporous Materials*, **2014**, 190 (0), 301-308

$$C_2H_6 \rightleftharpoons H_2 + C_2H_4 \qquad \Delta_r H_{298} = 136\,\mathrm{kJ/mol} \tag{4-1}$$

The ethane diluted with steam flows through high temperature tubes at high velocity to achieve a short residence time (less than 1 second). Typical decomposition reaction temperatures are between 800 °C to 850 °C. To maintain the high reaction temperature, furnace skin temperature is usually between 1100 °C to 1200 °C. Such high temperature operation causes serious side reactions in addition to being energy intensive.

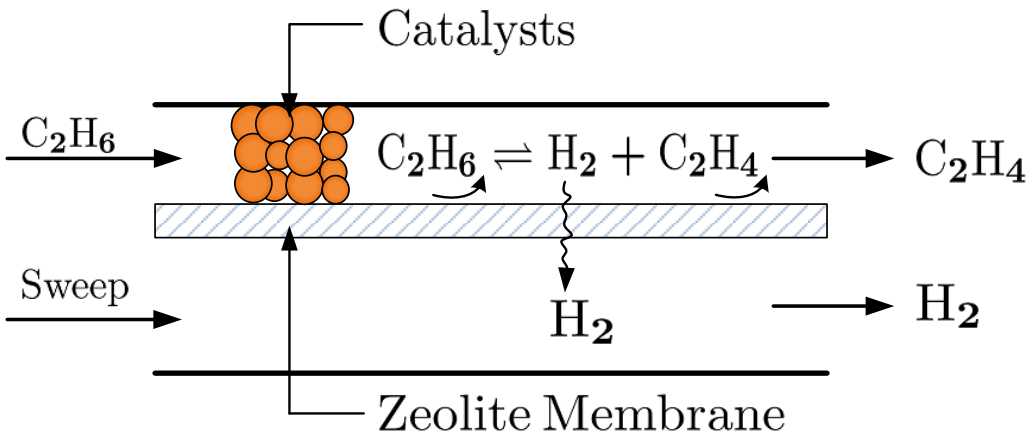

Figure 4-1 Illustration of membrane reactor concept for ethane dehydrogenation

As illustrated in Figure 4-1, selective removal of the product hydrogen from the reaction system enables shifting the ethane dehydrogenation reaction to production of ethylene. The dehydrogenation catalysts help the reaction reach equilibrium quickly and suppress side reactions at relatively low temperature.

A membrane reactor that selectively removes hydrogen can shift the conversion of ethane dehydrogenation to values above the thermodynamic equilibrium. High conversion levels at lower temperature result in increased energy efficiency of the system [53-56].

Ethane dehydrogenation has been investigated with various catalytic membrane reactors. Champagnie and coworkers [57] studied ethane dehydrogenation in a tubular alumina ceramic membrane reactor. The ceramic membrane was impregnated with 5wt% Pt as a cracking catalyst. The feedstock ethane was diluted with argon and hydrogen. The driving force for hydrogen separation was Knudsen diffusion. Gobina and coworkers [58-61] studied the packed-bed membrane reactor. The membrane was a thin layer of Pd-Ag alloy supported on porous Vycor glass tube. Ethane was diluted with nitrogen. Szegner and coworkers [62] studied ethane dehydrogenation in a packed-bed membrane reactor. The catalyst was Pt-Sn/Al_2O_3 pellets. Membrane used in the reactor was inert and only functioned as a separator. Feed gas was diluted with hydrogen and argon. The results showed that the conversion of ethane dehydrogenation was higher than that of equilibrium. Ethane dehydrogenation is a volume expansion reaction, so diluting the reaction system with inert gas could also shift the conversion above the equilibrium.

Among the membrane reactors for ethane dehydrogenation, the extractor-type membrane reactors is best suited, because the conversion is enhanced by selectively removing hydrogen from the reaction system shifting the reaction to the favorable direction. Hydrogen removal by the selective membrane is based on the fact that

hydrogen permeation is faster than that of hydrocarbons. However, at high temperatures the perm-selectivity of hydrogen is just slightly higher than that in the Knudsen flow, because the Knudsen separation factor is proportional to the square root of the ratio of molecular weights. In order to increase conversion further at these temperatures a higher selective membrane is required.

The unique internal channel system and pore sizes of some zeolitic membranes allow them higher selectivity to hydrogen permeation, making them good candidates as high temperature membrane reactors. Natural zeolite mordenite has uniform a one-dimensional channel system which has pores that can be small enough to admit only hydrogen leading to a higher selectivity toward hydrogen. The studies on gas separation [37] proved its perm-selectivity to hydrogen in the separation of hydrogen and ethane mixture [63].

The main objective of this work is to investigate ethane dehydrogenation reaction in a packed-bed membrane reactor (PBMR) that uses natural zeolite mordenite as membrane to extract hydrogen from the reaction system. The Pt-Sn/Al_2O_3 pellets were used as the catalyst. The PBMR operated in both the membrane reactor and a conventional packed-bed reactor mode by dramatically switching the sweeping gas on and off to evaluate the relative effect of the membrane on ethane conversion.

4.2 Experimental

4.2.1 The Catalyst

The catalyst used for the PBMR was 1wt%Pt-0.3wt%Sn/Al_2O_3 (Alfa Aesar product, USA, reduced). The spherical alumina pellet size ranged from 1-2 mm. The catalyst was dried at 110 °C for four hours before use.

4.2.2 Membrane Preparation

Mordenite membrane disks were prepared from the raw natural monolithic mordenite fragments from Paradise Quarry Limited, New Zealand. The rock pieces were shaped to $5 \times 5 \times 5\ cm$ cubes using a Rock Rascal Model TM Combination Trim Saw/Grinder equipped with a MK-303 diamond lapidary saw blade. The cubes were sliced into $\emptyset 19 \times 1.5\ mm$ disks by water jet cutting or by hand. The disks were polished with a rotating diamond polishing lapidary disk (180 mesh, Fac-Ette Manufacturing Inc.), washed in ultrasonic bath for 30 minutes, and then dried at 110 °C for four hours. Finished membrane disks were activated at 750 °C for four hours before use. Figure 4-2 show the steps of membrane disks preparation from the natural mordenite zeolite.

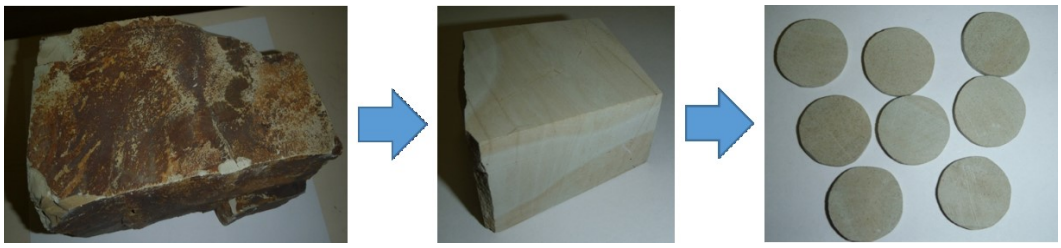

Figure 4-2 Steps of membrane disk preparation

4.2.3 Membrane Reactor Configuration

The packed-bed membrane reactor configuration is shown in Figure 4-3. The outer tube was made of quartz (ID 22 mm) and used as the feed side of the membrane reactor. The permeate side consisted of two concentric ceramic tubes. The sweep gas flowed through the inner tube and the permeate flux flowed out through the outer tube (OD 12.6 mm). The catalyst pellets were packed in the feed side in contact with the membrane and held by the quartz wool. The membrane was sealed on the end of the ceramic outer tube with high temperature ceramic adhesive (REFRACTOBOND ALP, Accumet Materials Co., USA) by the curing procedures described in the next section. All tube connections were sealed with rubber O-rings and Swagelok fittings. Outlet flows of both feed side and permeate side were measured with a bubble meter.

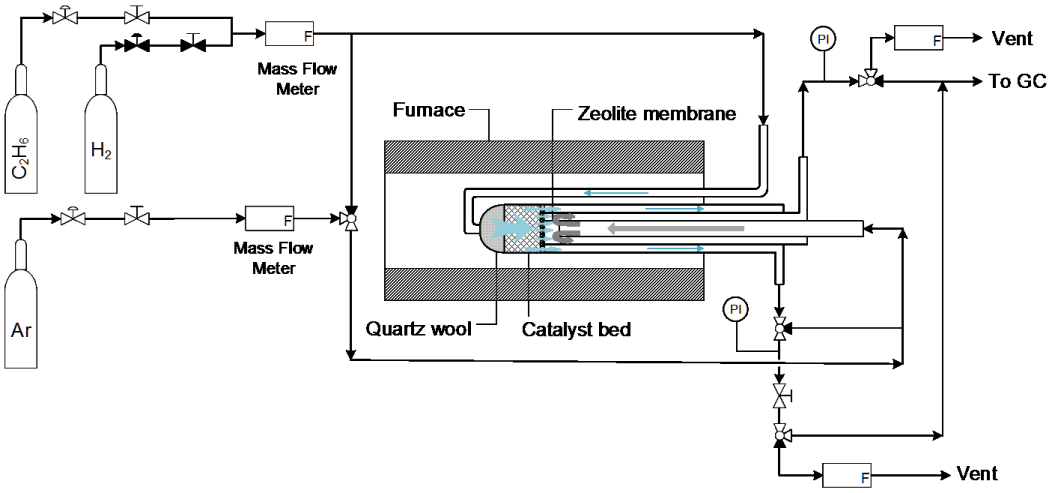

Figure 4-3 Packed-bed membrane reactor configuration

4.2.4 Experiment Conditions

Ethane dehydrogenation reactions were carried out at 500 °C and 550 °C. The amount of catalyst loaded was 2.2 g at both temperatures. An on-line GC (Bruker 450-GC) with automatic sampling valves and TCD detector was used to analyze both the permeate and the feed side streams. Inlet flow rates (feed and sweep gas) were controlled by mass flow controllers (Sierra Instruments Inc.). All gas flow rates (both inlets and outlets) were measured under lab conditions (21 °C, atmosphere pressure). Inlet flow rates were controlled by mass flow meters. Outlet flow rates were measured with bubble meters. All gases used were from Praxair Canada.

Ethane (99.5%) flow rate was 12.0 ml/min. Argon (99.99%) was used as the sweep gas and its flow rate was 54.0 ml/min. A higher sweep gas flow rate did not improve the hydrogen removal from the feed side. Feed side pressure was maintained at 2.7 kPa(g) with a back pressure regulator valve while the permeate side pressure was atmospheric. Argon was not detected in the retentate stream when pure helium was used as a feed stream in the membrane reactor at the same operating conditions. Feed dilution effects were negligible in the membrane reactor experiments.

4.2.5 Switching Membrane Reactor Mode to Conventional Reactor Mode

To quantify the enhancement of ethane conversion and evaluate the performances of the membrane reactor, the ethane dehydrogenation reaction was switched from packed-bed membrane reactor mode to conventional packed-bed

reactor mode by closing off the inlet and outlet of the sweep gas stream. A schematic demonstration is shown in Figure 4-4. When both inlet and outlet of the permeate side were shut off, the concentration of permeated species eventually equalized in both sides. The membrane reactor set-up essentially performed like a conventional packed-bed reactor. The performances of membrane reactor mode and conventional reactor mode for ethane dehydrogenation can be fairly compared to each other.

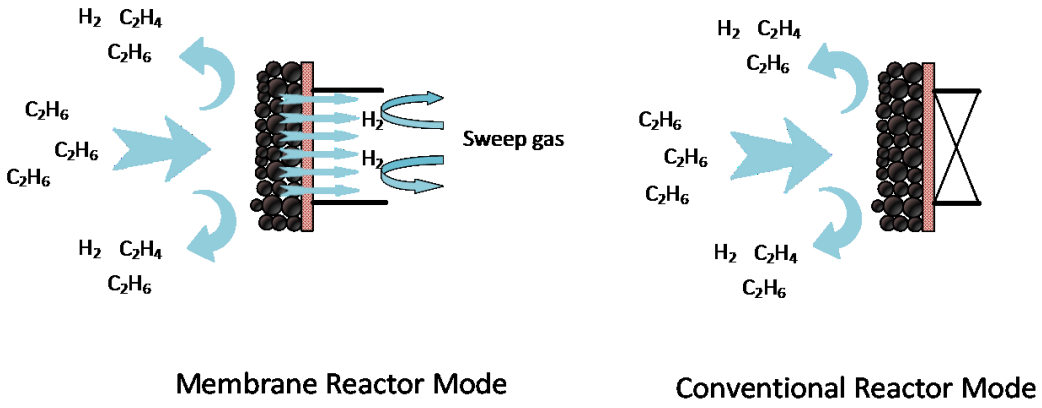

Figure 4-4 Schematic demonstration of switching between membrane reactor and conventional reactor mode

4.2.6 Mass Balance of Species at a Reactor and Membrane Reactor Mode

The reaction rate enhancement achieved in the membrane reactor mode could be quantified considering the mass balance of species in the reaction zone. The integral form of the continuity equation for species *i* in steady-state condition is expressed as:

$$\int_{A_R} \overline{N}_i \cdot \overline{n} dA = W \int_{V_R} r_i^* dV \tag{4-2}$$

where the term on the left-hand side represents the net molar flow rate of species *i* through the boundaries of the reaction zone, r_i^* is the local reaction rate in $mol/(cm^3 \cdot g_{cat} \cdot s)$ and W is the catalyst weight in the reactor. Integrated both sides, the equation (4-2) became:

$$F_{i,out} - F_{i,in} = W\langle r_i^* \rangle_{V_R} \tag{4-3}$$

where F_i is the molar flow rate of each reacting species and $\langle r_i^* \rangle_{V_R}$ is the volume-integrated reaction rate in $mol/(g_{cat} \cdot s)$.

The integral mass balance was applied for each product species of ethane dehydrogenation (H_2 and C_2H_4) in both the conventional reactor and the membrane reactor mode. The combination of each resulting expression gives:

$$\frac{\langle r_i^* \rangle_{V_{R,MR}}}{\langle r_i^* \rangle_{V_{R,R}}} = \frac{\left[Q_{out} x_{i,out}\right]_{MR}}{\left[Q_{out} x_{i,out}\right]_R} + \frac{\left[Q_p x_{i,p}\right]}{\left[Q_{out} x_{i,out}\right]_R} \tag{4-4}$$

Equation (4-4) can also be expressed in terms of dimensionless numbers

$$\tau_{i,MR/R} = \gamma_{i,MR/R} + \beta_{i,P/R} \tag{4-5}$$

Where $\tau_{i,MR/R}$ is the reaction rate ratio of product species between the membrane reactor (MR) and the conventional reactor (R) mode, $\gamma_{i,MR/R}$ is the outlet flow rate ratio for product species between the MR and the R mode, and $\beta_{i,P/R}$ is the ratio between product permeation flow rate over its formation rate in the R mode. The dimensionless number $\tau_{i,MR/R}$ represents the reaction rate enhancement achieved by the system as it switches from R to MR mode. It can be estimated in terms of the flow rate leaving the reaction zone, Q_{out}; the outlet permeate flow rate, Q_p and the outlet compositions from the reaction and permeate zones, $x_{i,out}$ and $x_{i,p}$.

All the dimensionless numbers defined for the analysis of the experimental data are summarized in Table 4-1. They are also related to the Damköhler and membrane Peclet numbers [64] estimated under reaction conditions. The Damköhler number relates the rate of reaction to the rate of reactant feed. The membrane Peclet number is defined in terms of the reactant feed rate and permeation rate of each product.

Table 4-1 Dimensionless numbers defined for the comparison between reactor and membrane reactor mode

Dimensionless number	Symbol	Definition
Reaction rate ratio	$\tau_{i,MR/R}$	$\tau_{i,MR/R} = \frac{\langle r_i^* \rangle_{V_{R,MR}}}{\langle r_i^* \rangle_{V_{R,R}}}$
Outlet flow rate ratio	$\gamma_{i,MR/R}$	$\gamma_{i,MR/R} = \frac{\left[Q_{out} x_{i,out}\right]_{MR}}{\left[Q_{out} x_{i,out}\right]_{R}}$
Permeation/reaction rate ratio	$\beta_{i,P/R}$	$\beta_{i,P/R} = \frac{\left[Q_p x_{i,p}\right]}{\left[Q_{out} x_{i,out}\right]_{R}} = \frac{1}{Da_R Pe}$
H_2/ethane outlet molar ratio	φ_{H_2/C_2}	$\varphi_{H_2/C_2} = \frac{x_{H_2,out}}{x_{C_2,out}}$

$Da_R = \frac{\langle r_i^* \rangle_{R,R} W}{F_{in}}$; $\frac{1}{Pe} = \frac{F_{i,p}}{F_{in}}$

The reaction enhancement can also be evaluated using ethane conversion, ethylene yield and ethylene selectivity. Ethane conversion was calculated in terms of the reaction products. For the reactor mode the ethane conversion is expressed as

$$\alpha_{C_2} = \left(1 - \frac{x_{C_2,out}}{x_{C_2,out} + x_{C_2^=,out} + 0.5 x_{CH_4,out}}\right) \times 100\% \qquad (4\text{-}6)$$

where C_2 and $C_2^=$ represent the ethane and ethylene species respectively. The ethylene yield was expressed as:

$$Y_{C_2^=} = \left(\frac{x_{C_2^=,out}}{x_{C_2,out} + x_{C_2^=,out} + 0.5 x_{CH_4,out}} \right) \times 100\% \quad (4\text{-}7)$$

Ethylene selectivity can be expressed as:

$$S_{C_2^=} = \frac{Y_{C_2^=}}{\alpha_{C_2}} = \left(\frac{x_{C_2^=,out}}{x_{C_2^=,out} + 0.5 x_{CH_4,out}} \right) \times 100\% \quad (4\text{-}8)$$

4.3 Results and Discussions

4.3.1 Reversibility in the Reactor-Membrane Reactor Mode

The system functioned as a membrane reactor (MR) by introducing the sweep gas. When a steady state was reached, it was switched to the reactor mode (R) by shutting off the sweeping gas. Experimental results are shown in Figure 4-5. When the sweep gas was shut off, hydrogen concentration on the feed side increased, and ethylene concentration decreased accordingly. When the system was switched back to MR mode by turning on the sweeping gas, the concentration profiles gradually resumed back to the levels at the beginning of the MR steady state. The experimental data demonstrates the reversibility between the conventional reactor and membrane reactor modes.

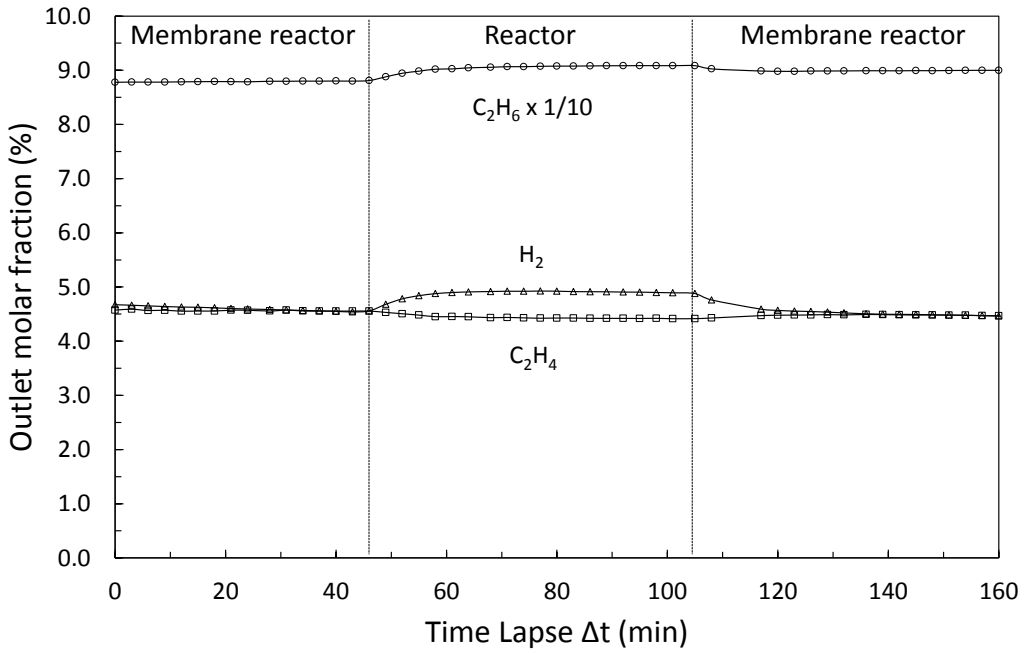

Figure 4-5 Dynamics of molar fractions of H_2, C_2H_4, and C_2H_6 in the reactor outlet as the system switched reversibly between a membrane reactor and a reactor operating mode at 500 °C, WHSV = 0.4 h^{-1}

4.3.2 The Conventional Reactor and Membrane Reactor Modes: Dynamics of Molar Fractions of Reaction Species at the Reactor Outlet

Figure 4-6 shows the steady state concentrations of ethane, hydrogen, and ethylene for both the membrane reactor (MR) and conventional reactor mode (R). When switched from membrane reactor mode to conventional reactor mode, hydrogen concentration increased, ethylene concentration decreased simultaneously, and hydrogen concentration became higher than that of ethylene. Figure 4-7 reveals the concentration changes of hydrogen and ethylene. Hydrogen molar fraction increased from 4.5% to 4.8% when the system was switched from membrane reactor mode to conventional reactor mode. Ethylene molar fraction was

higher in the membrane reactor mode than in conventional reactor mode. The measured data were: $[Q_{out}]_{MR} = 12.6\, ml/min$, $[Q_{out}]_R = 12.9\, ml/min$, permeate rate: 55, permeate compositions: $x_{\mathrm{H}_2,out} = 0.19\ v\%$, $x_{\mathrm{C}_2^=,out} = 0.025\ v\%$, $x_{\mathrm{C}_2,out} = 0.69\ v\%$.

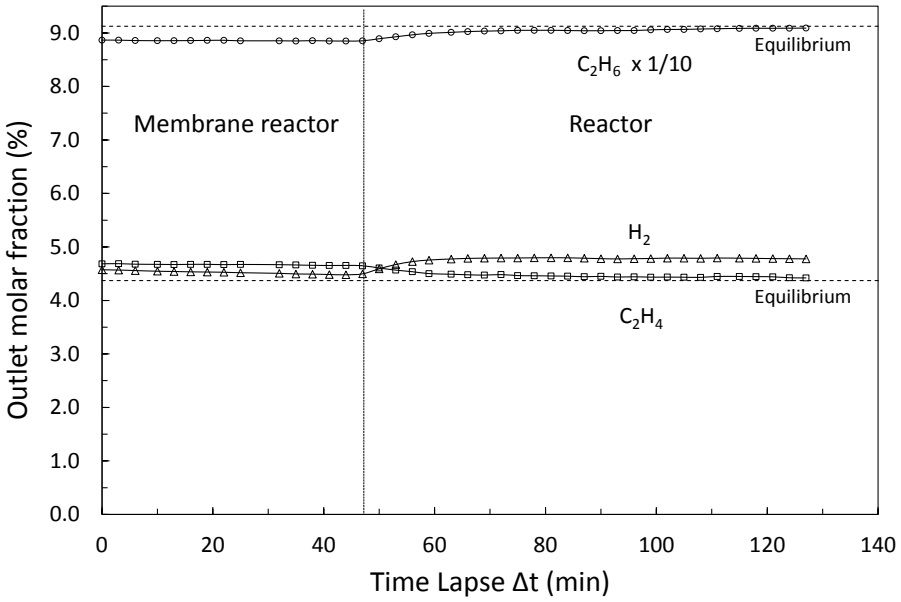

Figure 4-6 Dynamics of outlet molar fractions of C_2H_6, H_2, and C_2H_4 between membrane reactor and reactor mode at 500 °C, WHSV = 0.4 h^{-1}

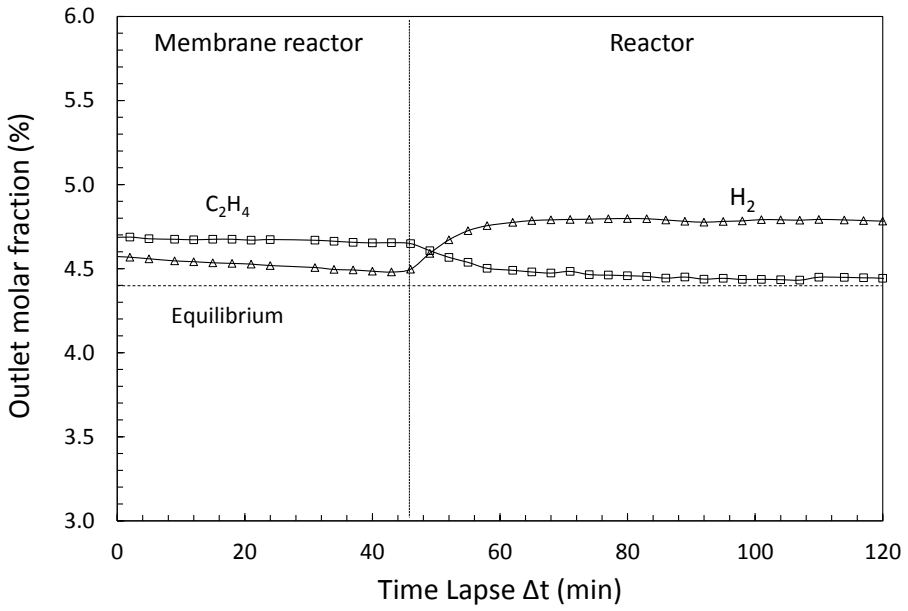

Figure 4-7 Dynamics of outlet molar fractions of H_2 and C_2H_4 between membrane reactor and reactor mode at 500 °C. , WHSV = 0.4 h^{-1}

As shown in Table 4-2, the reaction rate ratio, $\tau_{C_2^=,MR/R}$, calculated with Equation (4-5) in terms of ethylene was 1.05, which indicates that the ethylene production rate in the MR mode was higher than that in the R mode. The ethylene yields ($Y_{C_2^=}$) calculated with Equation (4-7) in the R and MR mode were 4.6% and 4.9% respectively. The results indicate that an ethylene yield enhancement of 6.5% was reached in the MR mode. Ethane conversion increased from 4.9% in the R mode to 5.2% in the MR mode at 500 °C.

The conversion improvement can also be analyzed in terms of the hydrogen permeation rate in relation to its generation rate. The ratio of permeation/reaction rate, $\beta_{H_2,p/R}$, was 16%, which meant that about 16% of the hydrogen generated in the reaction was extracted through the membrane. The value $\beta_{H_2,p/R} =$

16% corresponds to a Damköhler-Peclet number of $Da_R Pe = 6.1$ This number is bigger than the optimal value of membrane reactor effectiveness ($Da_R Pe \sim 1$) [65]. The $\boldsymbol{Da_R Pe}$ number approaching one means all the hydrogen produced in the membrane reactor is extracted through the membrane.

Table 4-2 Experimental values of the dimensionless numbers defined in Table 4-1 for R and MR modes at 500 °C and 550 °C

Mode	R	MR	R	MR	R	MR
T, ℃	500	500	500	500	550	550
$A/V_R, m^{-1}$	0.04	0.04	0.16	0.16	0.04	0.04
$\beta_{H_2,p/R}, \%$	-	16.7	-	36.6	-	24.2
$\varphi_{H_2/C_2}, \%$	5.3	5.1	5.8	4.6	11.2	9.9
$\beta_{C_2^=,p/R}, \%$	-	2.4	-	9.4	-	8.7
$\tau_{C_2^=,MR/R}$	-	1.05	-	1.15	-	1.09
$\alpha_{C_2}, \%$	4.9	5.2	4.8	5.5	9.7	10.5
$Y_{C_2^=}, \%$	4.6	4.9	4.5	5.2	9.0	9.8
$S_{C_2^=}, \%$	94.0	94.1	92.4	94.8	92.2	93.7
$S_{CH_4}, \%$	6.0	5.9	7.6	5.2	7.8	6.3

4.3.3 Increasing the Ratio of Permeation Area/Reactor Volume (A/V_R) of the Membrane Reactor

Increasing the effective permeation area of the membrane in a membrane reactor can extract more hydrogen from the reaction system while the hydrogen generation rate in the conventional reactor mode remains the same under the same

reaction temperature. Therefore, the ratio of permeation rate/reaction rate, $\beta_{H_2,p/R}$, increased. The measured data is: $[Q_{out}]_{MR} = 12.1\ ml/min$, $[Q_{out}]_R = 12.5\ ml/min$, permeate rate: 55.8, permeation compositions: $x_{H_2,out} = 0.43\ v\%$, $x_{C_2^=,out} = 0.09\ v\%$, and $x_{C_2,out} = 1.33\ v\%$.

Figure 4-8 shows the feed and product concentration changes in the two operation modes of ethane dehydrogenation. The membrane reactor had a larger membrane area. With the large-area membrane, the hydrogen molar fraction dropped considerably when the system was switched from conventional packed-bed reactor mode to membrane reactor mode. The ethylene molar fraction values increased beyond the thermodynamic equilibrium.

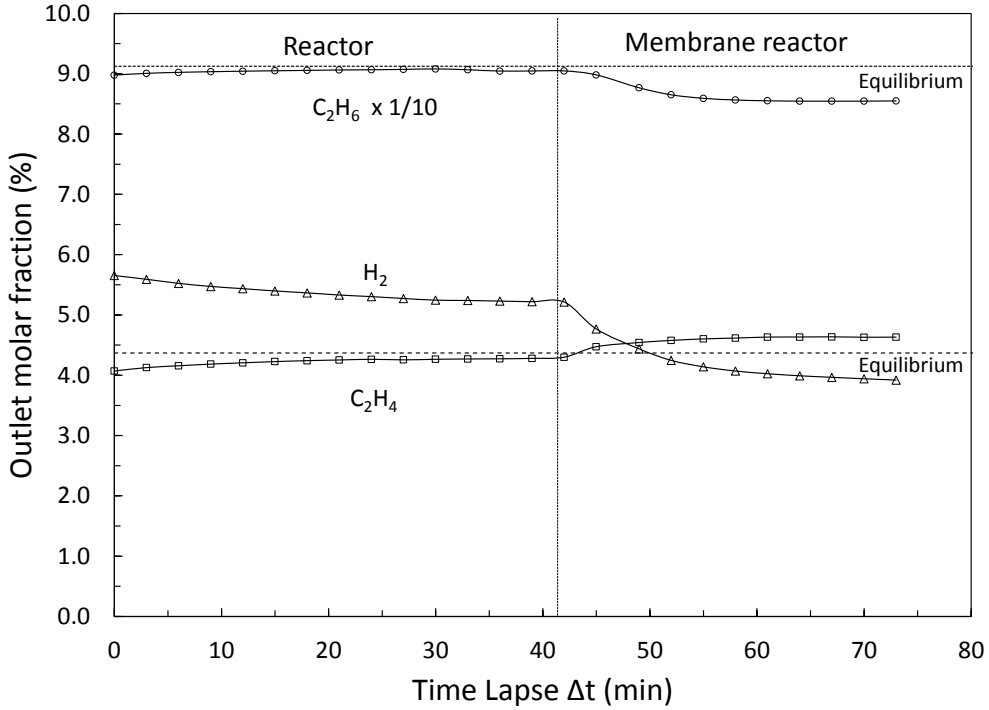

Figure 4-8 Dynamics of outlet molar fractions of C_2H_6, H_2, and C_2H_4 between reactor and membrane reactor mode at 500 °C, WHSV = 0.4 h^{-1} with bigger membrane area ($A/V_R \cong 0.16$)

For the larger ratio of effective membrane area to reactor volume, $A/V_R = 0.16$, the dimensionless number is $\beta_{H_2,p/R} = 36\%$, while for the smaller one ($A/V_R = 0.04$), the dimensionless number is $\beta_{H_2,p/R} = 16\%$, as shown in Table 4-2. Similarly, the H_2/C_2H_6 molar ratio at the reactor outlet φ_{H_2/C_2} decreased 80% of its original value when the system was switched from the conventional packed-bed reactor mode to the membrane reactor mode, while the φ_{H_2/C_2} value only decreased 3.8% (from 5.3% in the conventional reactor mode to 5.1% in the membrane reactor mode) for the lower ratio of $A/V_R = 0.04$. Larger permeation area favored more hydrogen pass through the membrane, and thus more hydrogen

was extracted from the reaction zone. As a result, the reaction rate, $\langle r_i^* \rangle_{V_{R,MR}}$, in the membrane reactor mode increased and the ethane conversion, α_{C_2}, improved in comparison to the membrane reactor with a smaller permeation area. The corresponding value for the dimensionless number is $\tau_{C_2^=,MR/R} = 1.15$, indicating a 15% increase in the reaction rate for a membrane reactor mode. Ethylene yield improved about 17%, from 4.4% in the conventional reactor mode to 5.2% in the membrane reactor mode.

4.3.4 Effect of Reaction Temperatures

Figure 4-9 shows the molar fractions of the products of ethane dehydrogenation in the conventional reactor mode and the membrane reactor mode at 550 °C. The ethylene selectivity at 550 °C decreased compared to that at 500 °C (see Table 4-2) because more side reactions occurred at the higher temperature. The reaction rate ratio, $\tau_{C_2^=,MR/R} = 1.09$, was larger than the corresponding value at 500 °C. The ethane conversion at 550 °C increased from 9.7% in reactor mode to 10.5% in the membrane reactor mode. Other measured data were: $[Q_{out}]_R = 12.4\ ml/min$, $[Q_{out}]_{MR} = 12.2\ ml/min$, Permeate rate: 54.2, permeate composition [%v/v]: $x_{H_2,out} = 0.50\ v\%$, $x_{C_2^=,out} = 0.16\ v\%$, and $x_{C_2,out} = 0.60\ v\%$.

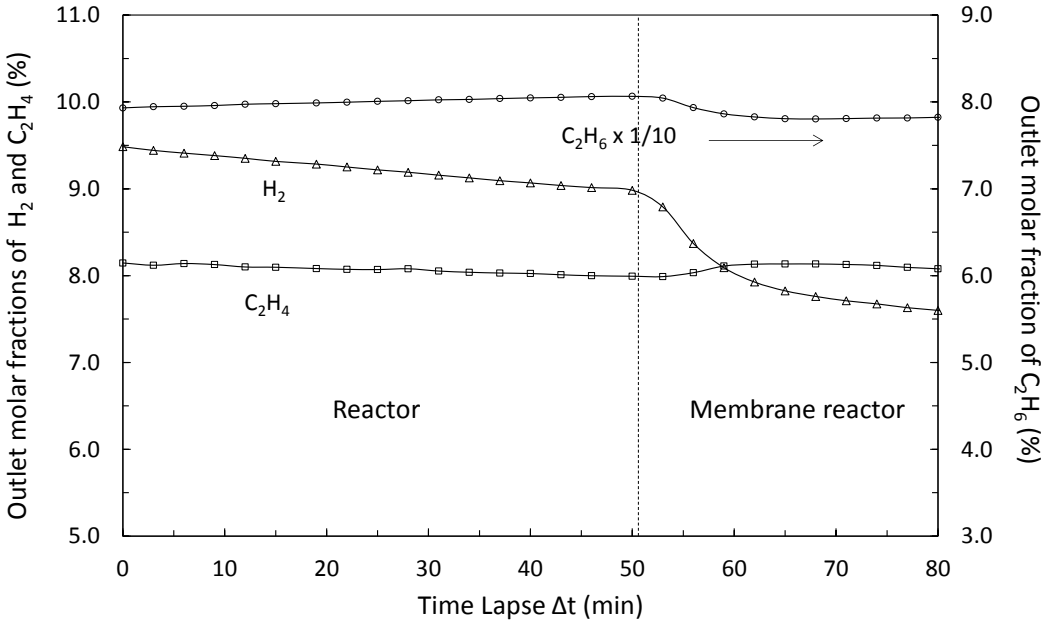

Figure 4-9 Dynamics of outlet molar fractions of C_2H_6, H_2, and C_2H_4 between reactor and membrane reactor mode at 550 °C, WHSV = 0.4 h^{-1}

Higher reaction temperature led to higher product concentraion, and thus the driving force for product permeation increased. Hydrogen and ethylene permeate fluxes at 550 °C increased comparing to experimental data at 500 °C. The dimensionless numbers $\beta_{\mathrm{H}_2,p/R} = 24.2\%$, and $\beta_{\mathrm{C}_2^=,p/R} = 8.7\%$ at 550 °C were larger than the corresponding values at 500 °C with the same A/V_R ratio (see Table 4-2). At 500 °C, $\varphi_{\mathrm{H}_2/\mathrm{C}_2}$ ratio dropped about 3.8% of the original value when the system was switched from the conventional ractor mode to the membrane reactor mode, while it dropped about 11.6% of the original value at 550 °C. Product extraction effectiveness and product concentration of the membrane reactor system increased at the higher temperature. Ethylene yield increased by 6.5% of the original value by switching from reactor mode to membrane reactor mode at 500 °C,

while the yield increased 8.9% of the original value at 550 °C. The ethylene selectivity slightly increased in the membrane reactor mode than in the conventional reactor mode at 550 °C.

4.3.5 Membrane Reactor Effectiveness

As shown in Table 4-3, when the temperature increased from 500 °C to 550 °C, the Damköhler number (Da_R) doubled as the reaction rate increased twice with the temperature. The increase of Da_R is also reflected in the conversion values risen from ~5% at 500 °C to ~10% at 550 °C, as shown in Table 4-2. However, the larger formation rate of hydrogen was compensated with a higher hydrogen removal rate. The hydrogen permeation rate was three times larger at 550 °C than at 500 °C. The increase of hydrogen permeation is also reflected in the $1/Pe$ values shown in Table 4-3. Consequently, the Damköhler-Peclet number ($Da_R Pe$) decreased from 6.1 to 4.2. Thus the effectiveness of the membrane reactor increased at higher temperature. The ethylene yield enhancement at 550 °C was 9.4%, which was higher than that at 500 °C. When the membrane area-to-volume ratio A/V_R increased from 0.04 to 0.16, the permeation/reaction rate ratio $\beta_{\mathrm{H}_2,p/R}$ increased up to 36% at 500 °C. This is equivalent to the $Da_R Pe$ number decreasing to 2.7 . The membrane reactor can work more effectively as $Da_R Pe$ number approaches 1. The ethylene yield enhanced about 17% at 500 °C in the membrane reactor mode. Higher hydrogen removal rate verse its formation rate resulted in a larger ethylene yield enhancement. The membrane reactor mode with the smallest $Da_R Pe$ number led to the largest ethylene yield improvement.

Table 4-3 Ethylene yield enhancements achieved with the membrane reactor at two different reaction temperatures and two A/V_R ratios. The corresponding Damköhler-Peclet numbers were calculated with reaction conditions. WHSV = 0.4 h^{-1}

Temperature, °C	500	550	500
$A/V_R, m^{-1}$	0.04	0.04	0.16
$\frac{1}{Pe}, \times 10^2$	0.8	2.4	2.0
$Da_R, \times 10^2$	4.9	10.0	5.4
$Da_R Pe$	6.1	4.2	2.7
$Y_{C_2^=,enhancement}$, %	6.1	9.4	16.5

4.4 Conclusions

A membrane reactor with a natural mordenite membrane disk coupled with a Pt/Al_2O_3 catalyst packed bed was able to selectively extract hydrogen and to shift the equilibrium of ethane dehydrogenation reaction at 500-550 °C. By increasing the area/volume ratio of the membrane reactor module, a 15.6% ethylene yield enhancement was achieved in comparison to that of the conventional packed bed reactor at 500 °C. The effectiveness of the membrane reactor improved since more hydrogen than the amount formed was removed from the system. The membrane reactor showed a higher ethylene yield enhancement at 550 °C than at 500 °C, due to the increase in hydrogen permeation rate. Lower Damköhler-Peclet number favored the higher ethylene yield improvement. The larger membrane disk at 500 °C provided the largest enhancement in ethylene yield.

Part II: Ethane Dehydrogenation Catalyst Development

Chapter 5. Ethane Dehydrogenation Catalyst Development

5.1 Introduction

Ethylene is the most important organic chemical for the petrochemical industry. It is mainly manufactured by steam cracking of hydrocarbon feedstocks, ranging from natural gas to heavy gas oils. The steam cracking technology is a highly energy intensive [15] process with low selectivity (~75% per pass) [66]. Ethylene production from ethane (main component in natural gas or shell gas) is the most economical and efficient process due to the abundant reserves and easy exploitation of natural gas, and the high selectivity as shown in Table 5-1 . However, compared to other feedsotcks, ethane cracking occurs at a much higher reaction temperature. For example, a typical furnace outlet temperature for cracking ethane is approximately 800 °C, while the temperature for cracking naphtha or gas oils is about 675-700 °C.

In order to lower the energy consumption and increase the conversion of ethane dehydrogenation at lower temperatures, the catalytic membrane reactor was developed as a potential technology for commercial ethylene manufacturing. The use of the membrane reactor can improve conversion by removing hydrogen from the reaction system, and thus shifting the equilibrium to the direction favoring the production of ethylene.

Table 5-1 A product yield comparison using different feedstocks [13]

	Ethane	Propane	Butane	Naphtha	AGO
P/E, kg/kg	65	90	0.35	0.55	0.54
Steam dilution, kg/kg	0.3	0.3	0.486	0.45	0.8
Residence time, s	0.3451	0.3337	0.344	0.3572	0.32
Yield, wt%					
H_2	4.05	1.55	1.09	0.92	0.71
CH_4	3.52	23.27	20.29	14.91	10.58
C_2H_2	0.47	0.51	0.42	0.47	0.38
C_2H_4	52.31	37.51	35.81	28.45	25.93
C_2H_6	35.03	2.8	4.16	4.23	2.82
C_3H_4	0.02	0.57	0.93	0.76	0.63
C_3H_6	1.13	14.82	17.24	15.64	14.07
C_3H_8	0.12	9.96	0.35	0.51	0.37
C_4H_4	0.05	0.08	0.1	0.13	0.12
C_4H_6	1.8	2.9	4.08	4.79	5.73
C_4H_8	0.19	1	2.83	4.52	3.61
C_4H_{10}	0.21	0.04	6.07	0.44	0.05
Benzene	0.47	2.12	2.69	7.12	5.44
Toluene	0.07	0.4	0.77	3.1	3.49
Xylenes	0	0.05	0.11	1.16	0.92
Ethylbenzene	0	0.01	0.01	0.62	0.37
Styrene	0.02	0.2	0.24	1.14	1.18
Pyrolysis gasoline	0.32	1.26	1.81	7.96	7.28
Pyrolysis fuel oil	0.16	0.89	0.94	3.09	16.3
E+P+B olefin	53.63	53.33	55.88	48.61	43.61

The ethane dehydrogenation reaction is more endothermic than that of heavier alkanes like butanes, ethylbenzene because methyl C-H bonds are stronger than methylene C-H bonds. It needs much higher reaction temperature to achieve the practical conversions. The use of catalyst can lower activation energy because the catalysts provide an alternative route to steam cracking by decreasing the activation energy of C-H bonds. Moreover, C-H bonds in ethane (423 kJ/mol) are much stronger than C-C bond (347~356 kJ/mol). C-H bonds in ethane are among the strongest single bonds in nature [67]. In order to achieve a high yield of ethylene production, C-H bonds need to be selectively activated while keeping the C-C bond stable. In this way, the side reactions such as coking and methane production are suppressed and high selectivity can be achieved.

Catalytic dehydrogenation of ethane and other light alkanes at elevated temperatures traces back to early 1900s when transition metals such as Co, Ni, Cu, Fe, Ag, Pt, and Pd were used as catalysts. Frey and Huppke [68] carried out the equilibrium dehydrogenation of ethane, propane, and butane from 300 °C to 500 °C on chromic oxide gel catalyst in 1933, and found the catalysts lost activity at higher temperature. Fabian and Robertson [69] examined ethane dehydrogenation in a vacuum on an incandescent Pt filament at temperatures between 1300 K to 1800 K. A mass spectrometry was used to detect free radicals and atoms evaporating from the filament. At very low pressure, the dehydrogenation reaction was a first order reaction. Pt filament lost reactivity quickly and residual oil vapor was observed. They found water and heavy water (D_2O) vapor could reactivate the poisoned filament, but oxygen and hydrogen could not.

Instead of unsupported catalysts, Pt was ussed on a variety of supports as ethane dehydrogenation catalyst. Cusumano et al. [70] revealed that Pt was more highly dispersed on alumina than on silica-alumina. The higher reactivity of Pt/Al_2O_3 catalyst for cyclohexane dehydrogenation was attributed to the greater dispersion of Pt on alumina support. SiO_2 [71-73], SiO_2-Al_2O_3[70], γ-Al_2O_3, α-Al_2O_3, and η-Al_2O_3 [74] were studied as the supports for the dehydrogenation catalysts. TiO_2 [75], carbon [76], hydrotalcite ($Mg(Al)O$) [77-81], monoliths [82, 83], ZrO_2 [84], and carbon nanotubes [85] were also exploited as the supports for the dehydrogenation catalysts.

Since 1960s the bimetallic platinum catalyst systems were developed to improve the performances of reforming catalysts. A second and/or more metal components were used as promoters. For ethane direct catalytic dehydrogenation, Sn is a widely used promoter for the supported Pt catalyst. Bell's group [80, 81, 86, 87] developed Pt-$Sn/Mg(Al)O$ catalysts for ethane, propane, and butane dehydrogenation. The addition of a second or third component improved ethylene selectivity significantly up to 100%. The Pt-Sn bimetallic system also used in ethane oxidative dehydrogenation reactions [88] and propane dehydrogenation [77]. Besides Sn, Fe [89], Rh [90], and Au [91] were also investigated as a second component of Pt dehydrogenation catalysts.

Mechanisms of ethane dehydrogenation on Pt and supported Pt catalysts have been extensively investigated. Loaiza et al. [92] proposed that ethane was adsorbed dissociatively into ethyl, which dehydrogenated into di-σ ethylene (η_2-CH_2CH_2-) followed by a transformation into ethylidyne ($\eta_3\equiv$C-CH_3) and C-C bond scission.

Vincent et al. [66] proposed a mechanism of generating methane by-product and coke deposit. Adlhart and Uggerud [93] used a Fourier transform ion cyclotron resonance mass spectrometer (FTICR) for investigated the dehydrogenation reaction of methane, ethane, and propane on gaseous platinum cluster cations ($Pt_n^+, n = 1 - 21$). Ethane dehydrogenation occurred through 1,1- and 1,2-dihydrogen elimination mechanism. Ju et al. [94] proposed a C-H and C-C bond activation model on a di-platinum cluster. They found the dehydrogenation pathway ($Pt_2C_2H_4 + H_2$) was favorable in thermodynamics, and the deethylenation pathway ($Pt_2H_2 + C_2H_4$) was favorable in kinetics. Both C-H and C-C cleavages were thermodynamically favorable, but C-H scission was kinetically preferred and C-C scission was kinetically hindered. They also concluded that the two C-H bonds from the two carbon atoms synchronously broke on Pt_2 cluster and then ethylene kinetically released. General elemental reaction steps proposed by Loaiza, Vincent, Adlhart and Uggerud, and Ju et al. are consistent with each other.

Yagasaki and Masel [95] found that coke and methane were mainly formed on the $(1 \times 1)Pt(110)$ surface by the decomposition of adsorbed ethylene (π-bonded) at elevated temperatures. The key to supress coke deposits and methane by-product was to prevent the re-adsorption of ethylene onto the Pt surface [80]. Rodriguez and Kuhn [96] investigated chemical and electronic properties of Pt bimetallic surfaces, and concluded that the formation of Pt-Zn bimetallic bond on $Pt(111)$ surfaces caused the density of Pt *5d* electrons to shift to *6s* and *6p*. Zn has the similar electronic perturbations as early transition metals (Group 3, 4 metals) to Pt, but

larger than late transition metals (Group 8-11 metals, by IUPAC definition). The electronic perturbations caused by Zn on Pt weakened the strength of the $\mathrm{Pt}(5d)$-π bonding interactions, which reduce the carbon monoxide chemisorption ability of Pt.

Some general reaction schemes of ethane dehydrogenation on Pt are illustrated in Reactions (5-1) to (5-12). Ethane adsorbed on Pt surface and dissociated hydrogen atom and ethyl group (Reactions (5-1), (5-2), and (5-4)). Hydrogen atom reacted with absorbed ethane to produce hydrogen gas (Reaction (5-3)).

$$\mathrm{C_2H_6 + 2Pt(s) \rightleftharpoons C_2H_6(s_2)} \tag{5-1}$$

$$\mathrm{C_2H_6(s_2) \rightleftharpoons H(s) + CH_2CH_3(s)} \tag{5-2}$$

$$\mathrm{C_2H_6(s_2) + H(s) \rightleftharpoons H_2(s) + CH_2CH_3(s) + Pt(s)} \tag{5-3}$$

Adsorbed ethyl group further dissociated to form di-σ ethylene (Reaction (5-5), then converted to π-bonded ethylene (Reaction (5-6), followed by a kinetic desorption step (Reaction (5-7)).

$$C_2H_6 + 2Pt(s) \rightleftharpoons H(s) + CH_2CH_3(s) \quad (5\text{-}4)$$

$$CH_2CH_3(s) + 2Pt(s) \rightleftharpoons H(s) + C_2H_4(s_2) \quad (5\text{-}5)$$

$$C_2H_4(s_2) \rightleftharpoons C_2H_4(s) + Pt(s) \quad (5\text{-}6)$$

$$C_2H_4(s) \rightleftharpoons C_2H_4 + Pt(s) \quad (5\text{-}7)$$

The di-σ ethylene transformed to ethylidyne (Reaction (5-8) on $Pt(111)$) and followed a C-C scission to form carbon deposit and methane.

$$C_2H_4(s_2) + 2Pt(s) \rightleftharpoons CCH_3(s_3) + H(s) \quad (5\text{-}8)$$

$$C_2H_4(s) + Pt(s) \rightleftharpoons C_2H_4(s_2) \quad (5\text{-}9)$$

When ethylene re-adsorbed on $(1 \times 1)Pt(110)$ (Reaction (5-9)), it transformed into a strained η_2=CCH_3 group (Reaction (5-10), and followed a disproportionation to yield methane and carbon deposit [95] (Reaction (5-11)).

$$C_2H_4(s_2) + Pt(s) \rightleftharpoons CCH_3(s_2) + H(s) \quad (5\text{-}10)$$

$$CCH_3(s_2) + 2Pt(s) \rightleftharpoons C(s_3) + CH_3(s) \quad (5\text{-}11)$$

$$CH_3(s) + H(s) \rightleftharpoons CH_4 + 2Pt(s) \quad (5\text{-}12)$$

Heterogeneous catalysts are a complex system. Not only the supported active metal components but also the support itself plays a key role in determining the catalyst performances. During the reactions, both the active components and the support interact with reactants. Catalyst performances can be optimized by enhancing the synergetic effects and adjusting the interactions among active components and the supports [97, 98]. This work reports the development and a study of a novel catalyst with high reactivity and selectivity for ethane dehydrogenation: Zn promoted Pt supported on ETS-2.

5.2 Experimental

5.2.1 Catalyst Preparation

A series of Pt-Zn/ETS-2 and Pd-Zn/ETS-2 catalysts were prepared by the incipient wetness impregnation method. ETS-2 is a sodium titanate prepared by alkaline digestion of nano-particles of titania. The caustic digestion converts the surface titania atoms to charged titanate species whose anionic charge is offset by sodium or hydrogen ions. A commercial sample marked “filter cake” was used to prepare the catalysts. The filter cake represents the material directly discharged from the reactor, filtered, and washed without any other pre-treatment steps. The filter cake was calcined at 600 °C for four hours and crushed into 30 to 50 mesh pellets as catalyst support. The ETS-2 support pellets were modified with ZnO and CeO_2 by incipient wetness impregnation method.

Metal precursors were prepared from aqueous solutions: 0.1M H_2PtCl_6 (Hydrogen hexachloroplatinate (IV) hydrate, Pt 40%, Acros Organics), 0.2 M

$Zn(NO_3)_2$ (Zinc nitrate hexahydrate crystalline, Fisher Scientific Canada), 0.1M $(NH_4)_2Ce(NO_3)_6$ (Ammonium cerium(IV) nitrate, 98.5%, Acros Organics), 0.1M $PdCl_2$ (Palladium (II) chloride, Pd 59.5%, Alpha Aesar, USA) (in 28wt% ammonium hydroxide solution, Fisher Scientific Canada).

All ETS-2 supports were calcined at 600 °C for four hours before impregnating metal components. Support ETS-2 was modified by Zn with different contents and then impregnated with 1 wt% of Pt. All catalysts were calcined at 500 °C for four hours except for the specified temperatures (600 and 650 °C). In the same procedure, for the other metal catalysts, the ETS-2 support was impregnated with the solutions mentioned above respectively, dried at room temperature overnight (> 8 hours), and then calcined at 500 °C for four hours. All catalysts mentioned in this work were prepared by the same procedure.

5.2.2 Catalysts Testing in Ethane Dehydrogenation Reaction

To evaluate the catalyst performance in ethane dehydrogenation reaction, a reactor as shown in Figure 5-1 was set up. The reactor was a quartz tube (ID 22 mm). The catalyst bed was supported by quartz wool on both sides. Both reduced and non-reduced catalysts were dried at 110 °C for four hours before use. The catalysts were reduced *in situ* with argon diluted hydrogen (40 v% H_2). The reduction conditions were: diluted hydrogen flow rate 40 ml/min; temperature range from room temperature to 300 °C with the heating rate 2 °C/min; at 300 °C for one hour.

The amount of the catalyst loaded on each run was 3.0 g. An on-line GC (Bruker 450-GC) was used. The ethane feed (99.5%, Praxair) flow rate was controlled by a mass flow meter (Sierra Instruments Inc.). The outlet flow rate was measured by bubble meter under lab conditions.

The selectivity of ethylene was calculated by Equation (5-13).

$$S_{C_2H_4} = \frac{[C_2H_4]}{[C_2H_4]+0.5[CH_4]} \times 100\% \quad (5\text{-}13)$$

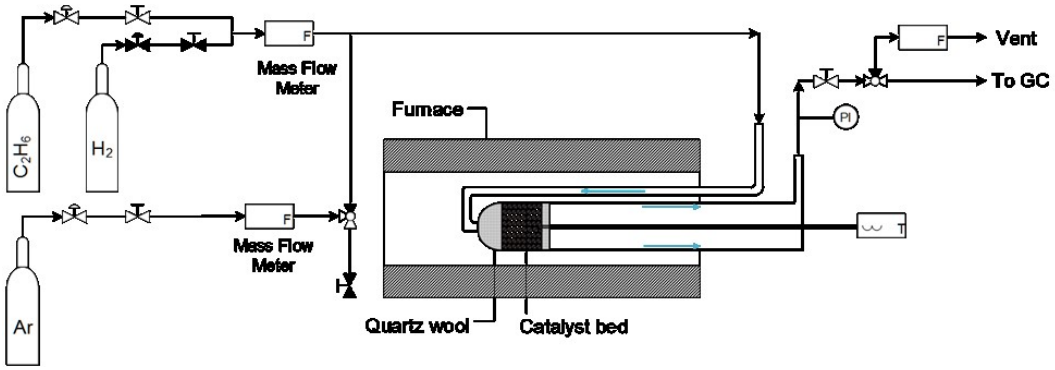

Figure 5-1 The scheme of packed-bed reactor for ethane dehydrogenation

5.3 Results and Discussion

5.3.1 Catalyst Characterization

5.3.1.1 BET and Pt Dispersion

Table 5-2 summarizes the BET specific surface areas of ETS-2, Al_2O_3 supported Pt catalysts, and Pt dispersion on the catalysts. From the table, it can be seen that the commercial ETS-2 filter cake dried at 150 °C has a high surface area.

When the sample was calcined at 600 °C for four hours, the surface area dropped significantly (about 36%). The huge difference of surface areas implies microstructure changes at elevated temperature.

When 1 wt% of Pt was introduced in the ETS-2 support, the specific surface area of 1%Zn/ETS-2 catalyst slightly increased. As the Zn content added into the support increased, the specific surface areas of the catalysts gradually decreased, and leveled off after the Zn content reached 5 wt%. The surface area decrease could be caused by the micropores plugged by ZnO. Solid state reaction occurred at higher temperature, as shown by the XRD results in Figure 5-4.

Table 5-2 BET Surface Area and Pt Dispersion of Catalysts

Catalyst (support)	Specific surface area, (m^2/g)	Pt surface dispersion, %	Pt mean crystal size, nm
ETS-2 (150 °C dried)	189.7	-	-
ETS-2 (600 °C calcined)	68.5	-	-
1%Pt/ETS-2	83.3	2.02	56.0
0.5%Zn, 1%Pt/ETS-2	50.0	8.21	13.8
1%Zn, 1%Pt/ETS-2	51.4	10.75	10.5
2%Zn, 1%Pt/ETS-2	42.4	3.54	32.0
5%Zn, 1%Pt/ETS-2	28.4	5.72	19.8
7.5%Zn, 1%Pt/ETS-2	28.4	3.42	33.0
5%Zn, 1%Pt/ETS-2 (500 °C, spent)	28.7	3.41	33.2
5%Zn, 1%Pt/ETS-2 (600 °C calcined)	24.3	0.97	116.4
5%Zn, 1%Pt/ETS-2 (650 °C, spent)	22.4	0.05	2464.2
0.5%Pt/Al_2O_3 (standard)		21.72	4.40
1%Zn, 1%Pt/Al_2O_3		41.14	2.75

The relationship between Zn content and Pt surface dispersion and particle sizes is illustrated in Figure 5-2. From the figure, it can be seen that the Pt dispersion on the catalysts dramatically increased with Zn content, and reached the maximum at 1wt% of Zn. Further increase in the Zn content led to rapid reduction in Pt dispersion. When Zn content reached 5 wt% any additional Zn could not cause any change in the dispersion, but the dispersion of Pt on the catalyst was still higher than that on the catalyst without Zn. The Pt crystal size change followed the opposite trend. Pt particle size decreased exponentially with the Pt dispersion, as shown in Figure 5-3. The introduction of Zn changed the ETS-2 surface properties, and therefore enhanced the Pt dispersion on the surface and Pt particle size reduction. The higher dispersion of Pt on the surface, the more active sites they can provide, and a higher activity of the catalyst can be achieved.

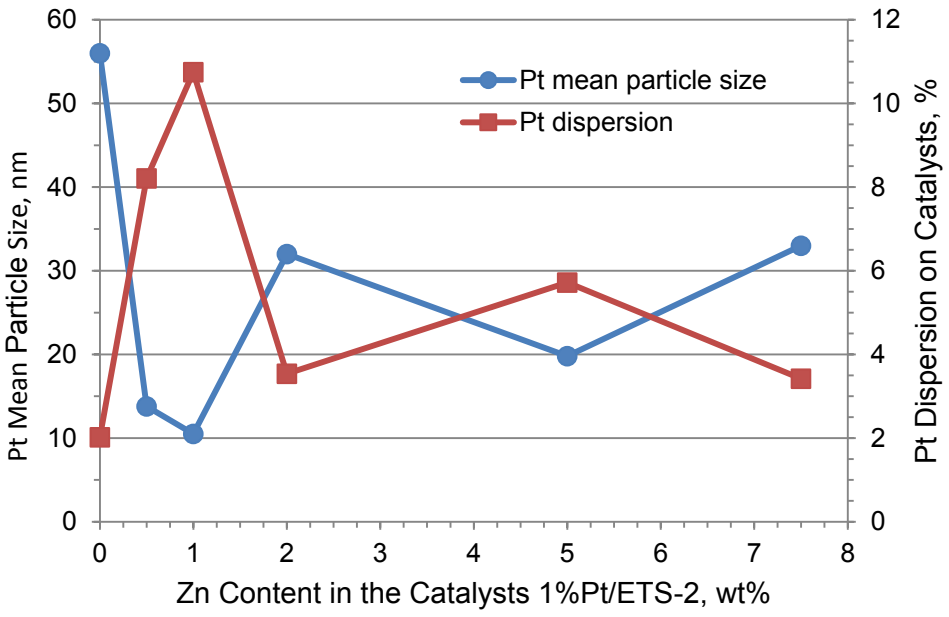

Figure 5-2 Pt mean particle size and dispersion change with Zn content

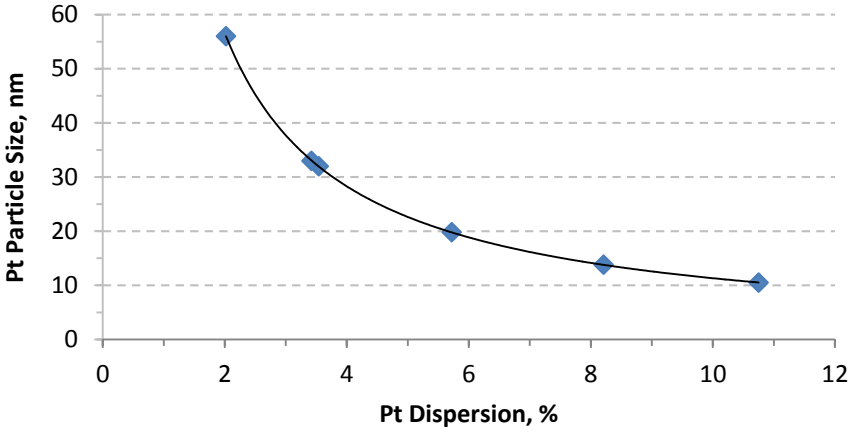

Figure 5-3 Pt particle size change with dispersion on catalysts

For alumina supported Pt catalysts, adding Zn enhanced the Pt dispersion significantly. The dispersion results of Pt on ETS-2 and alumina indicate that Zn could improve Pt dispersing on supports. When the catalysts with 5wt% of Zn calcined and/or tested at 600 °C or higher the Pt dispersion decreased significantly, but the specific surface area dropped slightly.

5.3.1.2 XRD

Figure 5-4 shows the XRD patterns of ETS-2 dried at 150 °C and calcined at 600 °C for four hours. For the dried sample, the TiO_2 was in the form of anatase. After calcined at 600 °C for four hours, some anatase phase was converted into rutile phase. Figure 5-5 indicates the XRD patterns of the catalyst 5%Zn, 1%Pt/ETS-2 treated at different temperatures. From the figure, it can be seen that new characteristic peaks are present in all catalyst's patterns, which imply loaded

metal components reacted with the support at elevated temperatures. It is unclear whether those reactions will affect catalyst performance until further experiments are conducted.

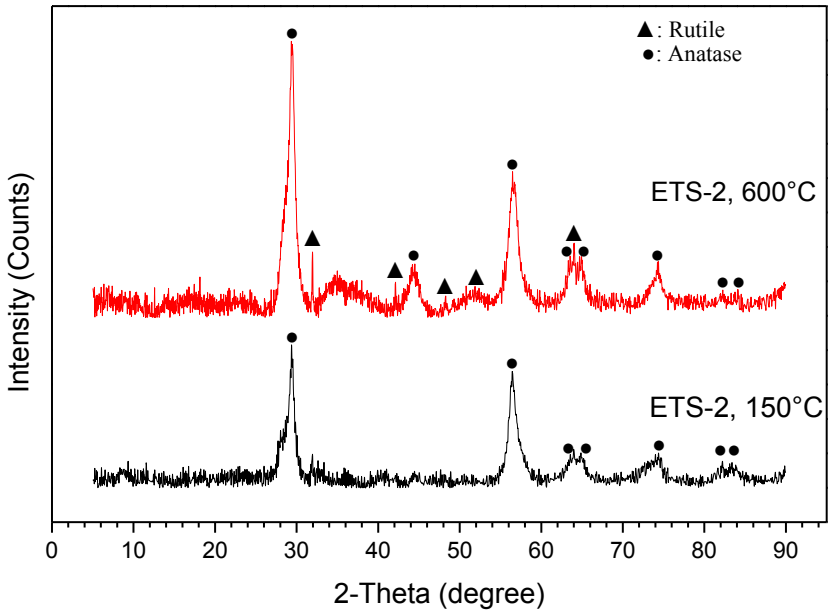

Figure 5-4 XRD patterns of ETS-2 dried at 150 °C and calcined at 600 °C for four hours

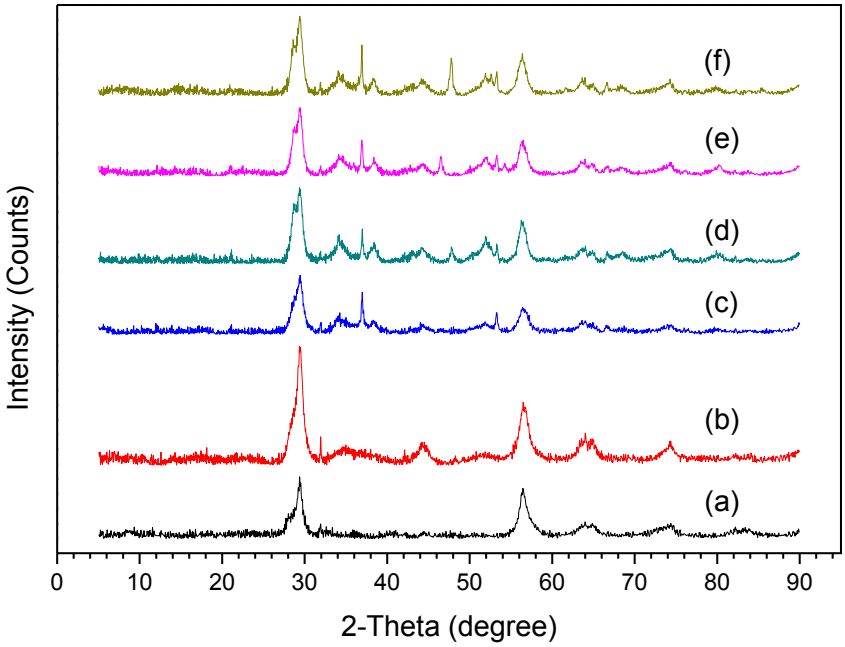

Figure 5-5 XRD patterns of: (a) ETS-2 dried at 150 °C , (b) ETS-2 treated at 600 °C, (c) 5%Zn, 1%Pt/ETS-2 (500 °C calcined), (d) 5%Zn, 1%Pt/ETS-2 (500 °C tested), (e) 5%Zn, 1%Pt/ETS-2 (600 °C calcined), (f) 5%Zn, 1%Pt/ETS-2 (600 °C tested)

5.3.1.3 Microstructure and Morphology of the Catalysts

Figure 5-6 shows the SEM images of ETS-2 before calcination (a) and after calcination at 600 °C (b). From the two images, it can be seen that the texture of ETS-2 with and without calcination is made of 1-2 μm of irregular fine particles. Low temperature dried samples are present as more flaky grains. After calcination at the elevated temperature the particle of the sample became granular. The change of morphology may count for the change of the specific surface area.

Figure 5-7 shows the images of the catalyst 5%Zn, 1%Pt/ETS-2 (a) calcined and (b) tested at 500 °C. There are no visible aggregated Pt particles observed in

either image. Figure 5-8 shows the images of the catalyst with the same compositions but treated at 600 °C. After testing, aggregated Pt particles were present, which was confirmed by the EDX analysis.

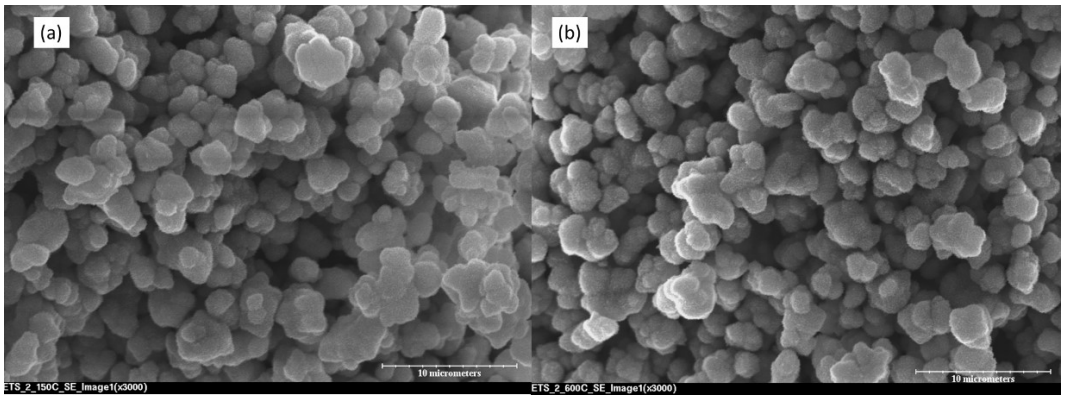

Figure 5-6 Industrial ETS-2 (a) dried at 150° for 4 hours; (b) calcined at 600 °C for 4 hours

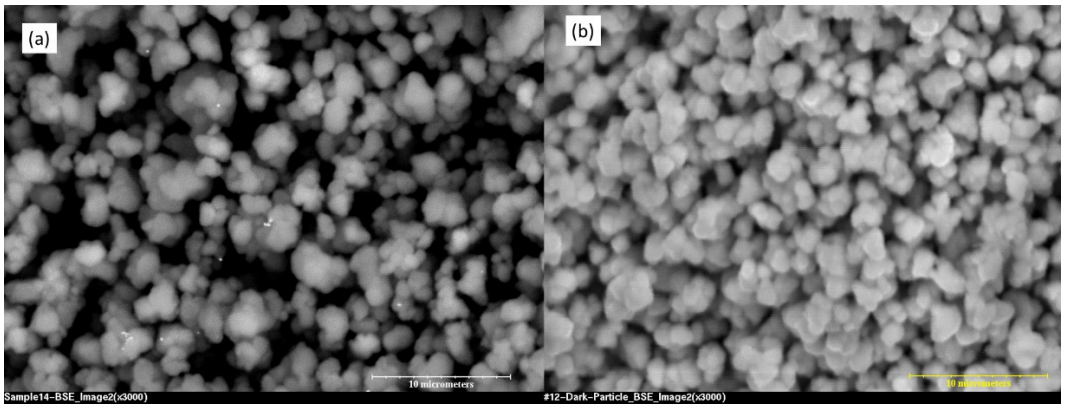

Figure 5-7 Catalyst 5%Zn, 1%Pt/ETS-2 (a) calcined at 500 °C for 4 hours; (b) tested at 500 °C

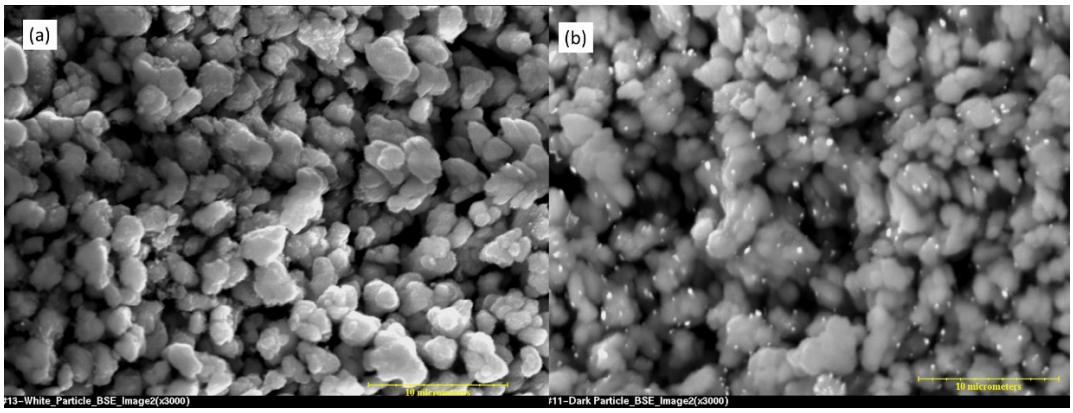

Figure 5-8 Catalyst 5%Zn, 1%Pt/ETS-2 (a) calcined at 600 °C for 4 hours; (b) tested at 650 °C

Figure 5-9 shows the image of catalyst 1%Pt/ETS-2 calcined at 500 °C. In the figure, aggregated Pt particles can be identified. Aggregation of active metal component will cause activity loss and changes in both stability and selectivity.

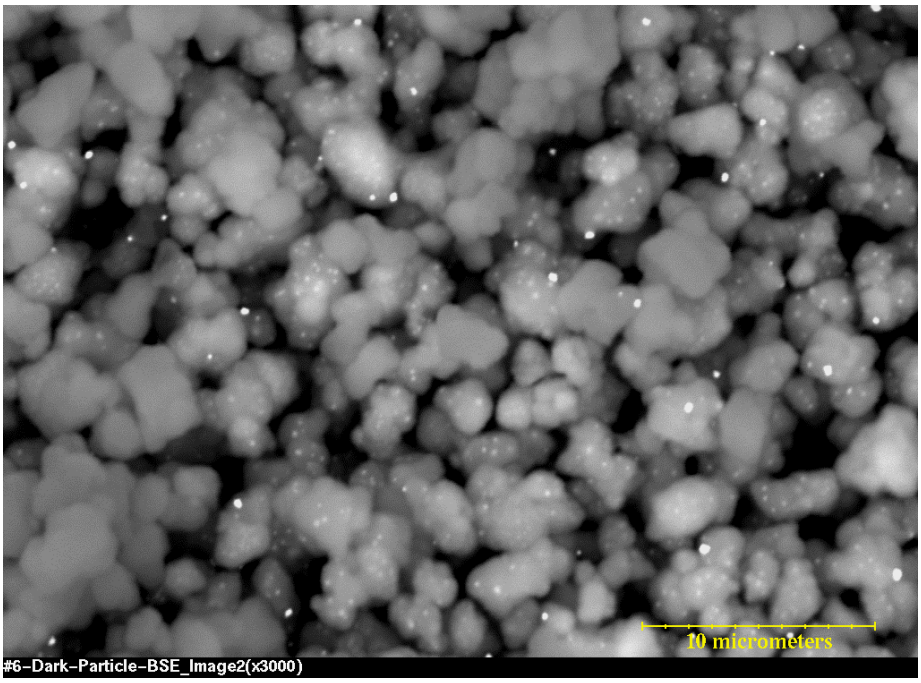

Figure 5-9 Catalyst 1%Pt/ETS-2 calcined at 500 °C for 4 hours

Figure 5-10 shows TEM images of catalyst 1%Pt, 5%Zn/ETS-2 treated at different conditions. From Figure 5-10 (a), it can be seen that Pt particles have aggregated on the catalyst surface. After the catalyst was evaluated for ethane dehydrogenation at 500 °C for four hours, Pt particles grew larger (b). When the catalyst calcined at 600 °C, the aggregated Pt particle size were larger than at 500 °C.

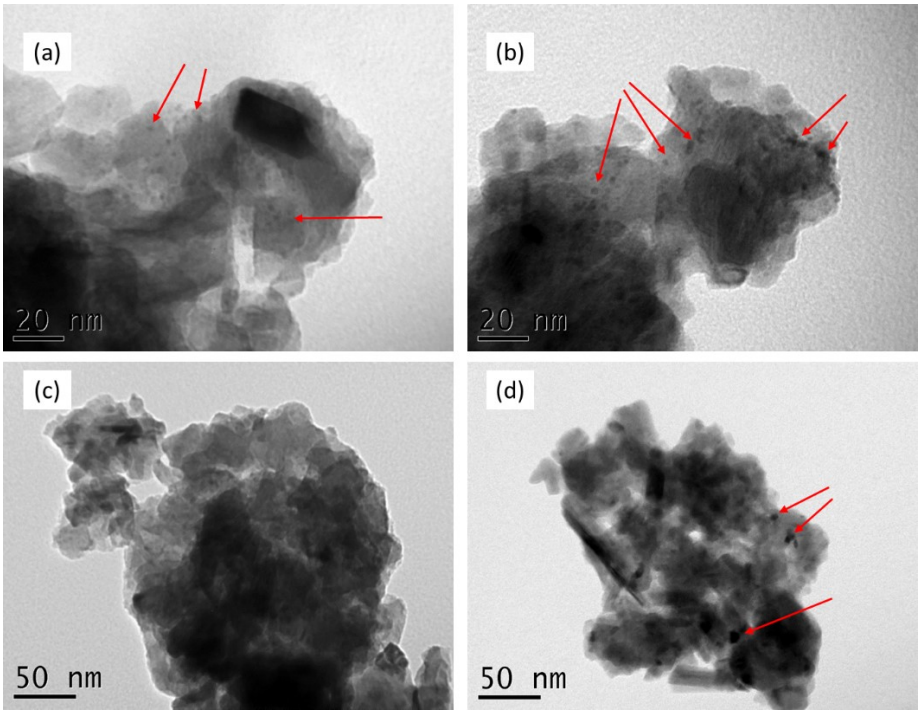

Figure 5-10 TEM images of the catalyst 1%Pt, 5%Zn/ETS-2: (a) calcined at 500 °C, (b) spent (run at 500 °C), (c) calcined at 600 °C, (d) spent (run at 600 °C)

5.3.1.4 XPS

The catalyst 5%Zn, 1%Pt/ETS-2 was calcined at 500 °C and 600 °C for four hours respectively, followed by hydrogenation reduction under the conditions: 40 v% H_2, 40ml/min, and 300 °C. Figure 5-11 shows XPS spectrum of the catalyst

calcined at 600 °C before reduction. The deconvolutions of the spectrum for core level Zn $2p_{3/2}$ revealed that the binding energies of Zn $2p_{3/2}$ could be deconvoluted to 1022.5 eV and 1021.1 eV. The Zn precursor was $Zn(NO_3)_2$. When calcined at elevated temperature, it was decomposed to ZnO. The binding energy 1022.5 eV is associated to Zn species in ZnO, which showed good agreement with literature data [99, 100]. The binding energy 1021.1 eV corresponds to metallic Zn [99-101] generated from the reduced ZnO. Large negative shift of the binding energy implied the formation of Pt-Zn alloy [96]. By integrating the two peak areas, it can be calculated that 81% of ZnO was reduced to metallic Zn.

XPS spectrum of the catalyst calcined at 500 °C before reduction was different from that of the catalyst treated at 600 °C, as shown in Figure 5-12. Only one single peak at 1021.3 eV was observed, which was ascribed to metallic Zn. Based on the negative binding energy shift, it was predicted that probably Pt-Zn alloy was formed.

Thermodynamic calculations indicate that Zn^{2+} cannot be reduced by hydrogen due to the positive free Gibbs energy under the present conditions. However, the free Gibbs energy becomes negative if hydrogen atoms take part in the reduction. The reduction of Zn^{2+} can be explained as follows: Pt cations were reduced first by hydrogen during the reduction process, and then, the reduced metallic Pt acted as the active sites to dissociate hydrogen. Afterwards, hydrogen atoms spilled over from Pt [102-106] to the adjacent zinc cations and reduced them to their metallic state. Furthermore, when Pt and Zn formed an alloy, the enthalpy of alloy formation was negative. The reduction of zinc cation was thermodynamically

favorable. The similar binding energy of metallic Zn and Zn^{2+} made it difficult to assess the zinc state by XPS. The Zn LMM Auger transition analysis is more distinguishable [100].

The differences of reducibility of ZnO in the catalysts treated under different temperatures indicate that ZnO reacted with support at higher temperature (600 °C) and formed a new species phase, which is harder to be reduced.

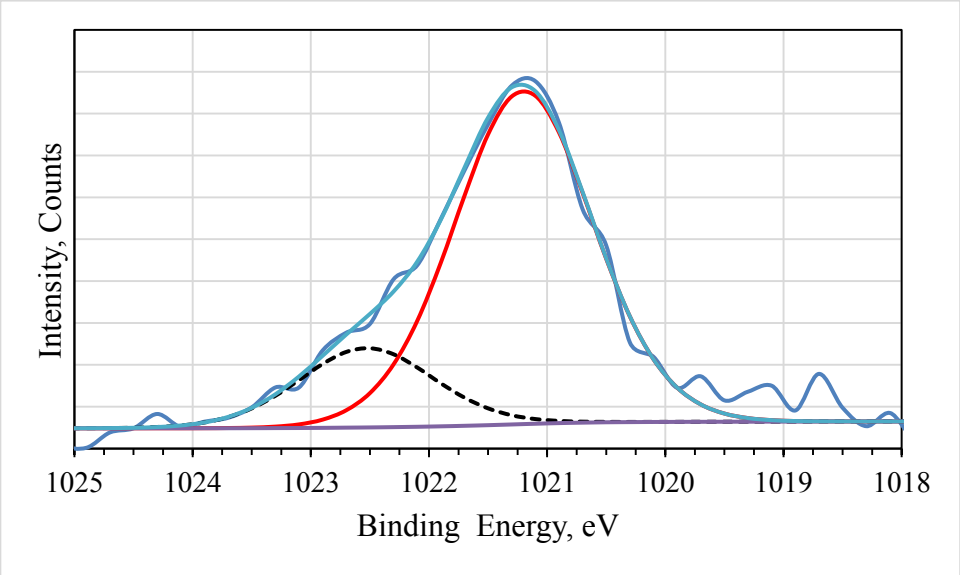

Figure 5-11 XPS of the Zn $2p_{3/2}$ of catalyst 5%Zn, 1%Pt/ETS-2 calcined at 600 °C

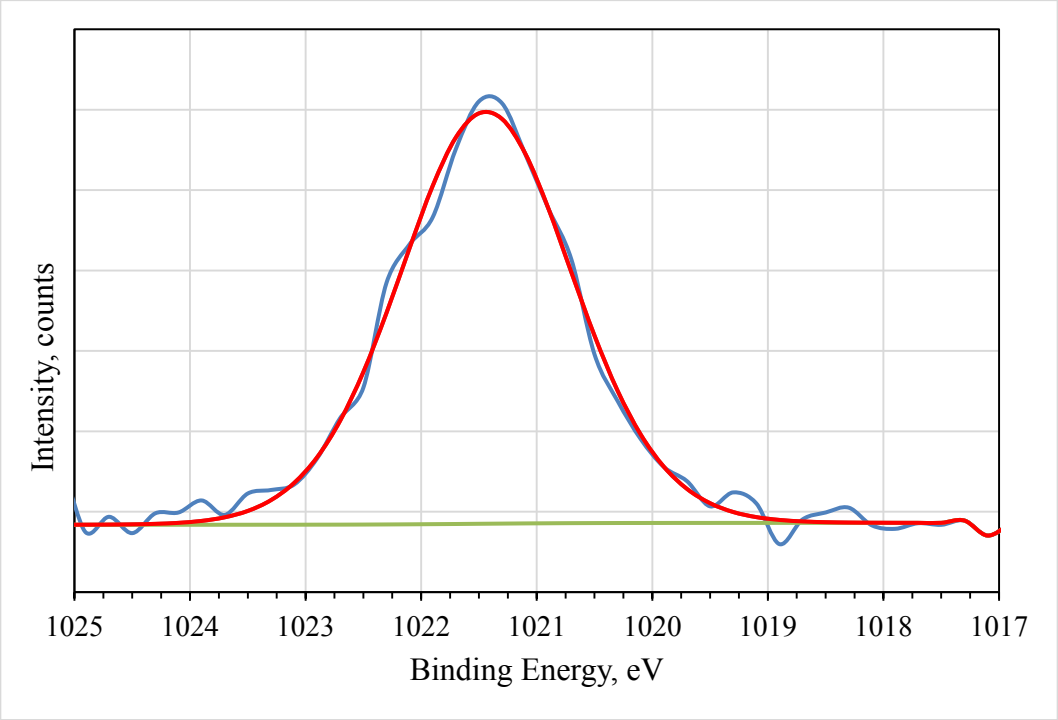

Figure 5-12 XPS of the Zn $2p_{3/2}$ of catalyst 5%Zn, 1%Pt/ETS-2 calcined at 500 °C

5.3.1.5 TPR

Figure 5-13 illustrates the H_2-TPR profiles of the three catalysts: (1) no Zn modified, only Pt loaded 1%Pt/ETS-2; (2) no Pt, only Zn modified 5%Zn/ETS-2; and (3) Zn modified and Pt loaded 1%Pt, 5%Zn/ETS-2.

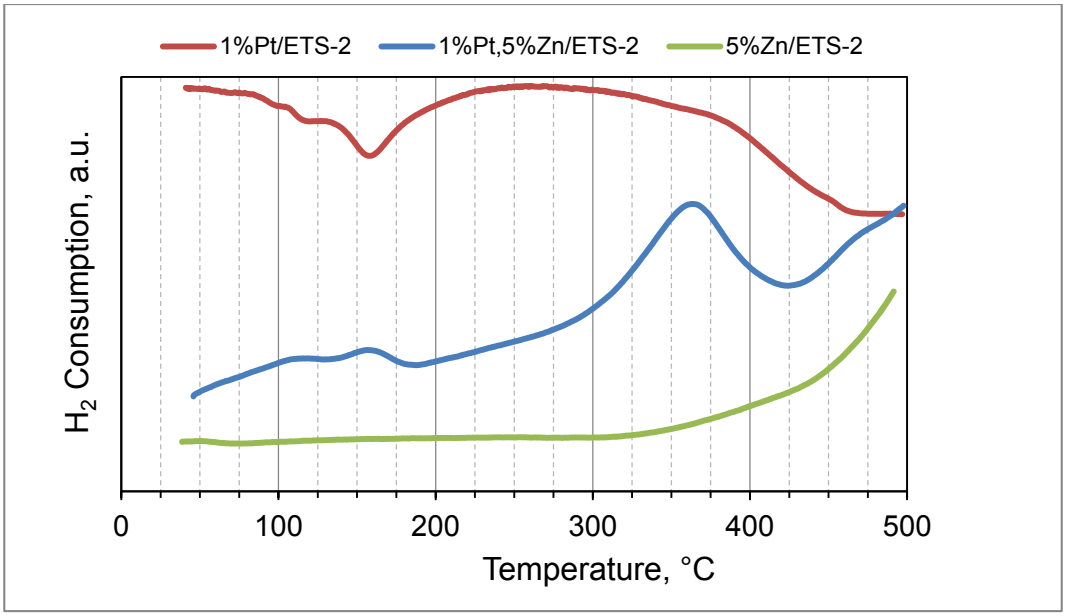

Figure 5-13 H_2-TPR profiles of ETS-2 supported catalysts

TPR curves reflected the difference in the reduction ability of the catalysts modified with different metals. The Pt metal on the catalyst 1%Pt/ETS-2 was much easier to be reduced. The Pt started to be reduced at room temperature. The hydrogen uptake gradually decreased. Starting from 130 °C for 5%Zn/ETS-2, the Zn was not reduced until 330 °C. A gradual increased curve after 330 °C revealed that increasing amounts of Zn were reduced at relatively high temperatures. For the Pt catalyst with Zn modification, 1%Pt, 5%Zn/ETS-2, the reduction of Zn changed their reduction behaviors. Two reduction peaks (H_2 consumption) appeared at low temperatures (110 °C and 160 °C), and one peak at 360 °C.

5.3.1.6 TG-MS Analysis of Coke on Spent Catalysts

The TG-MS analysis of the spent 5%Zn, 1%Pt/ETS-2 catalyst is shown in Figure 5-14. In the temperature range from room temperature to 600 °C, the total weight loss was only 1.4 wt%. The MS analysis proved that all the weight loss was associated with the water that was due to the desorption of the physically adsorbed water and –OH decomposition. No carbon deposited on 5%Zn, 1%Pt/ETS-2 after reactions was identified. However, a carbon dioxide emission peak around 400 °C in the TG-MS analysis of the spent alumina supported catalyst was identified, as shown in Figure 5-15. Carbon dioxide emission indicated there was coke deposit on the spent catalyst. The amount of water loss of the alumina supported catalyst was also higher than that of the ETS-2 supported catalyst.

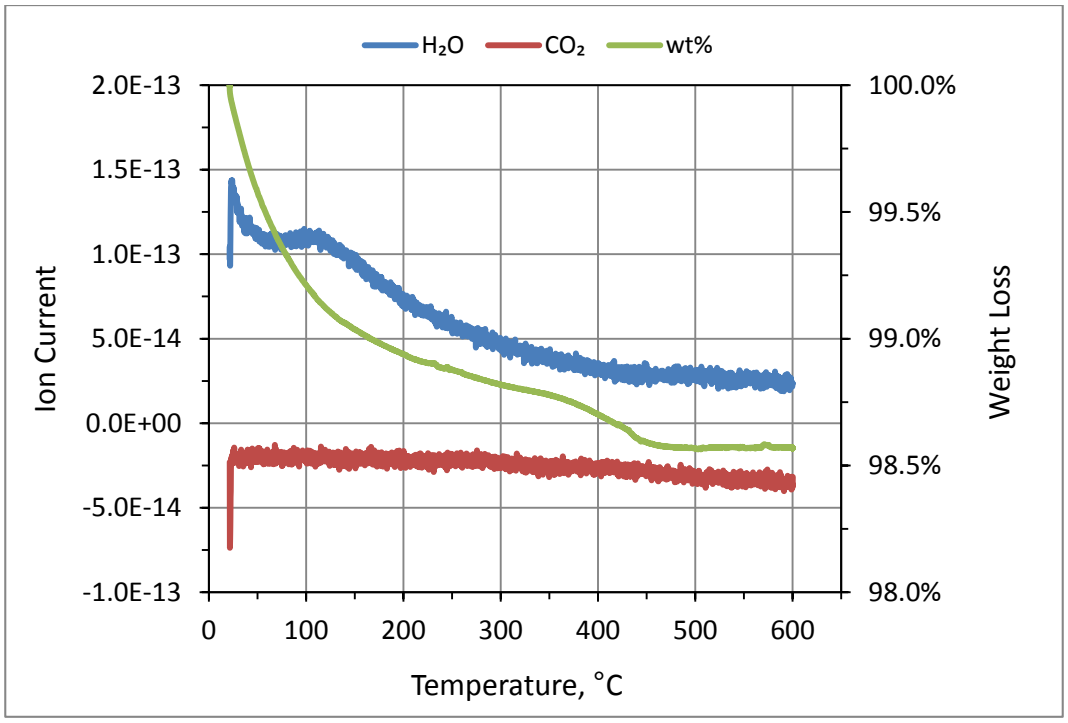

Figure 5-14 TG-MS analysis of catalyst 5%Zn, 1%Pt/ETS-2 tested at 650 °C

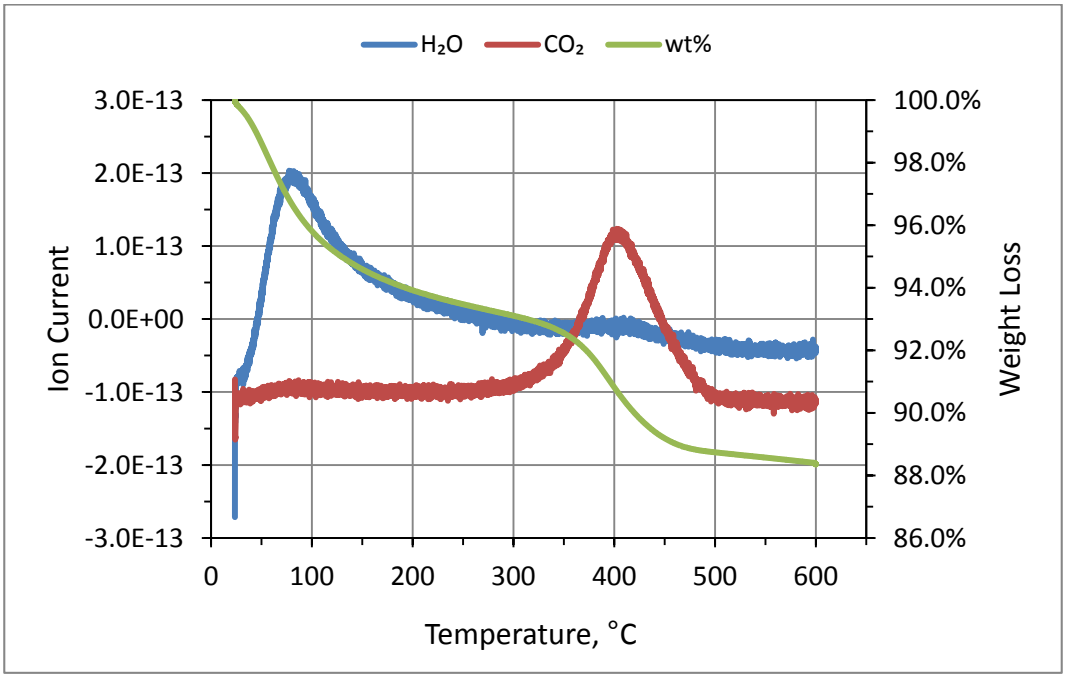

Figure 5-15 TG-MS analysis of catalyst 1%Zn, 1%Pt/Al_2O_3 tested at 500 °C

5.3.2 Effect of Main Metals on the Activity and Selectivity of Ethane Dehydrogenation

The noble metals, Pt and Pd, are the main catalytic components in ethane dehydrogenation reactions. To study the Pt and Pd effect on catalyst performances, the same amount of platinum and palladium were loaded on ETS-2 support respectively as the catalysts for ethane dehydrogenation. Figure 5-16 shows the ethane dehydrogenation product distributions on the two catalysts. From the figure, it can be seen that the Pt/ETS-2 catalyst exhibited a higher ethylene and lower hydrogen and methane yields at steady state. About 0.5 wt% of by-product methane

was produced on both catalysts. Pt was a better active component for ethylene production compared to Pd.

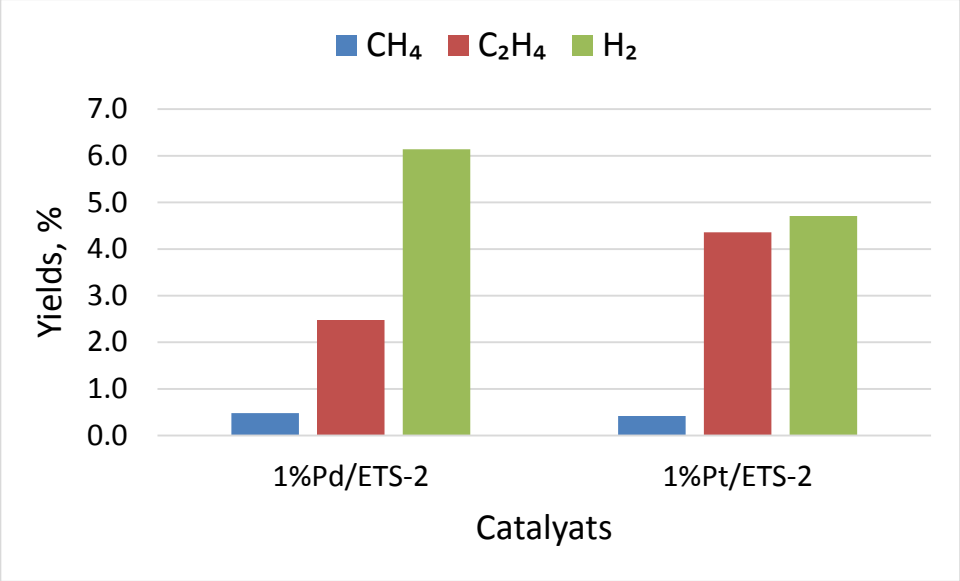

Figure 5-16 Product spectrum obtained with the 1%Pd/ETS-2 and 1%Pt/ETS-2 catalysts at 509 °C, and ethane WHSV = 0.28h^{-1}

Figure 5-17 shows the yield changes using 1%Pt/ETS-2 as the catalyst at different space velocities. The product distribution of 1%Pd/ETS-2 at WHSV=0.27 h^{-1} is also shown in the figure. The product yields on 1%Pt/ETS-2 decreased with the space velocity increasing. Even at higher space velocity (WHSV=0.80 h^{-1}), the ethylene yield of 1%Pt/ETS-2 was still higher than that of 1%Pd/ETS-2 at the lower space velocity (WHSV=0.27 h^{-1}). The result further proved that the Pt catalyst had higher activity and ethylene selectivity than that of the Pd catalyst.

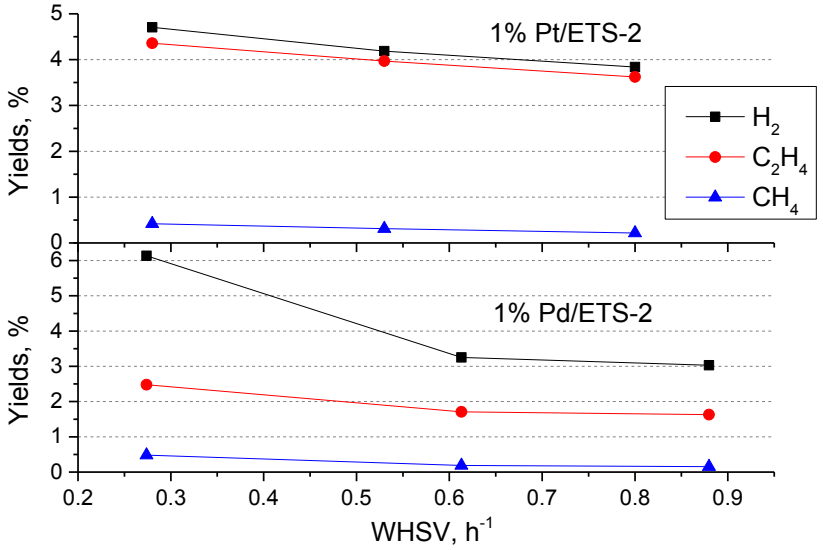

Figure 5-17 Product yield change with space velocity at 509 °C over catalysts 1%Pd/ETS-2 and 1%Pt/ETS-2

5.3.3 Effect of the Supports on the Activity and Selectivity of Ethane Dehydrogenation

To study the effect of the supports on the reaction performances of the ethane dehydrogenation catalysts, three catalysts were prepared with three different supports, ETS-2, Al_2O_3, and natural zeolite clinoptilolite (impregnated with 1 wt% Pt). The product distributions of the three catalysts in ethane dehydrogenation reaction under the same conditions are illustrated in Figure 5-18. Catalyst 1%Pt/ETS-2 gave the lowest yield of by-product methane, but the highest yield of ethylene. Catalyst 1%Pt/Al_2O_3 generated the highest methane. Catalyst 1%Pt/clinoptilolite had the highest hydrogen yield and the lowest ethylene yield.

Obviously, ETS-2 was the best support used on the catalyst for ethane dehydrogenation.

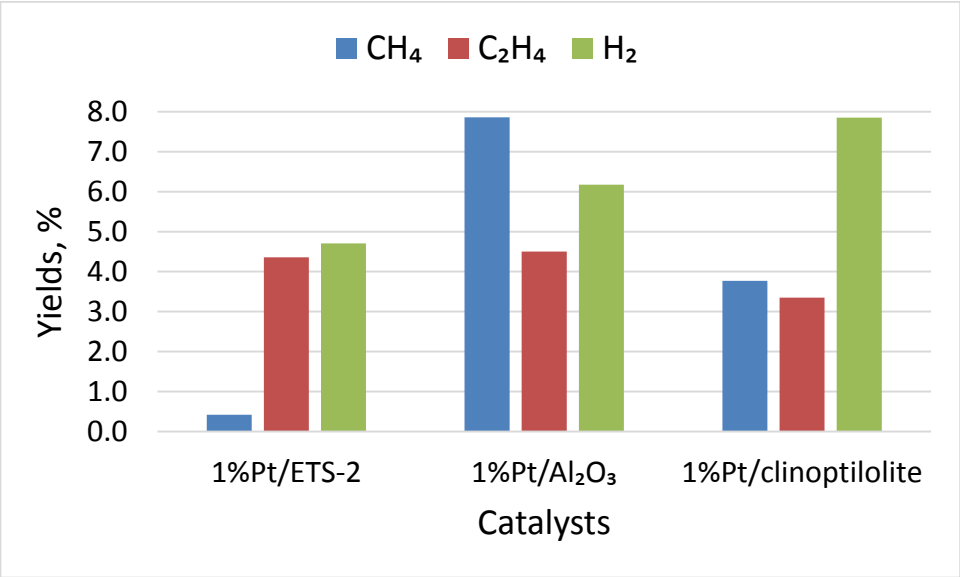

Figure 5-18 Product spectrum obtained with the 1%Pt/ETS-2, 1%Pt/Al_2O_3, and 1%Pt/clinoptilolite catalysts at 509 °C, and ethane WHSV = 0.28 h^{-1}

5.3.4 Effect of Promoters on the Activity, Selectivity and Stability of Ethane Dehydrogenation

5.3.4.1 Zn as the promoter

The 1%Pt/Al_2O_3 was modified with 1 wt% of Zn, and a comparison is illustrated in Figure 5-19. It is noted that Zn improved the ethylene concentration, and simultaneously suppressed the production of methane generated from the side reactions. As space velocity increased, the methane yield decreased significantly. Hydrogen yield decreased slightly, while ethylene yield increased slightly. The

results in Figure 5-19 suggest Zn is an effective promoter for ethane dehydrogenation reaction.

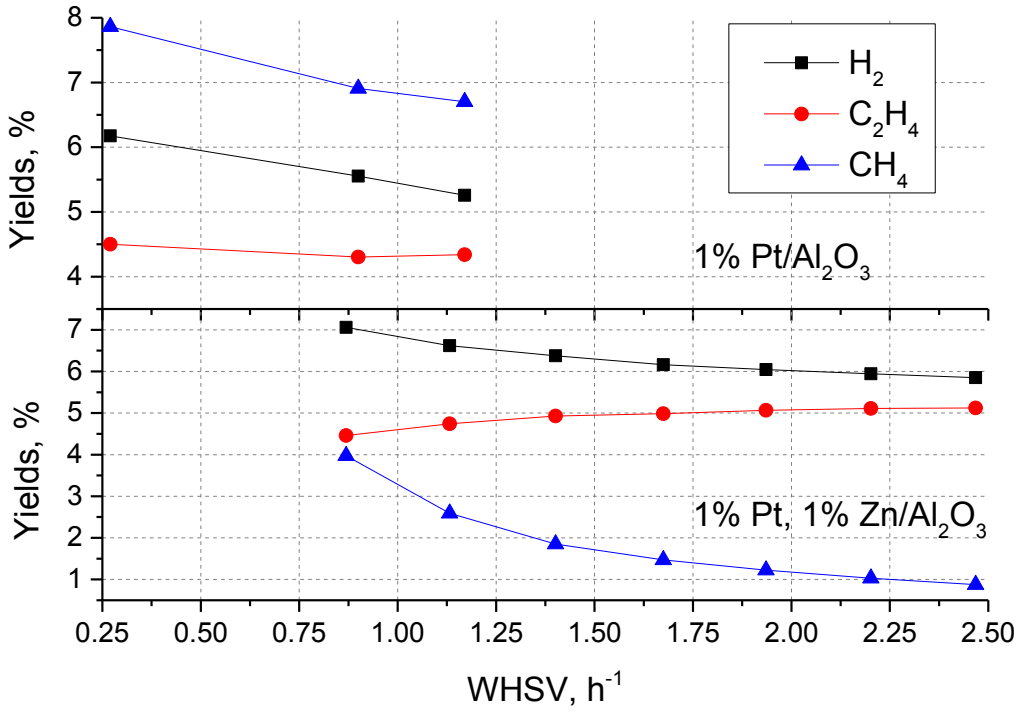

Figure 5-19 Product concentration change with WHSV at 509 °C over catalysts 1%Pt/Al_2O_3 and 1%Pt, 1%Zn/Al_2O_3

The product yield changes with time on 1%Pt/ETS-2 and 0.5%Zn, 1%Pt/ETS-2 are shown in Figure 5-20 and Figure 5-21 respectively. The conversion on 1%Pt/ETS-2 catalyst without Zn was lower than the equilibrium value. The side reaction occurred (producing CH_4), and activity was not stable.

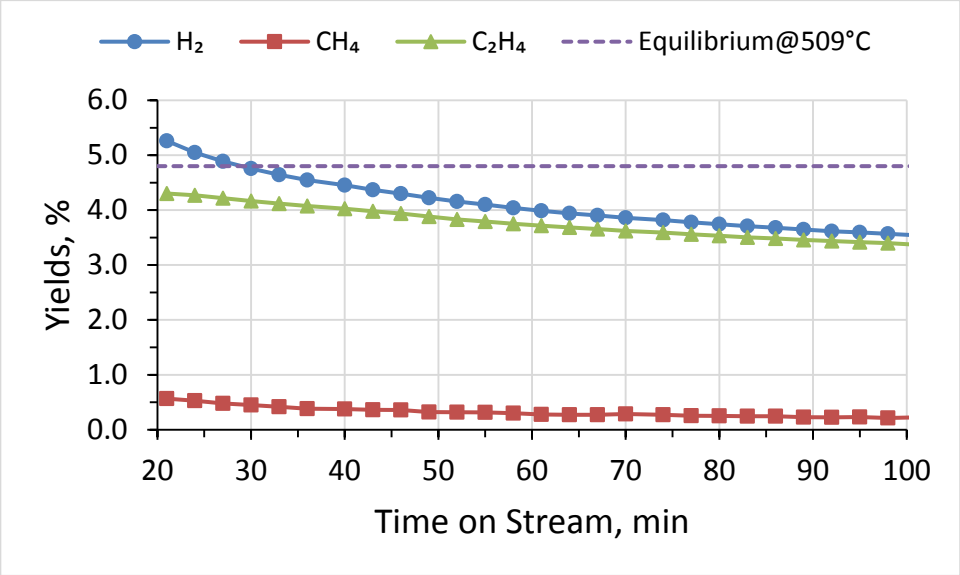

Figure 5-20 Product concentration changes with time over 1%Pt/ETS-2 at 509 °C, WHSV = 0.80 h^{-1}

The addition of 0.5wt% Zn into 1%Pt/ETS-2 did not promote the conversion since the ethylene yield was still below equilibrium, and side reactions were still present (CH_4 still presenting) even at relatively high feed flow rate. However, the Zn modification improved the catalyst stability.

Increasing the Zn content to 1wt%, the activity increased and stability was improved. The conversion reached equilibrium, as shown in Figure 5-22. Since ethane dehydrogenation is an endothermic reaction, the temperature measured in the middle of the catalyst bed was lower than that near the reactor wall because of the temperature gradient. So, the overall product yields were between the equilibrium and the highest point near the wall. However, side reactions (CH_4 by-product) still occurred at relatively lower space velocity.

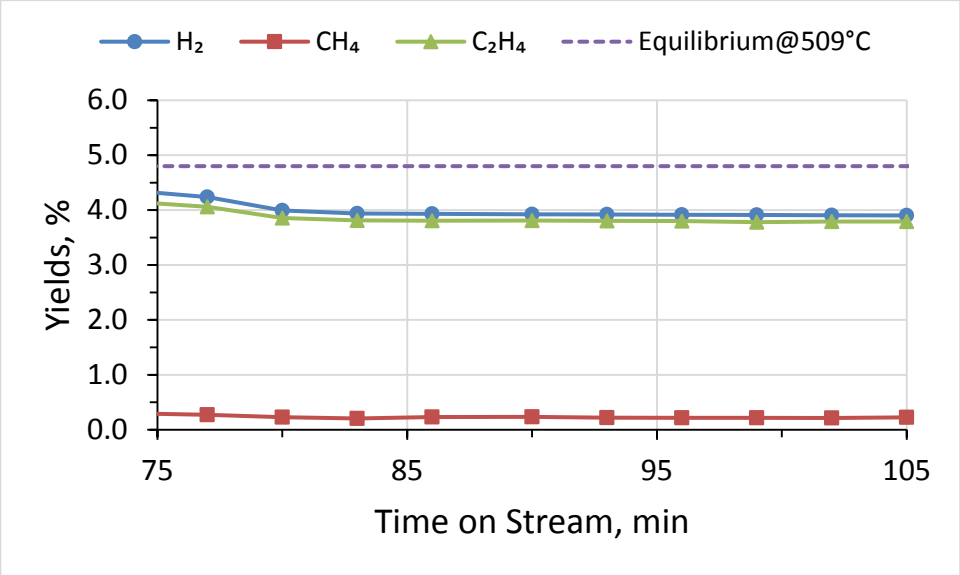

Figure 5-21 Product concentration changes with time over 0.5%Zn, 1%Pt/ETS-2 at 509 °C, WHSV = 1.13 h^{-1}

When the WHSV increased from 0.88h^{-1} to 1.14 h^{-1}, the by-product methane disappeared, as shown in Figure 5-23. The ethylene yield still stayed around equilibrium. Meanwhile, hydrogen yield was gradually reduced with reaction time and close to ethylene yield.

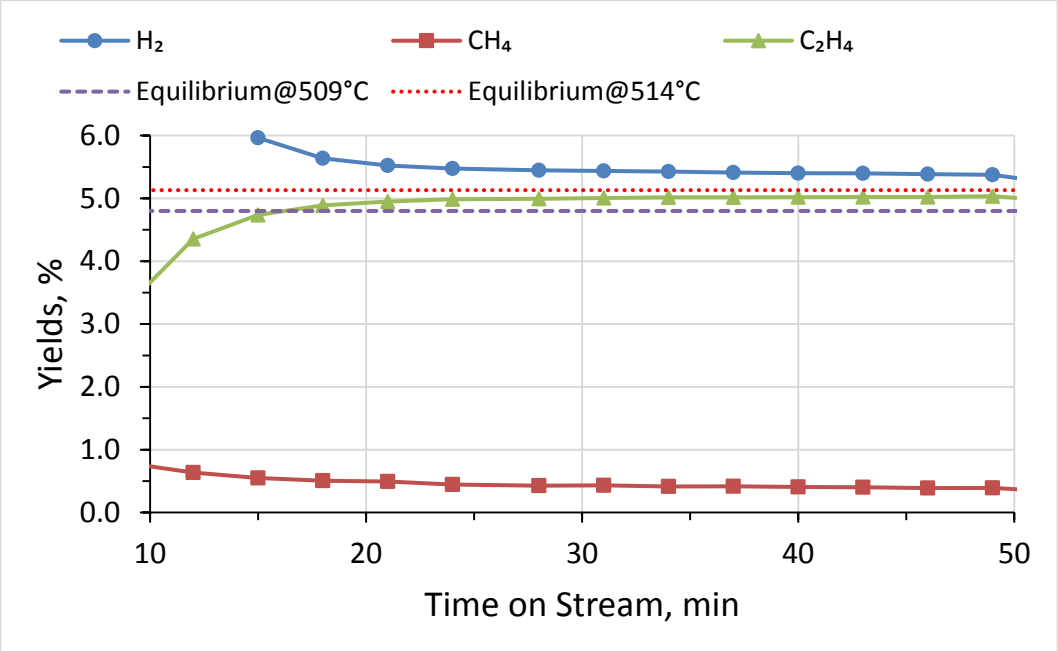

Figure 5-22 Product concentration changes with time over 1%Zn, 1%Pt/ETS-2 at 509 °C, WHSV = 0.88 h^{-1}

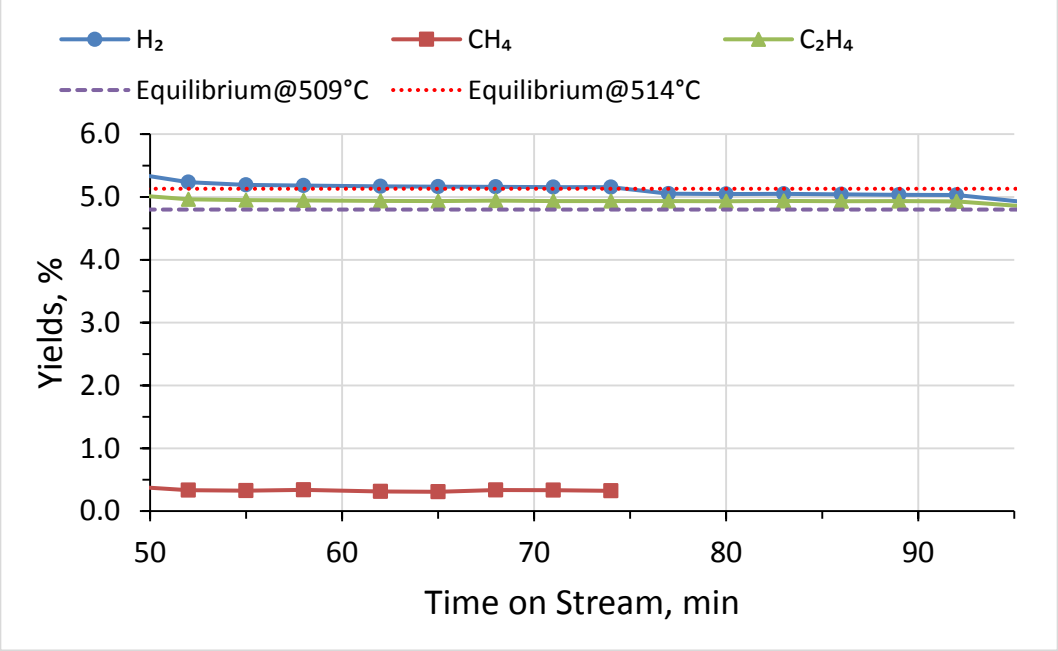

Figure 5-23 Product concentration changes with time over 1%Zn, 1%Pt/ETS-2 at 509 °C, WHSV = 1.14 h^{-1}

As shown in Figure 5-24and Figure 5-25, when the Zn content increased to 2 wt%, the hydrogen and ethylene yields were similar at low feed flow rate, even though side reactions still existed. However, when feed flow rate increased, methane disappeared, and the ethylene and hydrogen yield became identical.

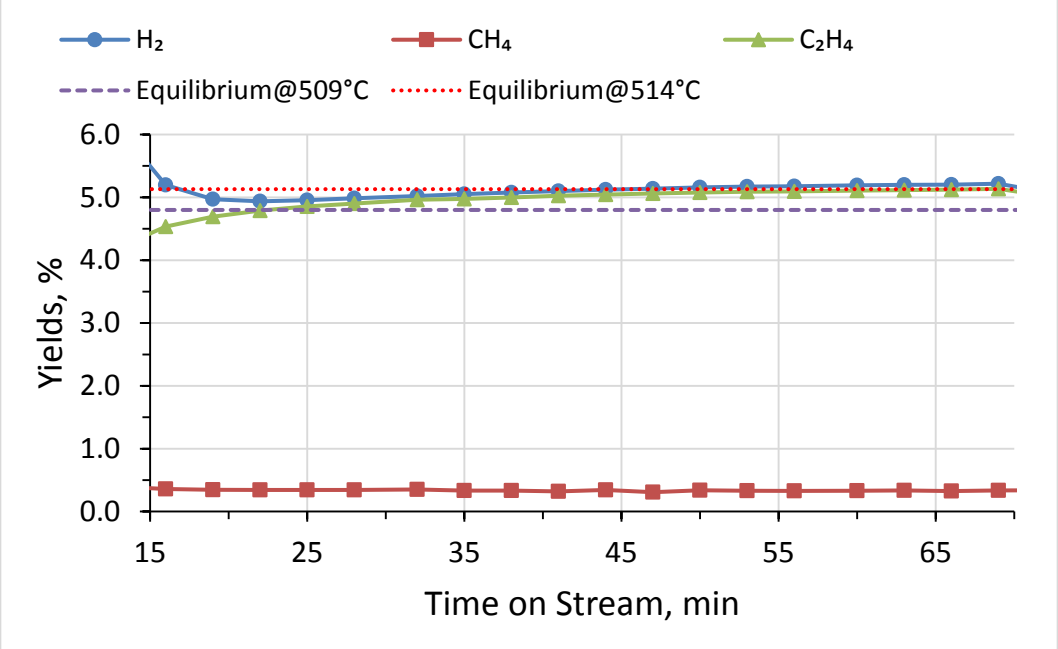

Figure 5-24 Product yield changes with time over 2%Zn, 1%Pt/ETS-2 at 509 °C, WHSV = 0.87 h^{-1}

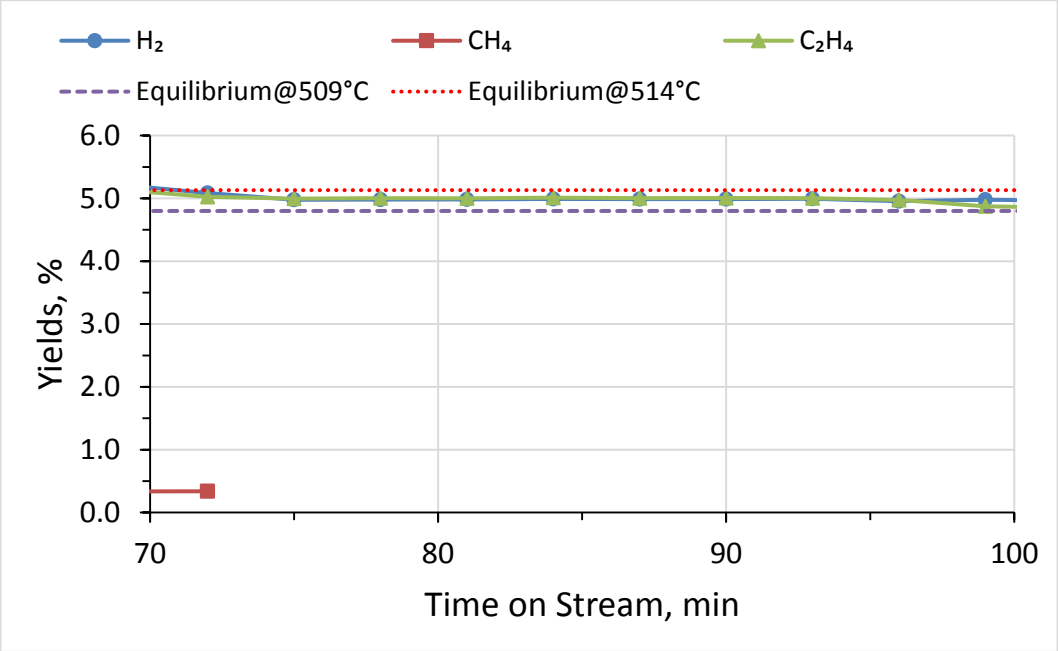

Figure 5-25 Product yield changes with time over 2%Zn, 1%Pt/ETS-2 at 509 °C, WHSV = 1.13 h^{-1}

Further increase of Zn content to 5wt%, suppressed side reactions even at low space velocity (0.89 h^{-1}). The conversion reached equilibrium state, as shown in Figure 5-26.

As shown in Figure 5-27, when Zn content increased to 7.5 wt%, the side reactions disappeared at low space velocity, the product yields were maintained around the equilibrium, and the activity increased further. The hydrogen yield was slightly higher than that of the ethylene. Zn modification enhanced the catalyst stability.

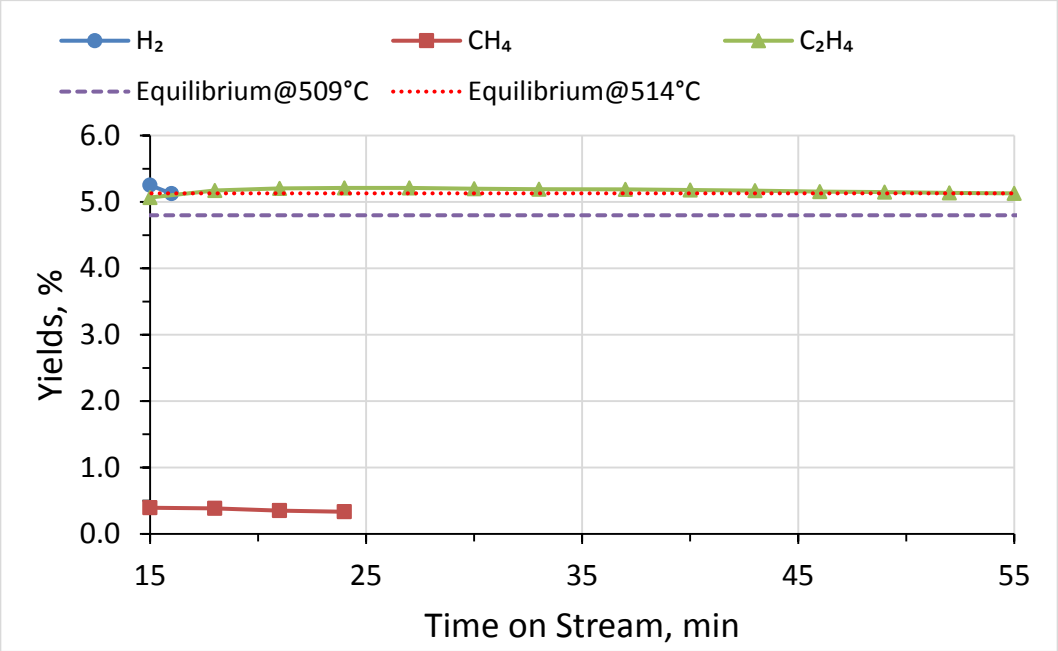

Figure 5-26 Product yield changes with time over 5%Zn, 1%Pt/ETS-2 at 509 °C, WHSV = 0.89 h^{-1}

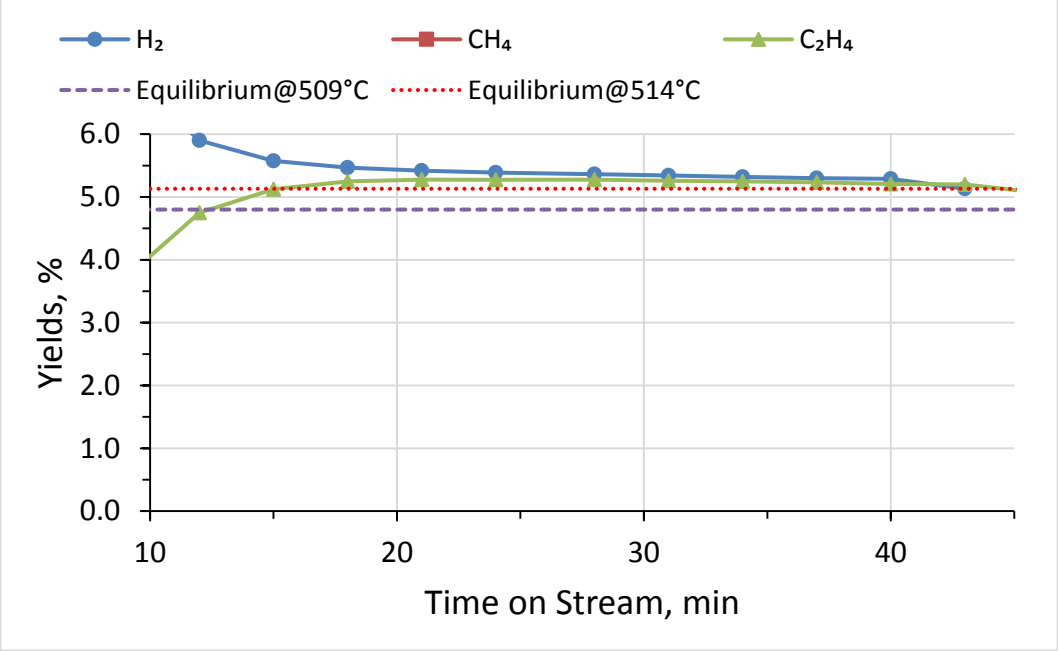

Figure 5-27 Product yield changes with time over 7.5%Zn, 1%Pt/ETS-2 at 509 °C, WHSV = 0.86 h^{-1}

The production yield changes with the Zn content were summarized in Figure 5-28. It can be seen that, to reach the reaction equilibrium, more than 1 wt% of Zn needed to be added. Higher Zn content (5 wt% or higher) helped to suppress the side reactions even at lower space velocity (0.87 h^{-1}).

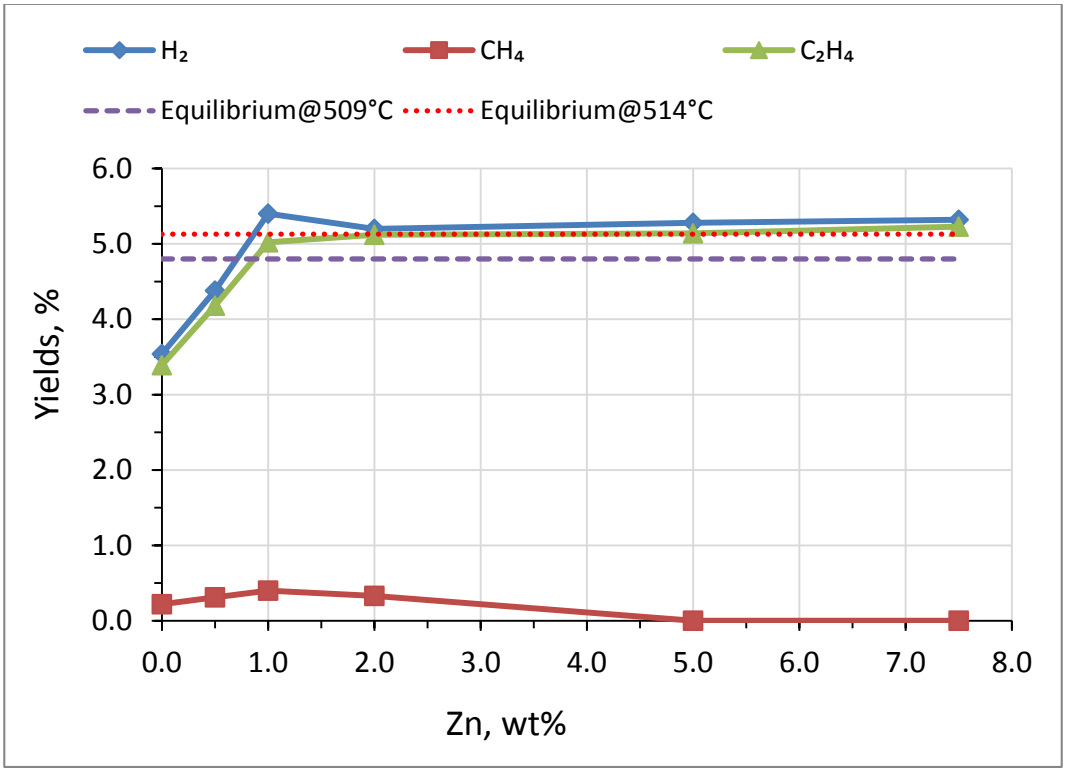

Figure 5-28 Product concentration change with Zn content on catalyst 1%Pt/ETS-2 at 509 °C, WHSV = 0.87h^{-1}

For Zn modified 1%Pt/ETS-2 catalysts, the yield changes of the main product ethylene, hydrogen, and by-product methane with different WHSV are shown in Figure 5-29. As expected, the product yields decreased with WHSV for all catalysts. However, the extent was quite different. From Figure 5-29, it can be seen that the

ethylene yields for all Zn modified catalysts were higher than that for the catalyst without Zn modification (1%Pt/ETS-2) in the whole range of space velocities studied. Among the Zn modified catalysts, 1%Pt/ETS-2 with 1 wt%, 2 wt%, and 5 wt% of Zn had similar high ethylene yields at all space velocities, but 1 wt% and 2 wt% of Zn modified catalysts had relatively higher methane yield at low space velocity. The catalyst 1%Pt, 5%Zn/ETS-2 had relatively stable ethylene yields at low space velocities, and its methane yields were suppressed to zero at all space velocities. The catalyst 1%Pt, 7.5%Zn/ETS-2 had the similar properties as 1%Pt, 5%Zn/ETS-2. Hydrogen yield had a similar trend to that of ethylene.

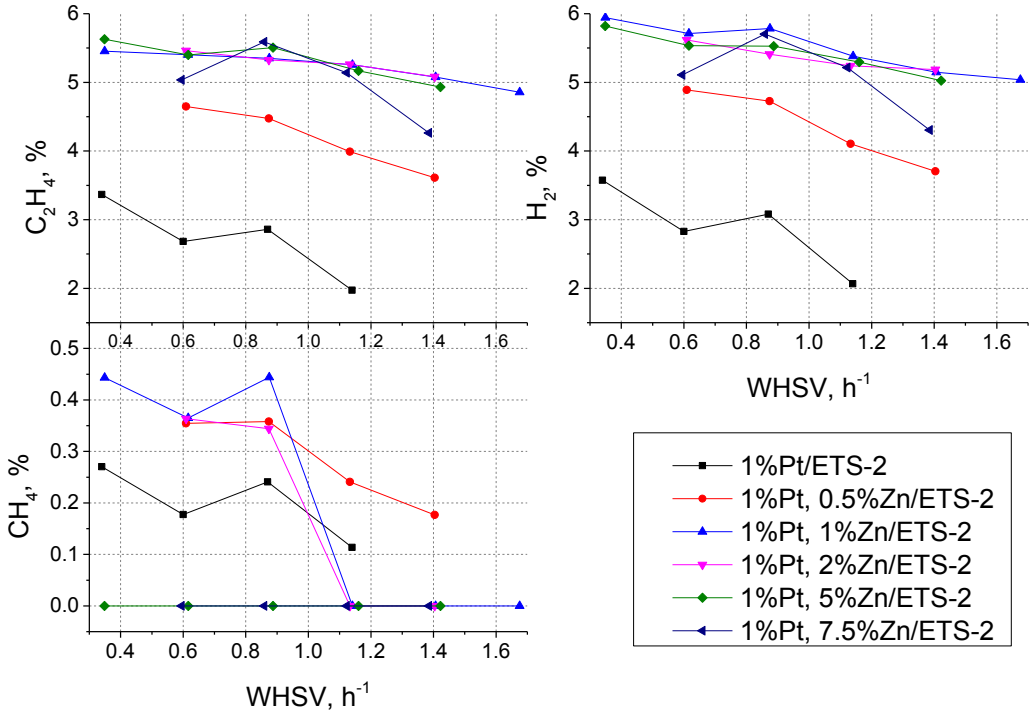

Figure 5-29 C_2H_4, H_2, and CH_4 yield change with space velocity on different content of Zn modified catalysts at 509 °C

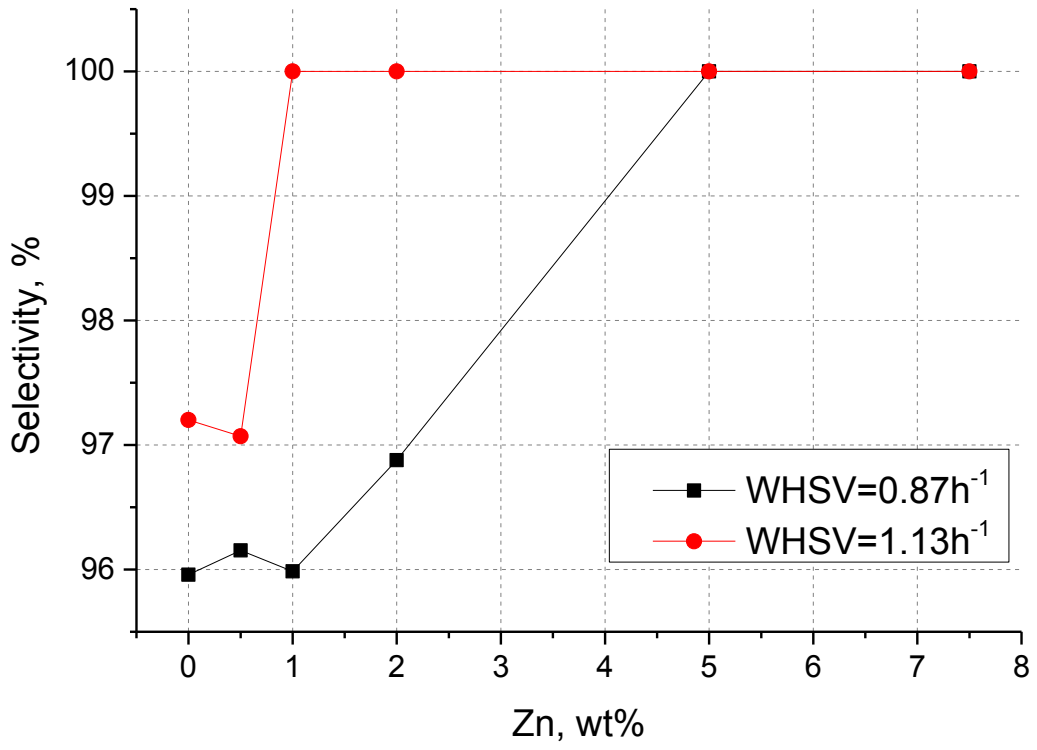

Figure 5-30 Effects of Zn content of catalysts 1%Pt/ETS-2 on selectivity of ethylene at WHSV=0.87 h^{-1} and 1.13h^{-1}, 509 °C

Figure 5-30 shows the effects of Zn content on the selectivity of ethylene at the space velocities 0.87 and 1.13 h^{-1}. From the figure, it can be seen that selectivity of ethylene increased with Zn content at both space velocities. Ethylene selectivity was able to reach 100% even at lower Zn content for high space velocity (1.13 h^{-1}).

5.3.4.2 Ce or/and Zn as Promoters

To study the promotion effect with the other metals, 1%Pt/ETS-2 was modified with Zn and Ce. The ethylene, hydrogen and methane yields at various

WHSVs are shown in Figure 5-31. From the figure, it can be seen that Zn enhanced ethylene yield, while Ce it. However, Ce could not eliminate side reactions even at high space velocity. The ethylene yield on Zn modified Catalyst (1%Pt, 1%Zn/ETS-2) was higher than that on only Zn and Ce modified catalysts (1%Pt, 1%Zn, 2.5%Ce/ETS-2). Zn and Zn-Ce modified catalysts could suppress the side reactions and minimize by-product methane at higher space velocities. Zn could also stabilize ethylene yields at higher space velocities. Hydrogen yield change was similar to that of ethylene.

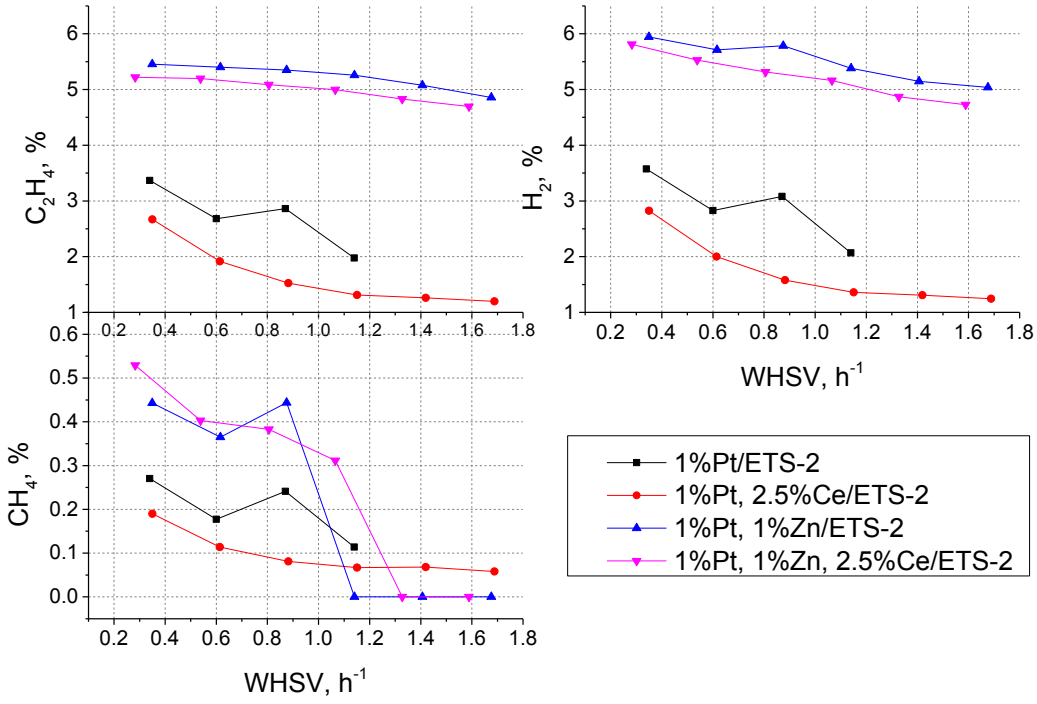

Figure 5-31 C_2H_4, H_2, and CH_4 yields change with WHSV at 509 °C over 1%Pt/ETS-2 modified with different promoters

To investigate the Ce modification effect for the support Al_2O_3, the catalysts modified with 1%Zn and 1%Zn+2.5%Ce were prepared. The ethylene, hydrogen, and methane yields at the various WHSVs are shown in Figure 5-32. Ethylene yield increased with space velocity for both catalysts, but both hydrogen and by-product methane yields decreased with space velocity. For the catalyst 1%Pt, 1%Zn/Al_2O_3, Ce inhibited the catalyst activities and thus decreased the ethylene yield. However, Ce modification did not help suppress by-product methane production for the alumina supported Pt catalysts.

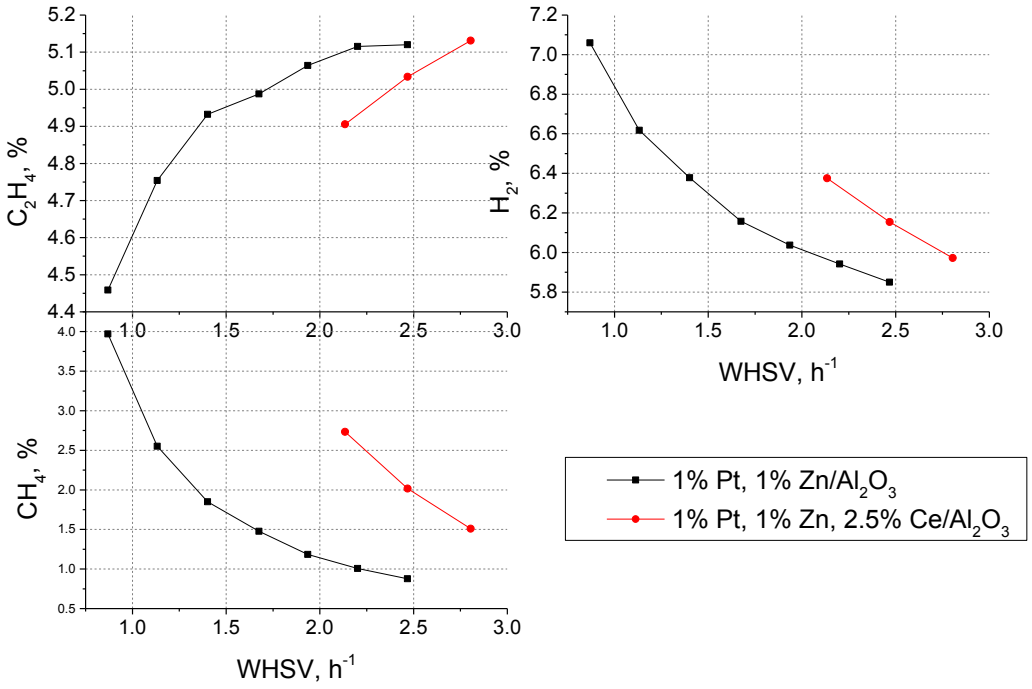

Figure 5-32 C_2H_4, H_2, and CH_4 yields change with space velocities at 509 °C over 1%Pt/Al_2O_3 catalyst modified with Zn and Ce promoters

5.3.4.3 Ce, Zn, and Sn Promoters

Ethane dehydrogenation testing results of the Zn and Ce modified Pd-Sn/Al_2O_3 catalyst are shown in Figure 5-33. From Figure 5-33, it can be seen that Zn and Ce enhanced the activity of Pd-Sn/Al_2O_3 catalyst. However, the side reaction increased as well. For 1%Pt/ETS-2 catalyst, Zn and Ce had similar promoting effects (Figure 5-31). However, for 1%Pt/Al_2O_3 catalyst, Zn acted as a promoter, while Ce acted as an inhibitor for catalyst activities (Figure 5-32).

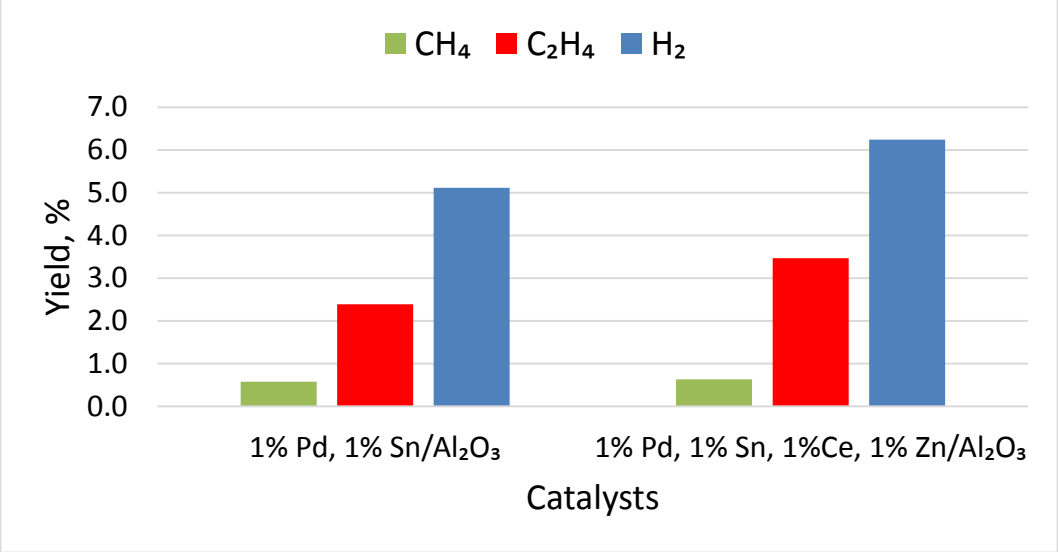

Figure 5-33 Product spectrum obtained with the 1%Pd, 1%Sn/Al_2O_3 and 1%Pd, 1%Ce, 1%Zn, 1%Sn/Al_2O_3 catalysts at 509 °C, and ethane WHSV = 0.28 h^{-1}

5.4 Conclusions

The Zn modification helped the Pt disperse on ETS-2 and Al_2O_3 supports, and therefore resulted in a significant improvement in ethane dehydrogenation performances. Pt was aggregated at high temperature. ZnO could react with the support to form new species. In the Pt catalysts, ZnO can be easily reduced by hydrogen. The new phase formation and strong interaction with the support of ZnO could lead to the decrease the reductibility of ZnO.

For the ethane dehydrogenation reaction, Pt showed a better performance than Pd; ETS-2 support was superior in reaction specificity to Al_2O_3 and clinoptilolite.

The addition of Zn in the Pt/ETS-2 catalyst improved the ethylene selectivity and stability significantly. The side reactions like coking and methane formation were effectively suppressed at a wider range of space velocities. With the Zn content increase, the activity of the catalysts increased, and the methane production was greatly suppressed. Pt-Zn alloy was formed and might act as the active species for ethane dehydrogenation that helped to reduce side reactions and shorten the time to reach the equilibrium. Residence time was a main factor that affected selectivity and activity.

The addition of Ce had detrimental effects on the Pt catalysts supported on both Al_2O_3 and ETS-2 supports.

Chapter 6. Conclusions and Suggestions for Future Work

6.1 General conclusions

Natural zeolite mordenite is abundant in nature. Monolithic mordenite rock fragments procured from New Zealand have good machinability and thermal stability. The crystal structure is stable up to 800 °C. The zeolite mordenite has uniform pore size distribution and has internal channels which can selectively separate hydrogen. All these features make the mordenite a good candidate as a high temperature membrane material for membrane reactors.

A membrane reactor with a natural mordenite membrane disk coupled with a Pt/Al_2O_3 catalyst packed bed was able to selectively extract hydrogen and shifted equilibrium of ethane dehydrogenation reaction at 500-550 °C. By increasing the area/volume ratio of the membrane reactor module from 0.04 m^{-1} to 0.16 m^{-1}, the ethylene yield increased from 6.5% to 15.6%. The membrane reactor showed a higher ethylene yield enhancement at 550 °C than at 500 °C, due to the increase in hydrogen permeation rate. Ethylene yield increased from 6.5% at 500 °C to 8.9% at 550 °C compared to the conventional packed bed reactor with the area/volume ratio 0.04 m^{-1}. Lower Damköhler-Peclet number favored the higher ethylene yield improvement.

For ethane dehydrogenation reaction, Pt showed a better performance than Pd; ETS-2 support was superior to Al_2O_3 and clinoptilolite.

The Zn modification promoted the Pt dispersion on ETS-2 and Al_2O_3 supports, and therefore significantly improved ethane dehydrogenation performance. The Pt-Zn alloy phase generated on catalyst surface could be active species for ethane dehydrogenation that helped to reduce side reactions. The addition of Zn in the Pt/ETS-2 catalyst improved the ethylene selectivity and stability significantly. The side reactions like coking and methane formation were effectively suppressed. As the Zn content increased, the activity of the catalysts increased as well, while the methane production was greatly suppressed. Residence time was one of the main factors that affected selectivity and activity. Pt particle aggregation at high temperature caused catalyst deactivation.

The addition of Ce had detrimental effects on the Pt catalysts supported on both Al_2O_3 and ETS-2 supports.

6.2 Suggestions for future work

Selectivity and permeance are key factors for membrane performance and effectiveness. Knudsen flow in membrane has limited selectivity since the selectivity depends on $\sqrt{M_B/M_A}$, because the square root of the molecular weight ratio of the two gas molecules is a small number. However, Knudsen flow occurs in pores $2 < d < 100\,nm$, which is in meso-pores ($2 < d < 50\,nm$) and small macro-pores range ($d > 50\,nm$). Knudsen flow significantly contributes to permeance. Permeance is a crucial parameter of process economics. Knudsen permeance is not a function of pressure. It is proportional to $\sqrt{1/T}$. Viscous flow also occurs in the range ($d > 20\,nm$) that Knudsen flow does, but it is not selective.

High temperature membranes require a material with good thermal stability, physically and chemically stable at high working temperatures. The membrane material's coefficient of thermal expansion (CTE) should be close to the sealing parts, so a tight sealing can be maintained.

Therefore, a good high temperature membrane should have selectivity better than Knudsen diffusion, high permeance, and good thermal stability at working temperatures.

Pt-Zn/ETS-2 catalyst has the ability to suppress side reactions including coking and methane formation. However, its activity could be improved (higher space velocity). Compared to alumina support, its specific surface area is very low, which affects the dispersion of active metal species like Pt, reduces the active sites on the surface, and thus limits the activity. Therefore, further modification of the catalysts is a topic that should be pursued in the future.

ETS-2 is not stable at high temperature. It can easily change phase above 600 °C, and it is also reactive with supported metal components at high temperature. These will cause the catalyst to lose activity and will reduce the run cycles. This is another area of potential future improvement.

Active metal components aggregating at high temperature is a major issue for catalyst deactivation. Aggregation of Pt particles still occurred on ETS-2 support even with Zn modification. Future research is needed in order to eliminate or mitigate the problem.

A more systematic and thorough investigation and characterization of the catalyst and the support, such as optimal metal compositions and chemistry of

catalyst preparation, will help understand reaction mechanisms and control catalyst quality.

References

[1] W. R. True: "Global Ethylene Production Continues Advance in 2009", *Oil & Gas Journal*, **2010**, 108 (27), 34-38.

[2] W. R. True: "Global Ethylene Capacity Poised for Major Expansion", *Oil & Gas Journal*, **2013**, 111 (7), 90-95.

[3] W. R. True: "Global Ethylene Capacity Continues Advance in 2011", *Oil & Gas Journal*, **2012**, 110 (7), 78-84.

[4] L. Bewley: "Ihs Wpc 2012: Shale Reshapes Ethylene Markets", *Chemical Week*, **2012**, 174 (10), 15.

[5] L. Bewley and R. Westervelt: "Mideast Producers Reap Benefits of Low-Cost Production. (Cover Story)", *Chemical Week*, **2011**, 173 (29), 32-33.

[6] C. Carr: "Global Ethylene Outlook: One Product..... Many Strategies", **2013**, http://ihsglobalevents.com/wpc2013/files/2013/03/Carr_20131.pdf.

[7] S. Jenkins: "Shale Gas Ushers in Ethylene Feed Shifts", *Chemical Engineering*, **2012**, October, 17-19.

[8] K. Bullis: "Shale Gas Will Fuel a U.S. Manufacturing Boom", *MIT Technology Review*, **2013**, 116 (2), 73-74.

[9] J. Chang: "Nova Explores Ethylene Expansions", *ICIS Chemical Business*, **2013**, 283 (12), 12.

[10] The Dow Chemical Company: "Dow to Build New Ethylene Production Plant at Dow Texas Operations", **2012**.

[11] Nexant: "North American Shale Gas: Opportunity or Threat for Global Ethylene Producers?", **2012**, http://www.chemsystems.com/reports/search/docs/prospectus/STMC12_Shale%20Gas_pros.pdf.

[12] K. Holmquist: "Global Ethylene Surplus to Last through 2011", *Oil & Gas Journal*, **2010**, 108 (27), 46-52.

[13] H. Zimmermann and R. Walzl: '*Ethylene*', in "Ullmann's Encyclopedia of Industrial Chemistry", 6th edn, 465-529; **2009**, Wiley-VCH Verlag GmbH & Co. KGaA.

[14] J. Towfighi, M. Sadrameli, and A. Niaei: "Coke Formation Mechanisms and Coke Inhibiting Methods in Pyrolysis Furnaces", *Journal of Chemical Engineering of Japan*, **2002**, 35 (10), 923-937.

[15] T. Ren, M. Patel, and K. Blok: "Olefins from Conventional and Heavy Feedstocks: Energy Use in Steam Cracking and Alternative Processes", *Energy*, **2006**, 31 (4), 425-451.

[16] K. S. W. Sing, D. H. Everett, R. A. W. Haul, L. Moscou, R. A. Pierotti, J. Rouquerol, and T. Siemieniewska: "Reporting Physisorption Data for Gas/Solid Systems with Special Reference to the Determination of Surface Area and Porosity", *Pure and Applied Chemistry*, **1985**, 57 (4), 603-619.

[17] M. Huttepain and A. Oberlin: "Microtexture of Nongraphitizing Carbons and Tem Studies of Some Activated Samples", *Carbon*, **1990**, 28 (1), 103-111.

[18] H. P. Hsieh: '*Chapter 4 Physical, Chemical and Surface Properties of Inorganic Membranes*', in "Membrane Science and Technology Series, 3: Inorganic Membranes for Separation and Reaction", 93-147; **1996**, Elsevier.

[19] A. J. Burggraaf: '*Chapter 9 Transport and Separation Properties of Membranes with Gases and Vapours*', in "Membrane Science and Technology Series, 4: Fundamentals of Inorganic Membrane Science and Technology", (eds. A. J. Burggraaf and L. Cot), 331-433; **1996**, Elsevier.

[20] Y. Cen and R. N. Lichtenthaler: '*Chapter 3 Vapor Permeation*', in "Membrane Science and Technology Series, 2: Membrane Separations Technology--Principles and Applications", (eds. D. N. Richard and S. A. Stern), 85-112; **1995**, Elsevier.

[21] B. Fayyaz-Najafi: "Nanoporous Silicon Carbide Membranes: Preparation and Reactive Applications", Ph.D. thesis, University of Southern California, Ann Arbor, **2005**.

[22] W. J. Koros, Y. H. Ma, and T. Shimidzu: "Terminology for Membranes and Membrane Processes (Iupac Recommendation 1996)", *Journal of Membrane Science*, **1996**, 120 (2), 149-159.

[23] M. Daramola, E. Aransiola, and T. Ojumu: "Potential Applications of Zeolite Membranes in Reaction Coupling Separation Processes", *Materials*, **2012**, 5 (11), 2101-2136.

[24] S. Tennison: "Current Hurdles in the Commercial Development of Inorganic Membrane Reactors", *Membrane Technology*, **2000**, 2000 (128), 4-9.

[25] C. Téllez and M. Menéndez: '*8 Zeolite Membrane Reactors*', in "Membranes for Membrane Reactors: Preparation, Optimization and Selection", (eds. A. Basile and F. Gallucci), 243-273; **2011**, John Wiley & Sons, Ltd.

[26] M. E. E. Abashar and A. A. Al-Rabiah: "Production of Ethylene and Cyclohexane in a Catalytic Membrane Reactor", *Chemical Engineering and Processing*, **2005**, 44 (11), 1188-1196.

[27] J.-A. Dalmon, A. Cruz-López, D. Farrusseng, N. Guilhaume, E. Iojoiu, J.-C. Jalibert, S. Miachon, C. Mirodatos, A. Pantazidis, M. Rebeilleau-Dassonneville, Y. Schuurman, and A. C. van Veen: "Oxidation in Catalytic Membrane Reactors", *Applied Catalysis A: General*, **2007**, 325 (2), 198-204.

[28] L. Chalakov, L. K. Rihko-Struckmann, B. Munder, and K. Sundmacher: "Oxidative Dehydrogenation of Ethane in an Electrochemical Packed-Bed Membrane Reactor: Model and Experimental Validation", *Chemical Engineering Journal*, **2009**, 145 (3), 385-392.

[29] M. P. Lobera, M. Balaguer, J. Garcia-Fayos, and J. M. Serra: "Rare Earth-Doped Ceria Catalysts for Odhe Reaction in a Catalytic Modified Miec Membrane Reactor", *Chemcatchem*, **2012**, 4 (12), 2102-2111.

[30] M. L. Rodriguez, D. E. Ardissone, E. Heracleous, A. A. Lemonidou, E. López, M. N. Pedernera, and D. O. Borio: "Oxidative Dehydrogenation of Ethane to Ethylene in a Membrane Reactor: A Theoretical Study", *Catalysis Today*, **2010**, 157 (1–4), 303-309.

[31] H. Q. Jiang, Z. W. Cao, S. Schirrmeister, T. Schiestel, and J. Caro: "A Coupling Strategy to Produce Hydrogen and Ethylene in a Membrane

Reactor", *Angewandte Chemie-International Edition*, **2010**, 49 (33), 5656-5660.

[32] H. H. Wang, C. Tablet, T. Schiestel, and J. Caro: "Hollow Fiber Membrane Reactors for the Oxidative Activation of Ethane", *Catalysis Today*, **2006**, 118 (1-2), 98-103.

[33] D. Ahchieva, M. Peglow, S. Heinrich, L. Mörl, T. Wolff, and F. Klose: "Oxidative Dehydrogenation of Ethane in a Fluidized Bed Membrane Reactor", *Applied Catalysis A: General*, **2005**, 296 (2), 176-185.

[34] S. Crapanzano, I. V. Babich, and L. Lefferts: "Selection of Mixed Conducting Oxides for Oxidative Dehydrogenation of Propane with Pulse Experiments", *Applied Catalysis a-General*, **2011**, 391 (1-2), 70-77.

[35] O. Czuprat, J. Caro, V. A. Kondratenko, and E. V. Kondratenko: "Dehydrogenation of Propane with Selective Hydrogen Combustion: A Mechanistic Study by Transient Analysis of Products", *Catalysis Communications*, **2010**, 11 (15), 1211-1214.

[36] D. S. Coombs, A. Alberti, T. Armbruster, G. Artioli, C. Colella, E. Galli, J. D. Grice, F. Liebau, J. A. Mandarino, H. Minato, E. H. Nickel, E. Passaglia, D. R. Peacor, S. Quartieri, R. Rinaldi, M. Ross, R. E. Sheppard, E. Tillmanns, and G. Vezzalini: "Recommended Nomenclature for Zeolite Minerals: Report of the Subcommittee on Zeolites of the International Mineralogical Association, Commission on New Minerals and Mineral Names", *Mineralogical Magazine*, **1998**, 62 (4), 533-571.

[37] M. W. Ackley, S. U. Rege, and H. Saxena: "Application of Natural Zeolites in the Purification and Separation of Gases", *Microporous and Mesoporous Materials*, **2003**, 61 (1–3), 25-42.

[38] D. C. L. How: "Xi.-on Mordenite, a New Mineral from the Trap of Nova Scotia", *Journal of the Chemical Society*, **1864**, 17 (0), 100-104.

[39] "Mordenite", http://www.mindat.org/min-2779.html.

[40] S. A. Hoseinzadeh Hejazi: "Characterization of Natural Zeolite Membranes for Molecular Hydrogen/Carbon Dioxide Separations by Single Gas Permeation", M.S. thesis, University of Alberta (Canada), Ann Arbor, **2011**.

[41] P. Simoncic and T. Armbruster: "Peculiarity and Defect Structure of the Natural and Synthetic Zeolite Mordenite: A Single-Crystal X-Ray Study", *American Mineralogist*, **2004**, 89 (2-3), 421-431.

[42] M. Földvári: "Handbook of Thermogravimetric System of Minerals and Its Use in Geological Practice", 101-102; **2011**, BUDAPEST, Geological Institute of Hungary (=Magyar Állami Földtani Intézet).

[43] G. Cruciani: "Zeolites Upon Heating: Factors Governing Their Thermal Stability and Structural Changes", *Journal of Physics and Chemistry of Solids*, **2006**, 67 (9–10), 1973-1994.

[44] A. W. Sleight: "Negative Thermal Expansion Materials", *Current Opinion in Solid State and Materials Science*, **1998**, 3 (2), 128-131.

[45] K. D. Hammonds, V. Heine, and M. T. Dove: "Rigid-Unit Modes and the Quantitative Determination of the Flexibility Possessed by Zeolite

Frameworks", *The Journal of Physical Chemistry B*, **1998**, 102 (10), 1759-1767.

[46] V. Heine, P. R. L. Welche, and M. T. Dove: "Geometrical Origin and Theory of Negative Thermal Expansion in Framework Structures", *Journal of the American Ceramic Society*, **1999**, 82 (7), 1793-1802.

[47] A. MARTUCCI, M. SACERDOTI, G. CRUCIANI, and C. DALCONI: "In Situ Time Resolved Synchrotron Powder Diffraction Study of Mordenite", *European Journal of Mineralogy*, **2003**, 15 (3), 485-493.

[48] E. Chmielewská: '*Chapter 18 an Update of Zeolitic and Other Traditional Adsorption and Ion Exchange Materials in Water Cleanup Processes*', in "Handbook of Natural Zeolites", (eds. V. J. Inglezakis and A. A. Zorpas), 436-452; **2012**, Bentham eBooks, Bentham Science Publishers.

[49] G. Horvath and K. Kawazoe: "Method for the Calculation of Effective Pore Size Distribution in Molecular Sieve Carbon", *Journal of Chemical Engineering of Japan*, **1983**, 16 (6), 470-475.

[50] R. L. Hay and R. A. Sheppard: "Occurrence of Zeolites in Sedimentary Rocks: An Overview", *Reviews in Mineralogy and Geochemistry*, **2001**, 45 (1), 217-234.

[51] M. Shekarchi, B. Ahmadi, and M. Najimi: '*Chapter 27 Use of Natural Zeolite as Pozzolanic Material in Cement and Concrete Composites*', in "Handbook of Natural Zeolites", (eds. V. J. Inglezakis and A. A. Zorpas), 665-694; **2012**, Bentham eBooks, Bentham Science Publishers.

[52] D. L. Bish and J. W. Carey: "Thermal Behavior of Natural Zeolites", *Reviews in Mineralogy and Geochemistry*, **2001**, 45 (1), 403-452.

[53] F. Gallucci, E. Fernandez, P. Corengia, and M. van Sint Annaland: "Recent Advances on Membranes and Membrane Reactors for Hydrogen Production", *Chemical Engineering Science*, **2013**, 92 (0), 40-66.

[54] J. Gascon, F. Kapteijn, B. Zornoza, V. Sebastián, C. Casado, and J. Coronas: "Practical Approach to Zeolitic Membranes and Coatings: State of the Art, Opportunities, Barriers, and Future Perspectives", *Chemistry of Materials*, **2012**, 24 (15), 2829-2844.

[55] M. O. Daramola, E. F. Aransiola, and T. V. Ojumu: "Potential Applications of Zeolite Membranes in Reaction Coupling Separation Processes", *Materials (1996-1944)*, **2012**, 5 (11), 2101-2136.

[56] S. M. Hashim, A. R. Mohamed, and S. Bhatia: "Catalytic Inorganic Membrane Reactors: Present Research and Future Prospects", *Reviews in Chemical Engineering*, **2011**, 27 (3/4), 157-178.

[57] A. M. Champagnie, T. T. Tsotsis, R. G. Minet, and A. I. Webster: "A High Temperature Catalytic Membrane Reactor for Ethane Dehydrogenation", *Chemical Engineering Science*, **1990**, 45 (8), 2423-2429.

[58] E. Gobina and R. Hughes: "Ethane Dehydrogenation Using a High-Temperature Catalytic Membrane Reactor", *Journal of Membrane Science*, **1994**, 90 (1–2), 11-19.

[59] E. Gobina, K. Hou, and R. Hughes: "Ethane Dehydrogenation in a Catalytic Membrane Reactor Coupled with a Reactive Sweep Gas", *Chemical Engineering Science*, **1995**, 50 (14), 2311-2319.

[60] E. Gobina, K. Hou, and R. Hughes: "Equilibrium-Shift in Alkane Dehydrogenation Using a High-Temperature Catalytic Membrane Reactor", *Catalysis Today*, **1995**, 25 (3-4), 365-370.

[61] E. Gobina, K. H. Hou, and R. Hughes: "A Comparative Evaluation of High-Temperature Membrane Systems for Catalytic Processing", *Chemical Engineering Communications*, **1998**, 166, 157-181.

[62] J. Szegner, K. L. Yeung, and A. Varma: "Effect of Catalyst Distribution in a Membrane Reactor: Experiments and Model", *Aiche Journal*, **1997**, 43 (8), 2059-2072.

[63] W. An, P. Swenson, L. Wu, T. Waller, A. Ku, and S. M. Kuznicki: "Selective Separation of Hydrogen from C1/C2 Hydrocarbons and Co2 through Dense Natural Zeolite Membranes", *Journal of Membrane Science*, **2011**, 369 (1–2), 414-419.

[64] S. T. Oyama and H. Lim: "An Operability Level Coefficient (Olc) as a Useful Tool for Correlating the Performance of Membrane Reactors", *Chemical Engineering Journal*, **2009**, 151 (1–3), 351-358.

[65] S. Battersby, P. W. Teixeira, J. Beltramini, M. C. Duke, V. Rudolph, and J. C. Diniz da Costa: "An Analysis of the Peclet and Damkohler Numbers for Dehydrogenation Reactions Using Molecular Sieve Silica (Mss) Membrane Reactors", *Catalysis Today*, **2006**, 116 (1), 12-17.

[66] R. S. Vincent, R. P. Lindstedt, N. A. Malik, I. A. B. Reid, and B. E. Messenger: "The Chemistry of Ethane Dehydrogenation over a Supported Platinum Catalyst", *Journal of Catalysis*, **2008**, 260 (1), 37-64.

[67] U. Fekl and K. I. Goldberg: '*Homogeneous Hydrocarbon C-H Bond Activation and Functionalization with Platinum*', in "Advances in Inorganic Chemistry", 259-320; **2003**, Academic Press.

[68] F. E. Frey and W. F. Huppke: "Equilibrium Dehydrogenation of Ethane, Propane, and the Butanes", *Industrial and Engineering Chemistry*, **1933**, 25, 54-59.

[69] D. J. Fabian and A. J. B. Robertson: "The Dehydrogenation of Ethane at Low Pressure on Incandescent Platinum", *Proceedings of the Royal Society of London Series a-Mathematical and Physical Sciences*, **1956**, 237 (1208), 1-16.

[70] J. A. Cusumano, G. W. Dembinski, and J. H. Sinfelt: "Chemisorption and Catalytic Properties of Supported Platinum", *Journal of Catalysis*, **1966**, 5 (3), 471-475.

[71] B. S. Gudkov, L. Guczi, and P. Tétényi: "Kinetics and Mechanism of Ethane Hydrogenolysis on Silica-Supported Platinum and Platinum-Iron Catalysts", *Journal of Catalysis*, **1982**, 74 (2), 207-215.

[72] G. C. Bond, F. Garin, and G. Maire: "Characterization of the Standard Platinum/Silica Catalyst Europt-1: Vi. Catalytic Properties", *Applied Catalysis*, **1988**, 41 (0), 313-335.

[73] C. De la Cruz and N. Sheppard: "Adsorption and Dehydrogenation of Ethane on a Silica-Supported Platinum Catalyst Monitored in the Temperature Range 90-294 K by Ftir Spectroscopy", *Physical Chemistry Chemical Physics*, **1999**, 1 (2), 329-332.

[74] H. E. Swift, F. E. Lutinski, and H. H. Tobin: "Catalytic Aluminas: Iii. Physical and Catalytic Properties of Nickel and Platinum Impregnated Eta and Gamma Alumina", *Journal of Catalysis*, **1966**, 5 (2), 285-292.

[75] P. Mériaudeau, O. H. Ellestad, M. Dufaux, and C. Naccache: "Metal-Support Interaction. Catalytic Properties of Ti02-Supported Platinum, Iridium, and Rhodium", *Journal of Catalysis*, **1982**, 75 (2), 243-250.

[76] R. Szymanski and H. Charcosset: "Preparation, Characterization and Catalytic Properties of Carbon-Supported Platinum-Zirconium Alloy Catalysts", *Journal of Molecular Catalysis*, **1984**, 25 (1–3), 337-345.

[77] J. Salmones, J.-A. Wang, J. A. Galicia, and G. Aguilar-Rios: "H2 Reduction Behaviors and Catalytic Performance of Bimetallic Tin-Modified Platinum Catalysts for Propane Dehydrogenation", *Journal of Molecular Catalysis A: Chemical*, **2002**, 184 (1–2), 203-213.

[78] A. Virnovskaia, S. Jørgensen, J. Hafizovic, Ø. Prytz, E. Kleimenov, M. Hävecker, H. Bluhm, A. Knop-Gericke, R. Schlögl, and U. Olsbye: "In Situ Xps Investigation of Pt(Sn)/Mg(Al)O Catalysts During Ethane Dehydrogenation Experiments", *Surface Science*, **2007**, 601 (1), 30-43.

[79] A. Virnovskaia, E. Rytter, and U. Olsbye: "Kinetic and Isotopic Study of Ethane Dehydrogenation over a Semicommercial Pt,Sn/Mg(Al)O Catalyst", *Industrial & Engineering Chemistry Research*, **2008**, 47 (19), 7167-7177.

[80] V. Galvita, G. Siddiqi, P. Sun, and A. T. Bell: "Ethane Dehydrogenation on Pt/Mg(Al)O and Ptsn/Mg(Al)O Catalysts", *Journal of Catalysis*, **2010**, 271 (2), 209-219.

[81] P. Sun, G. Siddiqi, W. C. Vining, M. Chi, and A. T. Bell: "Novel Pt/Mg(in)(Al)O Catalysts for Ethane and Propane Dehydrogenation", *Journal of Catalysis*, **2011**, 282 (1), 165-174.

[82] S. F. Hakonsen, B. Silberova, and A. Holmen: "Oxidative Dehydrogenation of Ethane on Pt-Sn Impregnated Monoliths", *Topics in Catalysis*, **2007**, 45 (1-4), 61-67.

[83] S. F. Håkonsen, J. C. Walmsley, and A. Holmen: "Ethene Production by Oxidative Dehydrogenation of Ethane at Short Contact Times over Pt-Sn Coated Monoliths", *Applied Catalysis A: General*, **2010**, 378 (1), 1-10.

[84] R. Gudgila and C. A. Leclerc: "Support Effects on the Oxidative Dehydrogenation of Ethane to Ethylene over Platinum Catalysts", *Industrial & Engineering Chemistry Research*, **2011**, 50 (14), 8438-8443.

[85] L. M. Ombaka, P. Ndungu, and V. O. Nyamori: "Usage of Carbon Nanotubes as Platinum and Nickel Catalyst Support in Dehydrogenation Reactions", *Catalysis Today*, **2013**, 217 (0), 65-75.

[86] A. T. Bell: "Thermal Dehydrogenation of Ethane on Pt and Pt-Sn Catalysts: Effects of Particle Size and Sn/Pt Ratio on Catalyst Activity, Selectivity, and

Stability", *Abstracts of Papers of the American Chemical Society*, **2012**, 244, 1.

[87] J. Wu, Z. Peng, P. Sun, and A. T. Bell: "n-Butane Dehydrogenation over Pt/Mg(in)(Al)O", *Applied Catalysis A: General*, **2014**, 470 (0), 208-214.

[88] E. A. de Graaf, G. Rothenberg, P. J. Kooyman, A. Andreini, and A. Bliek: "Pt0.02sn0.003mg0.06 on Gamma-Alumina: A Stable Catalyst for Oxidative Dehydrogenation of Ethane", *Applied Catalysis a-General*, **2005**, 278 (2), 187-194.

[89] J. Jia, J. Shen, L. Lin, Z. Xu, T. Zhang, and D. Liang: "A Study on Reduction Behaviors of the Supported Platinum–Iron Catalysts", *Journal of Molecular Catalysis A: Chemical*, **1999**, 138 (2–3), 177-184.

[90] R. Lødeng, O. A. Lindvag, S. Kvisle, H. Reier-Nielsen, and A. Holmen: '*Oxidative Dehydrogenation of Ethane over Pt and Pt/Rh Gauze Catalysts at Very Short Contact Times*', in "Studies in Surface Science and Catalysis", (eds. D. S. F. F. A. V. A. Parmaliana and A. F), 641-646; **1998**, Elsevier.

[91] P. Biloen, F. M. Dautzenberg, and W. M. H. Sachtler: "Catalytic Dehydrogenation of Propane to Propene over Platinum and Platinum-Gold Alloys", *Journal of Catalysis*, **1977**, 50 (1), 77-86.

[92] A. Loaiza, M. Xu, and F. Zaera: "On the Mechanism of the H–D Exchangereaction in Ethane over Platinum Catalysts", *Journal of Catalysis*, **1996**, 159 (1), 127-139.

[93] C. Adlhart and E. Uggerud: "Mechanisms for the Dehydrogenation of Alkanes on Platinum: Insights Gained from the Reactivity of Gaseous Cluster

Cations, Pt-N(+) N=1-21", *Chemistry-a European Journal*, **2007**, 13 (24), 6883-6890.

[94] T. Y. Ju, H. Q. Yang, F. M. Li, X. Y. Li, and C. W. Hu: "Reaction Mechanism on the Activation of Ethane C-H and C-C Bonds by a Diplatinum Cluster", *Theoretical Chemistry Accounts*, **2013**, 132 (9), 14.

[95] E. Yagasaki and R. I. Masel: "Ethylene Adsorption and Decomposition on (1×1) Pt(110): Chemistry of the Coke Formation Site on Platinum?", *Surface Science*, **1989**, 222 (2–3), 430-450.

[96] J. A. Rodriguez and M. Kuhn: "Chemical and Electronic Properties of Pt in Bimetallic Surfaces: Photoemission and Co-Chemisorption Studies for Zn/Pt(111)", *The Journal of Chemical Physics*, **1995**, 102 (10), 4279-4289.

[97] S. J. Tauster, S. C. Fung, R. T. K. Baker, and J. A. Horsley: "Strong Interactions in Supported-Metal Catalysts", *Science*, **1981**, 211 (4487), 1121-1125.

[98] R. M. Mironenko, O. B. Belskaya, V. P. Talsi, T. I. Gulyaeva, M. O. Kazakov, A. I. Nizovskii, A. V. Kalinkin, V. I. Bukhtiyarov, A. V. Lavrenov, and V. A. Likholobov: "Effect of Γ-Al2o3 Hydrothermal Treatment on the Formation and Properties of Platinum Sites in Pt/Γ-Al2o3 Catalysts", *Applied Catalysis A: General*, **2014**, 469 (0), 472-482.

[99] S. W. Gaarenstroom and N. Winograd: "Initial and Final State Effects in the Esca Spectra of Cadmium and Silver Oxides", *The Journal of Chemical Physics*, **1977**, 67 (8), 3500-3506.

[100] J. Silvestre-Albero, A. Sepúlveda-Escribano, F. Rodríguez-Reinoso, and J. A. Anderson: "Influence of Zn on the Characteristics and Catalytic Behavior of Tio2-Supported Pt Catalysts", *Journal of Catalysis*, **2004**, 223 (1), 179-190.

[101] L. Ley, S. P. Kowalczyk, F. R. McFeely, R. A. Pollak, and D. A. Shirley: "X-Ray Photoemission from Zinc: Evidence for Extra-Atomic Relaxation Via Semilocalized Excitons", *Physical Review B*, **1973**, 8 (6), 2392-2402.

[102] R. Prins: "Hydrogen Spillover. Facts and Fiction", *Chemical Reviews*, **2012**, 112 (5), 2714-2738.

[103] V. V. Rozanov and O. V. Krylov: "Hydrogen Spillover in Heterogeneous Catalysis", *Russian Chemical Reviews*, **1997**, 66 (2), 107-119.

[104] U. Roland, R. Salzer, T. Braunschweig, F. Roessner, and H. Winkler: "Investigations on Hydrogen Spillover. Part 1.-Electrical Conductivity Studies on Titanium Dioxide", *Journal of the Chemical Society, Faraday Transactions*, **1995**, 91 (7), 1091-1095.

[105] W. C. Conner and J. L. Falconer: "Spillover in Heterogeneous Catalysis", *Chemical Reviews*, **1995**, 95 (3), 759-788.

[106] P. A. Sermon and G. C. Bond: "Hydrogen Spillover", *Catalysis Reviews: Science and Engineering*, **1974**, 8 (1), 211-239.